
Bridging the Pressure Gap with Scanning Tunneling Microscopy

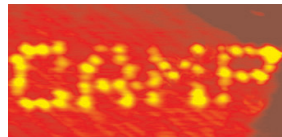
Peter Thostrup

Center for Atomic-scale Materials Physics
Department of Physics and Astronomy
University of Aarhus, Denmark

PhD thesis

July 2002

This thesis is submitted to the Faculty of Science at the University of Aarhus, Denmark, in order to fulfill the requirements for obtaining the PhD degree in Physics. The studies have been carried out under the supervision of Flemming Besenbacher in the scanning tunneling microscopy laboratory at the Department of Physics and Astronomy from August 1998 to July 2002.



Contents

List of Publications	iv
1 Introduction and motivation	1
1.1 Catalysis in and around us	2
1.2 Surface-science approach	3
1.3 Why high-pressure STM?	5
2 Experimental methods	7
2.1 Introduction	8
2.2 Experimental setup	9
2.2.1 Main chamber	9
2.2.2 The Aarhus STM	10
2.2.3 High-pressure cell and STM	12
2.2.4 STM tips	13
2.2.5 Gas handling	14
2.3 Atomic-scale imaging in a reactive atmosphere	16
2.4 Additional UHV techniques	17
2.4.1 Low-energy electron diffraction	17
2.4.2 Temperature-Programmed Desorption	18
3 Theoretical methods	21
3.1 Introduction	22
3.2 Density functional theory	22
3.2.1 STM image formation	25
3.2.2 STM image simulation	27
3.3 <i>d</i> -band model	29
3.4 Monte Carlo simulations	32
4 Hydrogen on Cu(110)	35
4.1 Introduction	36
4.2 <i>In situ</i> STM imaging	36

4.3	Quantitative comparison	40
4.4	Impurity-related structures	42
4.5	Conclusion	45
5	CO adsorption on Pt at low and high pressure	47
5.1	Introduction	48
5.2	CO on Pt(111)	49
5.2.1	Previous UHV and HP studies	49
5.2.2	High-pressure CO/Pt(111)	51
5.2.3	STM observations at low temperature	55
5.2.4	Conclusion	56
5.3	CO on Pt(110)	57
5.3.1	Experimental results	57
5.3.2	Discussion	64
5.3.3	Conclusions	71
5.4	CO on Pt(100)	73
5.4.1	Previous UHV studies	73
5.4.2	Preliminary results	74
6	Vacancy-related phenomena on TiO₂(110)	77
6.1	Introduction	78
6.1.1	Electronic structure of metal oxides	79
6.1.2	Adsorption on metal oxides	80
6.2	Rutile TiO ₂	80
6.2.1	Bulk rutile TiO ₂ structure	81
6.3	Structure of the rutile TiO ₂ (110) surface	82
6.3.1	Sample preparation	84
6.3.2	Appearance in STM	84
6.3.3	Surface defects	84
6.4	Voltage-dependent STM imaging	86
6.5	Water dissociation on TiO ₂	89
6.5.1	Motivation	89
6.5.2	DFT calculations	90
6.5.3	Experimental results and discussion	91
6.5.4	Conclusion	94
6.6	Nucleation and growth of Au on TiO ₂ (110)	96
6.6.1	Motivation	96
6.6.2	Experimental results and discussion	96
6.6.3	Conclusion	102
6.7	Absence of “cannon-ball” effect in Br/TiO ₂ (110)	103
6.7.1	Transient motion of bromine	104
7	Summary and outlook	107
	Bibliography	111
	Acknowledgements	121

List of Publications

- [I] *Bridging the Pressure Gap in Surface Science at the Atomic Scale: H/Cu(110)*, L. Österlund, P. B. Rasmussen, P. Thstrup, E. Lægsgaard, I. Stensgaard, and F. Besenbacher, *Phys. Rev. Lett.* **86**, 460–463 (2001).
- [II] *A high-pressure scanning tunneling microscope*, E. Lægsgaard, L. Österlund, P. Thstrup, P. B. Rasmussen, I. Stensgaard, and F. Besenbacher, *Rev. Sci. Instr.* **72**, 3537–3542 (2001).
- [III] *Adsorption-induced step formation*, P. Thstrup, E. Christoffersen, H. T. Lorensen, K. W. Jacobsen, F. Besenbacher, and J. K. Nørskov, *Phys. Rev. Lett.* **87**, 126102 (2001).
- [IIIa] *Erratum: Adsorption-induced step formation*, P. Thstrup, E. Christoffersen, H. T. Lorensen, K. W. Jacobsen, F. Besenbacher, and J. K. Nørskov, *Phys. Rev. Lett.* **88**, 049902(E) (2002).
- [IV] *Oxygen vacancies as active sites for water dissociation on rutile TiO₂(110)*, R. Schaub, P. Thstrup, N. Lopez, E. Lægsgaard, I. Stensgaard, J. K. Nørskov, and F. Besenbacher, *Phys. Rev. Lett.* **87**, 266104 (2001).
- [V] *CO-induced restructuring of Pt(110)-(1×2): Bridging the pressure gap with high-pressure STM*, P. Thstrup, E. K. Vestergaard, T. An, S. Helveg, E. Lægsgaard, I. Stensgaard, and F. Besenbacher, *J. Chem. Phys.*, submitted.
- [VI] *Comment on “High Pressure Adsorbate Structures Studied by Scanning Tunneling Microscopy: CO on Pt(111) in Equilibrium with the Gas Phase”*, E. Kruse Vestergaard, P. Thstrup, T. An, E. Lægsgaard, I. Stensgaard, B. Hammer, and F. Besenbacher, *Phys. Rev. Lett.* **88**, 259601 (2002).
- [VII] *Bridging the pressure gap between surface science and catalysis using high-pressure scanning tunneling microscopy*, P. Thstrup, E. Kruse Vestergaard, E. Lægsgaard, I. Stensgaard, and F. Besenbacher, *Prog. Surf. Sci.*, “Progress Highlight” in preparation.

- [VIII] *Bias-dependent STM imaging of the pristine and hydroxylated TiO₂(110) surface*, P. Thostrup, R. Schaub, N. Lopez, E. Lægsgaard, I. Stensgaard, J. K. Nørskov, and F. Besenbacher, in preparation.
- [IX] *Bonding of Gold Nano-Clusters to Oxygen Vacancies on Rutile TiO₂(110)*, E. Wahlström, N. Lopez, R. Schaub, P. Thostrup, A. Rønnau, C. Africh, E. Lægsgaard, J. K. Nørskov, and F. Besenbacher, Phys. Rev. Lett., submitted.
- [X] *Absence of cannon-ball effect in the Br/TiO₂(110) system*, K. Swamy, E. Kruse Vestergaard, M. Dall Rasmussen, P. Thostrup, B. Hammer, F. Besenbacher, in preparation.

CHAPTER 1

Introduction and motivation

Here we give a short introduction to some basic concepts of heterogeneous catalysis and their connection to surface science. The application of surface-science data to real catalytic processes leads to the definition of a number of so-called gaps between surface science and catalysis. These gaps are discussed and it is argued how the current thesis fits into a context defined by them.

1.1 Catalysis in and around us

A catalyst accelerates a chemical reaction without being consumed itself in the process, and possibly also selectively favors a specific reaction over competing, undesired reactions. Without catalysts, certain important chemical reactions would hardly take place because of high activation barriers, even though they are expected to proceed readily on thermodynamic grounds, i.e. the product state has lower Gibbs free energy than the reactant state. The solution is the introduction of suitable catalysts which permit the desired products to be produced with appreciable rates. This typically proceeds by breaking up the overall reaction into several additional steps, each with a lower activation barrier than that of the direct reaction, as illustrated by the energy diagram in Fig. 1.1. Almost any commercial chemical undergoes one or more catalytic processes during its production and it is safe to say that catalysis thus affects almost every aspect of our life.

Most basic is our dependence on the catalysis occurring within us; here enzymes are the catalysts which take part in all aspects of biochemistry. Nature has found a perplexingly intricate way to make all essential processes proceed at 37°C and 1 bar. Such high performance is however still far beyond our reach or control and for the artificial catalytic processes exploited in modern chemical industry, we have to resort to cruder methods. Typical process parameters reach temperatures of hundreds of degrees and pressures in the 1–100 bar range. The kind of catalysis performed by enzymes is branded homogeneous catalysis because reactants and catalyst reside in the same, generally liquid, phase. Industrial processes typically employ a heterogeneous scheme, so called because the reactants are present in different phases, with the reactants in a gaseous phase and the catalyst in the solid state. The catalyst surface then becomes the locus for the gaseous species to meet and react.

The economic impact of heterogeneous catalytic processes can hardly be overestimated. In the United States alone, the market value of products depending on catalytic processes is currently in excess of 10^{12} \$ and rising [1]. One of the most important catalytic processes, historically and presently, is the Haber process to produce ammonia:



Invented by Fritz Haber and refined by Carl Bosch and Alwin Mittasch around 1900, the large-scale industrial production of ammonia with an iron catalyst formulation started a gold rush for new ways to produce chemicals aided by catalysts. Mittasch set out to test, by trial and error, thousands of combinations of metals and oxides and catalyst preparation methods. Even today, catalyst preparation is by many considered an art, or even black magic, and high-speed screening, essentially a trial-and-error method as well, is in widespread use.

Also around the beginning of the 20th century, Irving Langmuir¹ started the first detailed investigations into the processes underlying surface chemistry. With an impressive combination of ingenuity and intuition, he grasped many of the surface-science concepts still in use today [2]. It was however not until the advent of Ultra-High Vacuum (UHV)

¹Langmuir received the 1932 Nobel Prize in Chemistry “for his discoveries and investigations in surface chemistry”.

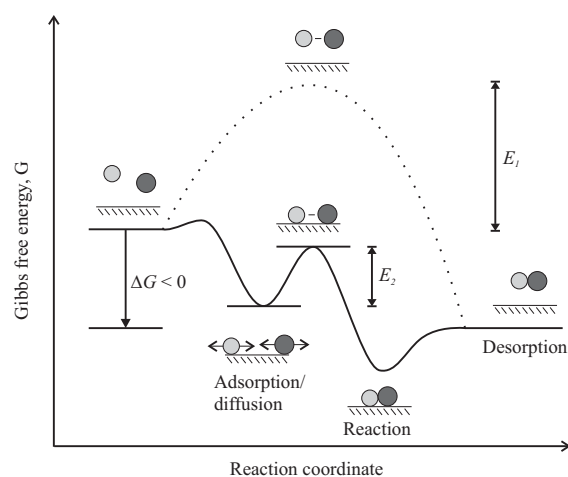


Figure 1.1: Illustration of catalysis action. The overall reaction, here assumed to occur in the gas phase without the intervention of the catalyst surface, is broken up into two steps. Below some steps, the nomenclature associated with each is noted. The two activation barriers, E_1 without catalyst and E_2 with catalyst, are indicated.

techniques in the 1960s that the implementation of surface-sensitive techniques became feasible [3].

Surface science has to a large extent been driven by (heterogeneous) catalysis. The hope is that new catalysts can be designed based on fundamental insight into the atomic-scale mechanisms governing catalytic activity, as has indeed been demonstrated in a few cases [4]. Over the last 35 years, a whole arsenal of surface-sensitive techniques has been devised to study the separate processes occurring on catalyst surfaces. The scientific approach to catalysis has been a reductionistic one; the overall reaction is broken into its separate steps, which are then studied and analyzed individually. Fundamental surface-science studies have introduced the now well-known concepts of surface adsorption, diffusion, reaction, and desorption illustrated in Fig. 1.1. These concepts of surface science, first introduced by Langmuir [2], are today an integral part of the basic ideas and vocabulary used in catalytic contexts.

1.2 Surface-science approach

An industrial catalyst is evidently optimized for maximum performance per catalyst volume, i.e. a high surface area is desired. To achieve this, the active material is dispersed on a porous support with a concurrent rise in complexity. This makes the catalyst very hard to characterize on the atomic scale, particularly under realistic operating conditions, i.e. high pressures and temperatures. The reductionistic approach however requires complete control over all parts of the system under investigation and heavy

approximations—to be discussed below—have to be introduced. The aggregation of these approximations together with reductionistic approach is often referred to as the “surface-science approach to catalysis” [2, 5].

Surface scientists have come a long way in understanding the atomistic mechanisms governing bonding and reactivity of adsorbates on surfaces. In some cases, it has even been demonstrated that the activity of a real catalyst can be modelled based on surface-science data alone [6, 7]. The surface-science approach to catalysis lead to the identification of a number of so-called gaps between surface science conditions and high-pressure/high-temperature conditions employed in heterogenous catalysis, among these [8]:

- the pressure gap
- the materials gap

The pressure gap arises due to the high ($1-10^2$ bar) pressures and temperatures employed in industrial catalytic processes. In contrast, a typical surface-science experiment is performed at low temperature (relative to relevant adsorbate desorption temperatures) and low pressures ($10^{-13}-10^{-5}$ mbar). These conditions are used extensively to mimic high-pressure situations where a high incoming molecular flux facilitates high adsorbate coverages even well above the adsorbate desorption temperatures.

The materials gap describes the disparity between oxide-supported cluster catalysts and the corresponding single-crystal model catalysts traditionally investigated in surface science. Model catalysts have to be introduced due to the prohibitively complex structure of real catalysts, which often impedes atomic-scale characterization. The influence on the surface chemistry from the small size and complicated shape of supported clusters is not easily reproduced in single-crystal studies. When the cluster size reaches the nanometer regime, first of all the larger relative proportion of surface steps and kinks may alter the catalytic activity [9] and quantum size effects may step in, as has been observed in the case of dispersed gold clusters [10, 11]. Moreover, the presence of a support material often has an indirect influence on the catalytic activity [12] and in some cases, the support even participates in the catalytic process. A example of the latter is the reversible oxygen-storing and releasing capacity of reducible cerium oxide used in automotive three-way catalytic converters. Here the support oxide cooperates via spill-over with the catalytically active platinum clusters to oxidize carbon monoxide or unburned hydrocarbons under fuel-rich conditions [13].

Notable progress has recently been made in approaching more realistic model catalysts. In particular, metal catalysts deposited on oxide supports have been used to reproduce effects originating from the metal-oxide interface [14–17]. The studies on Au/TiO₂(110) reported in the penultimate chapter of this thesis also falls within this category.

A more subtle aspect of the materials gap is the fact that the presence of adsorbates may alter the relative stability of different crystal facets to produce varying crystal shapes under different reaction conditions. The metal-oxide interfacial energy may also be influenced by the gaseous environment. One recent example is the dynamic shape changes of nano-crystalline Cu/ZnO observed when switching between oxidizing and reducing

conditions [18, 19]. The change in interfacial energy is suggested to arise from a modification of the oxygen content in the ZnO surface caused by a change in the oxidation potential of the gas.

The initial composition of the catalyst may also change under reaction conditions. This includes adsorption-induced surface segregation [20, 21] and the formation of a new catalytically active phase. The latter effect has been convincingly demonstrated in the case of Ru, which in its metallic state acts as a rather poor catalyst for CO oxidation. Under reaction conditions, it is found that a new phase, RuO₂, grows epitaxially with its (110) plane parallel to the Ru(0001) plane. The catalytic activity of the RuO₂ phase is much higher than that of Ru, and even superior to platinum [22, 23]. More generally, it has been suggested that the existence of an “induction period” during some catalytic processes may be an indication that the initial catalyst material undergoes dramatic changes into a new phase, which is then the real catalytically active material [24].

The two latter examples are obviously intimately connected to the pressure gap. In some cases, the materials gap and pressure gap should even be discussed together. An example of this is the case of CO oxidation on Ru [22, 23], which for many years was believed to be a clear manifestation of the pressure gap. As discussed above, the active phase for CO oxidation at high oxygen pressures is simply a different material, RuO₂, and neither a pressure gap nor a materials gap can be claimed to exist for this system. Gas-induced structural and compositional changes can sometimes be examined with post-mortem analysis, but it is imperative to realize that these changes may well be reversible and only exist under high gas pressures or during reaction. This emphasizes the need for *in situ* investigations to characterize the active phase.

1.3 Why high-pressure STM?

At the high pressures and temperatures employed in real catalysis, new and unexpected phenomena have been reported as compared to what is observed through the conventional surface science approach [25–27]. The application of UHV data on the other side of the pressure gap is necessarily rendered invalid, if the surface science approach fails to explain processes occurring at high pressures and temperatures. From cases in the literature where relations between the two sides of the pressure gap have been investigated so far [6, 25–29], it can only be concluded that the high-pressure response is system specific. There is thus a clear need to add to the number of systems considered and from specific cases try to extract general trends. Work along these directions is still sparse but we hope the studies presented in Chaps. 4 and 5 of this thesis will help correct this situation.

Our approach to establishing correlations between the two sides of the pressure gap is to investigate the response of selected single-crystal surfaces to reactive gases over 13 orders of magnitudes in pressure, up to atmospheric pressure. We do this using the same technique, Scanning Tunneling Microscopy (STM), at all pressures. Two sets of studies on H/Cu(110) (Chap. 4) and CO on two different Pt terminations, (111) and (110), (Chap. 5) address the pressure gap directly by establishing correlations between the two sides of the pressure gap.

STM is not a crystallographic technique so bond lengths and structural details of other than the topmost layer cannot be obtained. This limitation notwithstanding, combined with more traditional techniques, STM has proved an invaluable tool for adding in a complementary way to existing insight into specific systems. The literature contains several examples where a reexamination with STM has helped resolve long-standing disputes and affected a rejection or refinement of existing models [30–33].

Most surface-sensitive techniques exploit combinations of incoming and outgoing electrons, ions, and photons created and detected at a distance from the surface under investigation. Since the advent of UHV techniques and consequent practical applicability of surface-sensitive technique, much has been learned about surface structural and vibrational properties as well as fundamental aspects of surface processes. With the increasing level of understanding has however followed the realization that in many cases, structural imperfections have a profound influence on surface reactivity [12, 34].

A minority species or structural defects such as vacancies, kinks, and steps are not easily detected with most traditional surface-sensitive techniques owing to their averaging nature. The unique characteristic and great virtue of STM is its ability to provide extremely local information and between the probe techniques, STM is still unsurpassed in supplying true atomic-scale resolution. The studies presented in this thesis rely on this ability and in some cases, it is difficult to imagine how the same level of detailed insight could have been obtained otherwise.

A determination of the chemical identity of observed features in STM images frequently requires the assistance of theoretical STM image simulations. An additional complication is the fact that STM images are dominated by electronic rather than geometric effects [35, 36]. We shall see an example of the synergetic interplay between experiment and theory in Chap. 6 where a identification of and distinction between two surface-defect species (oxygen vacancies and hydroxyl groups) will prove essential to unravel the water-dissociation mechanism on $\text{TiO}_2(110)$. Based on this knowledge, we are able to investigate the nucleation and growth of gold on $\text{TiO}_2(110)$. Surface vacancies are found to have a profound influence on the nucleation behavior and a novel growth mechanism involving vacancy-cluster complex diffusion is presented. These studies do not fit directly into the pressure-gap context of previous chapters but should rather be viewed as providing the necessary pieces of information to enable a comparison to future high-pressure studies of the $\text{Au/TiO}_2(110)$ system.

CHAPTER 2

Experimental methods

This chapter describes the experimental setup used to obtain the results in subsequent chapters. This includes the UHV chamber and attached apparatus. The main experimental technique being STM we shall go to some length in describing the detailed design of the home-built UHV and High-Pressure (HP) STMs. We shall see later that high-pressure gas handling imposes additional requirements on gas cleanliness compared to conventional gas handling for UHV systems. Hence we present a description of the specially designed gas handling system. Also included is a demonstration of the performance of the novel HP-STM design, which enables atomic-scale imaging even at atmospheric pressures of both noble and reactive gases.

2.1 Introduction

Modern surface science wields an arsenal of surface-sensitive techniques exploiting the interaction of any conceivable combination of ions, electrons, and photons made to impinge on and/or eject from a surface, each combination designated by a more or less idiomatic acronym [37, 38]. Free ions and electrons scatter strongly in any gas or material so to attain a sufficiently long path length, their path to/from the material under investigation has to be cleared of obstacles. This necessity was part of the motivation behind the development of UHV techniques in the 1960s. Equally important was the need to maintain a clean and well-defined surface for an extended period of time since surfaces in air or limited vacuum become covered with a layer of contaminants within seconds.

The latter requirement may be circumvented by employing ultra-pure gases, but as mentioned before, the use of many traditional surface science techniques is inherently hindered at high pressures. An increasing number of techniques that provide detailed structural information has however recently been developed to overcome this problem. These include environmental transmission electron microscopy (TEM), x-ray diffraction (XRD) and absorption techniques, Sum-Frequency Generation (SFG), atomic-force microscopy, and STM. Photon techniques are not inherently restricted to UHV environments but in the case of e.g. SFG it has been demonstrated that it is nevertheless mandatory to minimize the path lengths of the incoming and outgoing laser beams through the high-pressure volume [39, 40]. STM does not suffer from scattering in the gas phase owing to the extremely short path length of the electrons passing between tip and sample so it can be employed in at any pressure.

With *in situ* transmission electron microscopy (TEM), it is possible to retain layer resolution at pressures in the mbar range by applying high pressures only close to the sample, e.g. on a Cu/ZnO methanol synthesis catalyst [19, 41]. The same system has been investigated using *in situ* Extended X-ray Absorption Fine Structure (EXAFS) at high pressures [18, 42]. These techniques have the additional advantage of facilitating imaging of non-idealized, “real” catalysts. So far, none of these methods have however produced genuine atomically resolved images of a metal surface in a reactive atmosphere at high pressures.

In our approach, HP-STM is in most cases not applied as the first technique when embarking into investigations on a new system. First of all, an understanding of the UHV behavior is required to facilitate comparison across the pressure gap. Second, it should not be overlooked that the introduction of high gas pressures adds significant complications such as influence from impurities and higher noise levels while imaging. Much effort has hence been invested in UHV investigations prior to moving on to HP-STM.

We therefore start this chapter with a description of the UHV chamber and attached apparatus, including the UHV “Aarhus STM”. In continuation, we present a novel HP-STM design, which for is capable of imaging metal surfaces and any other conductive surface with atomic resolution in reactive gases all the way from UHV to atmospheric pressures. We discuss the design of the HP-STM, which is in principle a further development of the Aarhus STM design [43]. To illustrate the extremely good image quality

of the HP-STM, we present details of a study involving imaging under high pressures of hydrogen gas on the Au(111) surface.

To conclude this chapter, we include descriptions of two other UHV techniques, low-energy electron diffraction (LEED) and Temperature Programmed Desorption (TPD), which were used to support the interpretation of the STM results presented in later chapters.

2.2 Experimental setup

In this section we describe in detail the design and implementation of a HP-STM in a multi-purpose UHV system. We will describe (i) the main UHV chamber, (ii) the Aarhus STM, (iii) the HP cell attached to the main chamber and containing the HP-STM, (iv) the choice of material for STM tips, and finally (v) the gas handling system, which allows for dosing of ultra-pure gases into the HP cell.

2.2.1 Main chamber

The main UHV chamber is cylindrically shaped and equipped with a multitude of analytical instruments for surface preparation, chemical and structural analysis [44]. The whole UHV system rests on an *undamped* steel frame, since active vibrational damping is redundant due to the high eigenmode frequency spectrum of the STM (>8 kHz). For chemical analysis, a double-pass cylindrical mirror analyzer is available for Auger electron spectroscopy (AES) and X-ray photoelectron spectroscopy (XPS). A differentially pumped quadrupole mass spectrometer equipped with a gold-plated random flux shield is used for gas analysis and TPD experiments. For structural analysis, the chamber is equipped with reverse view optics for LEED. A digital camera connected to a PC for digital storage and processing is used to record LEED intensities. As a unique feature, the UHV chamber also houses two home-built UHV STMs, one operating at room temperature only and one at variable temperatures.

Sample preparation is facilitated by a fully automated system for cleaning crystals by inert gas sputtering and annealing. It consists of a differentially pumped sputter gun, a piezoelectric gas valve, and a negatively biased Osram filament placed behind the sample for heating by radiation and electron bombardment. Cycles of sputtering and annealing are controlled by a home-built electronics and software package with built-in feedback and security algorithms. With this arrangement, crystals can be cleaned routinely overnight or over weekends without other supervision than that provided by an online log file written to a dedicated web site.

A sophisticated sample holder and sample transfer system allow for quick sample exchange between the HP cell and the UHV chamber. The sample, normally cut in a hat-shaped fashion, is mounted in a Ta¹ support squeezed in place by a thin foil, which is spot-welded to the support plate on the rear. For temperature reading, a thermocouple wire is pressed between the foil and the back of the crystal, which is in turn connected

¹or any other suitable material such as Mo, which is used in the H₂ studies presented in Chap. 4 due to H absorption in Ta

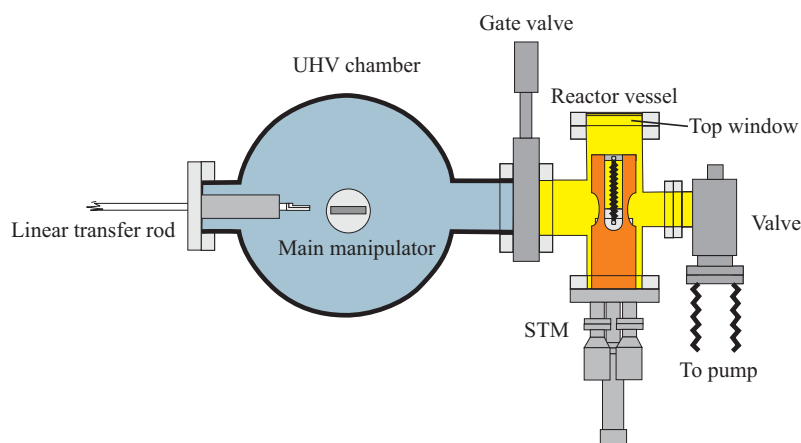


Figure 2.1: Reaction vessel containing the STM, the connection to the UHV system, and the sample transfer mechanism. The manipulator of the main chamber moves perpendicularly to the plane of the figure.

to a thermocouple male connector screwed onto the support plate. This construction constitutes a “mobile” sample unit with retained temperature readout.

For sample transfer between the main chamber and the HP cell, a home-built bellows-sealed linear-motion feedthrough is installed on the chamber wall opposite to the HP cell (see Fig. 2.1). The linear-motion feedthrough is equipped with a pliers grip and can grab the sample plate and move it into position in the HP cell. A cassette of up to nine samples mounted on a linear feedthrough in the main chamber provides easy *in situ* sample exchange without breaking the vacuum. If necessary, *ex situ* sample exchange is readily done via the HP cell, which can also be used as a load lock.

2.2.2 The Aarhus STM

The electronic and mechanical parts of the STMs are all home-built. The key design features of the Aarhus STM are that it is small and compact, has an easy coarse approach of the tip to the sample, is fully automated, and controlled by electronic means only. For the following description, refer to Fig. 2.2: The central part consists of two piezoelectric tubes (Staveley EBL2), a scanner tube for x - y - z movement of the tip relative to the sample, and a linear motor tube used for coarse positioning of the tip relative to the specimen.

The outer surface of the scanner tube is partitioned into four identical sections. When voltages of different polarity are applied to a pair of opposite electrodes, one side contracts and the other expands, whereby the tip can be raster scanned in the x - y surface plane. By changing the voltage of the inner nonsectioned electrode with respect to the outer ones, axial z motion of the tip is achieved. The scanner tube is mounted on a shaft held by the other piezo-tube which, together with the shaft, forms a linear motor.

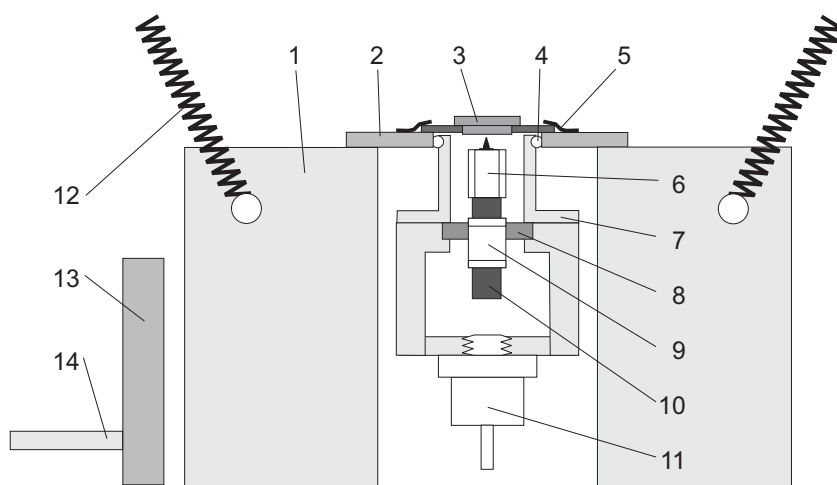


Figure 2.2: Cross-sectional side view of the Aarhus STM. (1) Al cradle; (2) top plate; (3) sample mounted in sample holder; (4) quartz balls; (5) leaf springs; (6) scanner piezo tube and W tip for x - y - z motion; (7) inner STM housing; (8) insulating Macor ring; (9) inchworm piezo tube; (10) SiC shaft; (11) 75 V Zener diode; (12) suspension springs; (13) cold finger; (14) LN₂ feedthrough.

The linear motor is made by dividing the outer electrode on the piezo-tube into three axial sections: two small end sections and a longer center section. The end sections are equipped with bearings inside with a near-perfect fit to the shaft. The linear motor similarly to an inchworm with the smallest step size being in the Å range. It walks by clamping the lower end, expanding the center section, clamping the upper end, unclamping the low end, contracting the center section, and so forth.

The whole assembly is then finally mounted rigidly inside an Invar housing via an attached Macor ring clamped between the housing and a support ring. Above the scanner assembly, the inner housing is mounted on the top plate, thermally and electrically insulated by three balls made of fused quartz. The sample support is mounted in a slit in the top plate, and held in place by two leaf springs. This ensures a good mechanical coupling between the sample and the microscope.

Cooling is achieved by pressing a LN₂-cooled finger against the Al cradle and sample temperatures as low as 100 K can be reached. During imaging, the cold finger has to be retracted but the sample temperature rises only 5–10 K/h due to the large thermal mass of the Al block. The scanner-tube and inchworm assembly is kept at RT at all times by way of a 75 V Zener diode² mounted at the bottom of the inner housing since the SiC shaft would lose its tight fit to the inchworm piezo tube at other temperatures.

²Zener diodes are ideal for local heating in a UHV system since only very low currents (in our case in the mA range) need be used to deposit a sizeable power. Of more practical concern is the fact that threaded Zener diodes are easily made to attach tightly to a metal object.

Furthermore, the piezo coefficients of the scanner-head piezos are strongly temperature dependent and by keeping the whole piezo assembly at RT, we gain the advantage of having to use only one set of image calibration factors.

Sample heating during imaging derives from 75 V Zener diodes similar to the one counterheating the inner house. A stable temperature can be maintained indefinitely since electric heating does not produce vibrations. The scanner-tube assembly however cannot be actively cooled so the upper temperature limit is imposed by the requirement that the scanner-tube assembly not reach temperatures above ~ 310 K since it then would cease functioning. Sample temperatures up to 420 K have been successfully employed.

The compact and rigid design implies that the lateral and vertical resonance frequencies of the STM are as high as 8 and 90 kHz, respectively. This reduces the sensitivity of the STM to external vibrations and allows for fast scanning, i.e. several constant current images can be recorded per second. Added to this is the fact that our STMs have great mechanical stability and vibrational resistance (the noise level is typically below 1 pm root-mean-square). This is why no vibration isolation of the main chamber is used; the only vibration isolation necessary is the springs, from which the STM is suspended, with a low resonance frequency of 3–4 Hz. This effectively dampens transmission of high-frequency vibrations coming from the outside.

2.2.3 High-pressure cell and STM

The HP-STM is integrated into a HP cell and separated from the main chamber by a 6" all-metal gate valve. A vertical section through the UHV chamber at the position of the HP cell is shown in Fig. 2.1. The basic design of the HP cell is a stainless steel cross. The HP cell is pumped by a separate 70 ℓ/s , two-stage turbomolecular drag pump with ceramic bearings. The turbo pump is backed by a membrane pump, thus ensuring a completely oil-free environment. This arrangement facilitates rapid pump-down from atmospheric to vacuum pressure. The pumping line is separated from the HP cell by a manual all-metal gate valve as shown in Fig. 2.1. Gas is admitted through a bellows-sealed Nupro valve or a leak valve (not shown). The pressure is measured from 1 bar to 10^{-8} mbar by a combined cold cathode and Pirani gauge, and a four decade (0.1–1000 mbar) capacitance manometer. The latter gauge has to be added due to the poor precision of the Pirani gauge at high pressures. The gauges are separated from the HP cell by bellows-sealed Nupro valves. To ensure chemical inertness, the cell and all metal parts of the STM are electrochemically gold plated. All connections to the HP cell are made through metal gasket-sealed flanges or VCR connections. A window is mounted on the top flange for visual access of the sample holder and the HP-STM to facilitate sample loading and detachment.

The design of the central part of the HP-STM (shown in Fig. 2.3a) is similar to the Aarhus STM described above [43, 45], with all mechanical parts home-built.

The novel support and suspension of the HP-STM is shown in Fig. 2.3b. The STM housing is rigidly mounted inside a heavy (0.7 kg) steel block suspended inside a metal tube by two springs. The block can be held in a fixed position for sample loading by a holder mounted on a linear translator squeezing the mounting block up against a collar inside the tube (not shown). The free volume of the HP cell is only about 0.5 l . Elec-

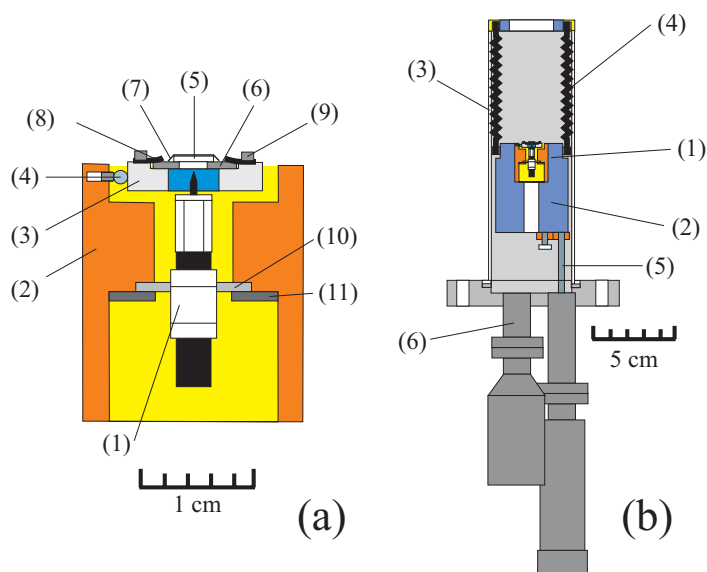


Figure 2.3: (a) HP-STM consisting of: (1) Inchworm-scanner-tip assembly; (2) Invar housing; (3) sample holder; (4) quartz balls; (5) sample; (6) Ta support; (7) Ta foil; (8) leaf springs; (9) screws; (10) Macor ring; and (11) support ring. (b) Mounting and suspension of the STM: (1) STM assembly; (2) mounting block; (3) outer steel tube; (4) suspension springs; (5) linear translator; and (6) electrical feedthroughs.

trical connections to the piezo tube, inchworm, tip, bias voltage, and thermocouple are taken out through two ten-pin electrical feedthroughs. The instrument is mounted on a standard $4\frac{1}{2}$ " Conflat flange.

STM experiments could in principle be performed at pressures higher than atmospheric pressures, but for safety reasons this design is limited to approximately 1 bar because of the top window, which is not designed to withstand pressure from the inside.

2.2.4 STM tips

HP-STM imaging poses demands on the tip material, and care must be taken to ensure successful application. Traditionally, and for good reasons, tungsten is the material of choice for UHV-STM probe tips since they provide the most stable imaging. Also for experiments with hydrogen at atmospheric pressures, we use single-crystal tungsten tips, since W is relatively inert towards H_2 . The performance of the tip in terms of stability and reproducibility suggests that, even at high pressures, H_2 does not react appreciably with the tungsten tip under typical scanning conditions ($V=10\text{--}300$ mV, $I=0.5\text{--}1.5$ nA). Similarly, atomic-scale imaging at high pressures of CO, CO_2 , as well as mixtures of CO_2 and H_2 , was also facilitated by a tungsten tip. This is in contrast to high-pressure imaging in O_2 where W oxidation causes the condition of the tip to

change violently during scanning. So far, our choice of tip material has been limited to W so we have not yet succeeded in imaging in an oxygen atmosphere. Probe tips of platinum or platinum alloys (Pt/Rh, Pt/Ir) have been demonstrated to provide stable imaging in high oxygen pressures [46,47] and such tips are in preparation. Pt tips are not stable in CO so for CO/O₂ mixtures one seems to be restricted to gold tips, which however are more susceptible to blunting than W tips.

2.2.5 Gas handling

The HP studies in this thesis involve H₂/Cu (Chap. 4) and CO/Pt (Chap. 5). These gas/substrate combinations represent two different aspects of the importance of proper gas handling in HP experiments. We shall use the two cases to illustrate these aspects.

First, the H₂ sticking coefficient in the H/Cu system is extremely low ($<10^{-10}$ at room temperature) and at the very large total exposures employed, the surface is exposed to a non-negligible amount of impurity gases, even if their concentration is in the ppb range. Hence the surface chemistry will be dominated by the gas with the highest product of sticking coefficient and partial pressure.

Second, CO forms stable binary carbonyls with many transition metals, primarily from the central part of the transition-metal series. The most stable binary carbonyl is nickel carbonyl, Ni(CO)₄, which is an extremely toxic, colorless liquid (melting point -19.3°, boiling point 42.2°). Since nickel is alloyed into the steel used for gas handling tubes, Ni(CO)₄ is formed inside the gas-handling system and carried along with the gas. When the carbonyl enters the HP cell, it may dissociate and nickel is deposited. This is of course highly undesirable so special precautions have to be taken.

Figure 2.4 shows the layout of the H₂ handling system used with the HP-STM. Gases are admitted to the HP cell through noncorrosive, all-metal valve pressure regulators, followed by an all-metal gas handling system made of stainless steel. The gases used in the experiments presented below and in Chap. 4 were hydrogen and argon of 99.9999% and 99.999% purity, respectively, delivered in lecture bottles. Depending on the required gas purity, different procedures can be used for gas dosing in the HP cell.

All gas dosing typically follows this procedure: first, the gas handling system and the pressure regulators are evacuated; the pressure regulators are heated to roughly 350 K for 10 min. The pressure regulators are then flushed several times with gas and isolated from the gas handling system. They are now left with a slight overpressure (approximately 1.5 bar) on the low-pressure side and cylinder pressure on the high-pressure side. Finally, the all-metal parts of the gas handling system are baked at 400 K for typically 10 h.

If additional purification of the gas is necessary, the gas flow can be redirected (see Fig. 2.4) through additional cleaning stages including catalytic cleaning, molecular sieves, and cold traps. For the H/Cu(110) experiments described in Chap. 4, it turned out that the cleanliness of the supplied hydrogen gas was insufficient (oxygen contaminated) if the gas was used as-delivered, see Sec. 4.4. To clean the gas further, the H₂ gas was passed through a Cu/ZnO/Al₂O₃ catalyst bed (LK-821-2, Haldor Topsøe) to remove residual O, and a 4 Å pore size molecular sieve (UOP Type 4A, Fluka), which

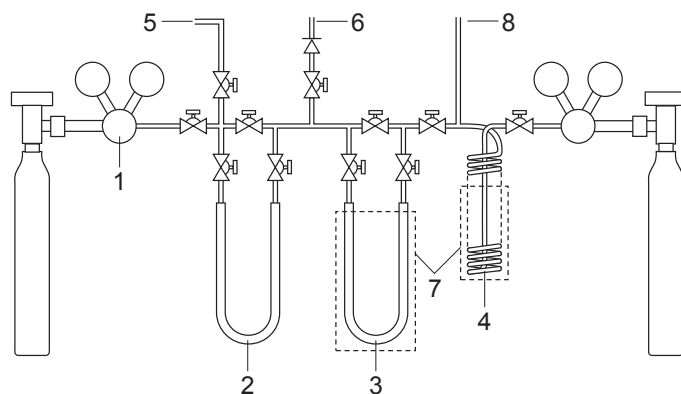


Figure 2.4: System used for purifying as-delivered gases consisting of: (1) All-metal reduction valve; (2) catalyst; (3) molecular sieve; (4) LN₂ cold trap; (5) inlet; (6) exhaust for catalyst preparing gases; (7) cold baths for molecular sieve and spiral tubing; and (8) tube leading to gas-inlet system.

removes oxygen impurities very efficiently. Condensable impurities can furthermore be removed by a liquid nitrogen trap, either by cooling the molecular sieve tube or a dedicated cooling trap.

After the catalytic cleaning stage, the gas is passed to the dosing stage of the gas handling system, which consists of a series of bellows-sealed Nupro stainless-steel valves. The gas can be admitted to the HP cell in two different ways: (i) It can be admitted directly to the HP cell through a check valve, which allows any desired pressure to be reached in the HP cell without back-flowing of the gas; or (ii) the gas can be dosed through a leak valve to achieve precise dosing. This construction allows exposure to the sample to any pressures between UHV and atmosphere. The system described above is suitable for cases where additional gas cleaning can be achieved by catalytic means, simply by inserting a different catalyst for different gases. As mentioned above, CO however presents special problems. A CO cleaning system designed to avoid Ni(CO)₄ formation was added. This system works independently of the rest of the gas-handling system to avoid cross-contamination. First, exposure of CO to stainless steel components is minimized by using copper tubing. Second, just prior to the inlet to the gold-plated HP cell, the CO is passed through an activated carbon filter heated to ~ 400 K. Any Ni-carbonyls will dissociate on the high surface-area powder and the Ni is left behind. This cleaning system has proven effective in that no Ni has been detected by AES on the Pt surfaces under investigation, even after extended CO exposure. The gas inlet procedure is otherwise quite similar to H₂ procedure described above. The only difference is that the brass pressure regulator used for CO cannot be baked owing to internal plastic parts.

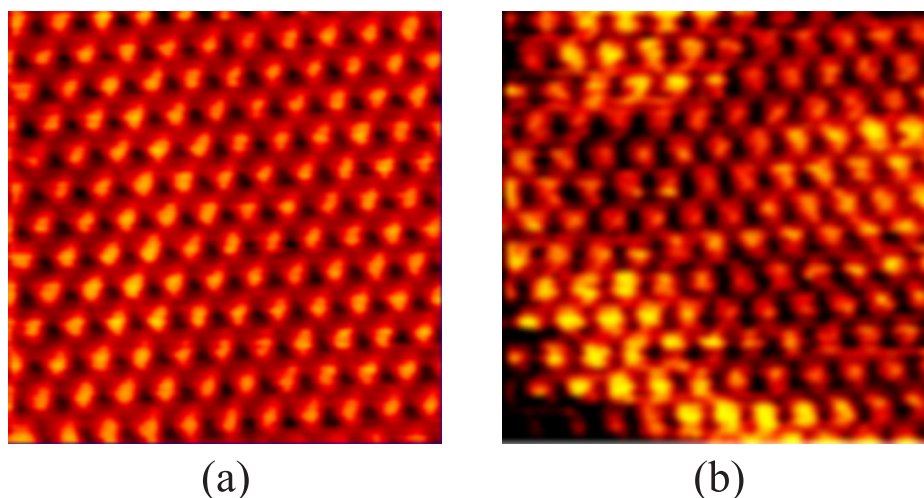


Figure 2.5: STM images of the Au(111) surface at 300 K. (a) $32 \times 31 \text{ \AA}^2$ image displaying atomic resolution in UHV. $V_t=2.0 \text{ mV}$, $I_t=3.37 \text{ nA}$. (b) $32 \times 31 \text{ \AA}^2$ image obtained during exposure to 0.85 bar of H_2 . The atomic structure of the Au(111) surface is clearly seen. $V_t=1.0 \text{ mV}$, $I_t=2.65 \text{ nA}$.

2.3 Atomic-scale imaging in a reactive atmosphere

To test the basic performance of the HP-STM, an Au(111) crystal was chosen as a chemically inert test sample. The sample was cleaned by sputtering and annealing, and then transferred to the STM in the HP cell. With the HP cell open to the UHV chamber, atomically resolved images of the Au(111) surface could readily be obtained, see Fig. 2.5a. High-quality images were observed routinely in a broad range of tunneling parameters. The observed nearest-neighbor distance of 2.94 \AA is in good agreement with the value of 2.88 \AA expected from the bulk lattice constant of 4.08 \AA . Furthermore, at larger length scales, the well-known herringbone reconstruction [48] was routinely observed.

Once a series of reference images was obtained in vacuum, the HP cell was isolated from the UHV chamber by closing the gate valve. First, Ar gas was introduced into the HP cell to 1 atm in order to test the performance of the HP-STM at high pressures in an inert gas. Atomically resolved images were readily obtained, and it was confirmed that at high pressures no acoustic vibrations, that affect the scanning performance significantly, are transmitted through the gas. A satisfactory basic performance of the HP-STM has thus been demonstrated.

As a next step, the Au(111) crystal was exposed to H_2 gas at about atmospheric pressure ($p \sim 0.85 \text{ bar}$). Again, atom-resolved images were readily obtained; a typical image is shown in Fig. 2.5b. Furthermore, the herringbone structure was also observed under these conditions. The images obtained during H_2 exposure were essentially identical to the images obtained under UHV conditions. Comparable corrugation amplitudes and

identical lattice constants were observed for the same tunneling conditions. These results imply that the Au(111) surface is unaffected by the large H₂ flux impinging on the surface at atmospheric conditions, and also demonstrate that the gas purity is satisfactory since the herringbone structure is sensitive to small perturbations [49]. Subsequent pump-down and transfer to the UHV chamber and AES analysis confirmed that the surface was clean within the detection limit (<1%).

The experiment described above clearly demonstrates that STM imaging with atomic resolution in a reactive gas is indeed possible with the HP-STM. The fact that the same corrugation amplitudes are observed in both UHV and in the high-pressure environment for similar tunneling conditions suggests that neither the geometric nor the electronic properties of the tip were affected significantly by the presence of H₂. The slightly higher noise level observed in the images obtained under high-pressure conditions may be caused by molecules entering the vacuum gap during scanning or may be due to coupling of acoustic noise through the gas.

2.4 Additional UHV techniques

For the sake of completion, we give in the following an introduction to two other UHV techniques used for the experiments described in this thesis.

2.4.1 Low-energy electron diffraction

LEED is perhaps the historically most significant example of a surface-sensitive technique³, which can be used to determine first of all the symmetry of an ordered surface structure, but also with some additional effort the exact arrangement of adsorbates and substrate atoms in the surface unit cell. For low-energy electrons, the de Broglie wavelength $\lambda = h/p$ ⁴ and mean free path length, ℓ , in solids conspire to yield electron matter-wave diffraction from the first few atomic layers of an ordered crystal. Coincidentally, both λ and ℓ for 1–1000 eV electrons are at the order of an atomic lattice spacing in solids, resulting in the formation of diffraction patterns and surface sensitivity, respectively.

Neglecting multiple-scattering events, in the so-called kinematic approximation, the LEED pattern represents the surface unit cell in reciprocal space. This of course only occurs for ordered structures but even if only part of the area under investigation is ordered, a diffraction pattern can still be obtained because disordered areas contribute to a uniform background signal upon which the contribution from ordered patches is superimposed. Kinematic LEED images only facilitate a determination of the surface unit cell so details of the exact arrangement of adsorbates and possible symmetry elements within the unit cell remains hidden⁵.

³Clinton Joseph Davisson and George Paget Thomson received the 1937 Nobel Prize in Physics for “their experimental discovery of the diffraction of electrons by crystals”.

⁴ h is Planck’s constant and p the particle’s momentum.

⁵One exception occurs when a glide-plane symmetry element exists in the unit cell. This symmetry element has the effect of extinguishing fractional-order diffraction spots along the glide-plane direction.

More detailed structure determination can however be obtained with a *dynamic* LEED analysis. The same strong scattering, which brings about surface sensitivity, also enhances the probability for an already scattered electron to scatter several additional times and this has to be taken into account when simulating a diffraction-spot intensity vs. incoming electron energy, $I(V)$, spectrum. An $I(V)$ spectrum facilitates an extremely detailed analysis of bond lengths and substrate relaxations once an initial, qualified guess has been input into an optimization routine.

LEED is an inherently area-averaging technique since constructive diffraction only occurs from ordered areas. This impedes observation of isolated defect structures and limits the usefulness of LEED in obtaining genuine atomic-scale information from aperiodic structures. It should however not be overlooked that dynamic LEED still offers the highest attainable precision in bond-length and substrate-relaxation determination for ordered structures.

For the present thesis, we have used kinematic LEED as a standard tool to determine first of all the sample order during the initial stages of sample cleaning. Second, in Chap. 4 LEED images are used as supporting material in determining the structures formed upon H_2 exposure on Cu(110).

2.4.2 Temperature-Programmed Desorption

Desorption techniques are in general employed to learn more about adsorbate-substrate bonding. For thermal desorption, clearly the stronger the adsorbate-substrate bond, the higher temperatures are needed to desorb the adsorbate detect it e.g. by mass spectrometry (MS). Desorption through thermal means is dubbed Thermal Desorption Spectroscopy (TDS) or Temperature-Programmed Desorption (TPD). These often give useful information on the temperature range suitable for avoiding desorption of the adsorbate under investigation or, conversely, making sure an unwanted adsorbate does not stay adsorbed. This kind of considerations is often implicit but for our purpose we have in Secs. 4.2 and 5.3.2 also exploited the incidental side-effect that integrated TPD intensities provide information about the absolute surface coverage of a given adsorbate once scaled against the integrated intensity from a known structure with a well-defined coverage.

More detailed information on the nature and number of adsorbed species as well as their desorption kinetics can be extracted from a quantitative TPD spectrum analysis. In the situation where the desorption energy E_d and frequency factor ν_x are independent of coverage, the rate of change in coverage can be represented by an Arrhenius equation

$$-\frac{d\theta}{dt} = \theta^x \nu_x \exp(-E_d/RT) \quad (2.1)$$

where x is the desorption order. For a molecular adsorbate, such as CO, the rate of desorption will depend linearly on the CO coverage, i.e. we expect first-order desorption ($x=1$). For associative desorption of e.g. O, we expect second-order desorption ($x=2$) since two oxygen atoms have to meet prior to desorption.

During a TPD experiment, the conditions are such that the pumping rate is much larger than the desorption rate, and an analysis can be carried out by noting that the MS

intensity rise of a given molecular species is simply proportional to the desorption rate. A TPD peak at some temperature T_{\max} hence indicates a maximum desorption rate at that temperature. For first-order desorption, T_{\max} is not influenced by coverage while for second-order desorption, T_{\max} will shift with coverage, often providing a useful hint on the desorption mechanism. As will become relevant in later chapters, it is important to realize that second-order TPD peaks often originate from other mechanisms than simple associative desorption, such as adsorbate-adsorbate interactions, substrate transformations, etc.

For TPD analysis, a very useful relationship due to Redhead helps connect the desorption energy and peak temperature T_{\max} :

$$E_d/RT_{\max} = \ln(\nu_1 T_{\max}/\beta) \times 3.64 \quad (2.2)$$

with the heating rate $\beta = dT/dt$. The logarithmic nature of the relationship helps reduce the impact of the different underlying assumptions and may thus provide a useful estimate of the desorption energy.

CHAPTER 3

Theoretical methods

The pieces of new understanding presented in this thesis are not the results of a purely experimental effort but are the synthesis of a synergistic interplay between experiment and theory. The main theoretical technique employed by our collaborators is Density Functional Theory (DFT). A short account of the elements, capabilities and, equally important, limitations of DFT will be given. We shall make use of DFT calculations in Chaps. 5 and 6. An extremely useful conceptual framework that captures general trends from *ab initio* DFT calculations is the so-called *d*-band model. Concepts from this model will be discussed here and exploited extensively in Chap. 5. We close this chapter with a short introduction to the powerful Monte Carlo technique.

3.1 Introduction

The expanding database of experimental surface-science data carries with it the need for conceptual frameworks, which can be used to interpret or rationalize the results in general terms. With the development of accurate numerical techniques and concurrent rapid increase in computing power, it has become possible to treat more and more complex systems and effectively perform computer simulations of real systems. The level of sophistication is now such that equilibrium structures, adsorption energies, reaction pathways, and reaction mechanisms can be routinely calculated. The accuracy is however still not high enough to calculate chemical reaction rates but accurate enough to facilitate a semiquantitative description of adsorption and reaction processes.

This chapter describes the theoretical methods used for assisting the interpretation of some of the experimental results presented in this thesis. These include Density Functional Theory (DFT), which is the state-of-the-art method for obtaining accurate equilibrium structures and adsorption energies.

Large-scale DFT calculations are necessary for obtaining an accurate description of adsorption and reaction processes. As is also the case for experimental results, it would however be extremely helpful to create a model, which captures general trends from (computer) experiments. One such model is the *d*-band model, which explains the adsorption behavior of atoms and molecules on metal surfaces. The *d*-band model will prove invaluable for the interpretation of the complex behavior observed in the CO/Pt(110) system in Chap. 5 and is described in detail in Sec. 3.3.

The Monte Carlo technique is discussed in the last section and exploited in Chap. 5 to elucidate the mechanisms underlying a series of complex substrate transformations observed in the CO/Pt(110) system. Importantly, the interaction parameters entering the MC simulations presented in Chap. 5 are all taken from *ab initio* DFT calculations.

3.2 Density functional theory

DFT describes how the ground state electron density and total energy can be obtained by solving a set of one-electron Schrödinger equations (the Kohn-Sham equations) instead of an intractable N -electron Schrödinger equation. This results in an enormous simplification and systems containing more than 1000 electrons can be treated with high accuracy.

The efficacy of DFT finds its root in a theorem due to Hohenberg and Kohn [50]. It states that the full many-particle ground state Ψ of an interacting inhomogeneous electron gas in a static potential $v(\mathbf{r})$ is a unique functional of the electron density $n(\mathbf{r})$ ¹. From this theorem and the Rayleigh-Ritz variational principle, Hohenberg and Kohn showed that ground-state energy $E[n(\mathbf{r})]$ is a minimum for the correct density function $n(\mathbf{r})$, with $n(\mathbf{r})$ as the variational function.

¹Walter Kohn was awarded the 1998 Nobel Prize in Chemistry for the development of DFT [51].

The ground-state energy can be written as

$$E = \int v(\mathbf{r})n(\mathbf{r})d\mathbf{r} + \frac{1}{2} \int \int \frac{n(\mathbf{r})n(\mathbf{r}')}{|\mathbf{r} - \mathbf{r}'|} d\mathbf{r}d\mathbf{r}' + G[n] \quad (3.1)$$

where the first term represents the interaction between the electrons and the static potential $v(\mathbf{r})$ set up by the nuclei, the second term the electrostatic electron-electron interaction (with a factor 1/2 to correct for double counting), and $G[n]$ is a universal functional of the electron density whatever the potential $v(\mathbf{r})$. In a definition due to Kohn and Sham [52], $G[n]$ is furthermore split up into two terms

$$G[n] \equiv T_s[n] + E_{xc}[n] \quad (3.2)$$

where $T_s[n]$ is the kinetic energy of a system of *noninteracting* electrons and $E_{xc}[n]$ the exchange and correlation energy of an interacting system. Until now, no approximations have been made but unfortunately we do not know how to write the dependence of the exchange and correlation energy on the electron density in an explicit way. For slowly varying densities, however, one can approximate $E_{xc}[n]$ by the Local Density Approximation (LDA)

$$E_{xc}[n] = \int n(\mathbf{r})\epsilon_{xc}(n) d\mathbf{r} \quad (3.3)$$

where $\epsilon_{xc}(n)$ is the exchange and correlation energy per electron in a *uniform* electron gas of density n , which can be calculated exactly [50], hence the term LDA. The stationary nature of E in Eq. 3.1 leads, via the Rayleigh-Ritz variational principle, to surprisingly simple one-electron Schrödinger equations, the so-called Kohn-Sham equations, from which $n(\mathbf{r})$ and the Kohn-Sham eigenvalues ϵ_i can be obtained:

$$\left\{ -\frac{1}{2}\nabla^2 + \phi(\mathbf{r}) + \mu_{xc}(n(\mathbf{r})) \right\} \psi(\mathbf{r}) = \epsilon_i \psi_i(\mathbf{r}) \quad (3.4)$$

under the constraint

$$n(\mathbf{r}) = \sum_{i=1}^N |\psi_i(\mathbf{r})|^2. \quad (3.5)$$

Here

$$\phi(\mathbf{r}) = v(\mathbf{r}) + \int \frac{n(\mathbf{r}')}{|\mathbf{r} - \mathbf{r}'|} d\mathbf{r}' \quad (3.6)$$

is the electrostatic potential and

$$\mu_{xc}(n) = \frac{d(n\epsilon_{xc}(n))}{dn} \quad (3.7)$$

is the exchange and correlation contribution to the chemical potential of a uniform gas of density n . In this way, an N -particle problem has been reduced to equivalent Schrödinger equations describing single electrons moving in an effective potential

$\phi(\mathbf{r}) + \mu_{xc}(n(\mathbf{r}))$ set up by the surrounding ions and electrons. Equations (3.4)–(3.7) must be solved self-consistently starting with an assumed $n(\mathbf{r})$, then finding $\phi(\mathbf{r})$ from (3.6) and μ_{xc} from (3.7) and solving (3.4) and (3.5) to get a new $n(\mathbf{r})$. The ground-state energy is given by

$$E = \sum_{i=1}^N \epsilon_i - \frac{1}{2} \int \int \frac{n(\mathbf{r})n(\mathbf{r}')}{|\mathbf{r} - \mathbf{r}'|} d\mathbf{r}d\mathbf{r}' + \int n(\mathbf{r}) [\epsilon_{xc}(n(\mathbf{r})) - \mu_{xc}(n(\mathbf{r}))] d\mathbf{r} \quad (3.8)$$

A sum of one-electron energies does enter into this expression but the presence of the next two terms invalidates an interpretation of the Kohn-Sham energy eigenvalues ϵ_i as single-particle energies.

The calculated ground-state energy E is obviously dependent on the specific choice of exchange and correlation energy functional $E_{xc}[n]$. While very good at predicting structural properties, LDA significantly overestimates adsorption energies, typically of the order of several eV. In recent years, improvements to LDA have been invented, collectively known as the Generalized Gradient Approximation (GGA), where also the gradient of the electron density enters:

$$E_{xc}[n] = \int n(\mathbf{r})f(n, \nabla n) d\mathbf{r} \quad (3.9)$$

The choice of the function f , and hence the total energy functional, is still a matter of debate and different versions have appeared, one of the first one being the Perdew-Wang 91 (PW91) functional [53]. Later developments include the Perdew-Burke-Ernzerhof (PBE) functional [54] and revised version of the latter, such as revPBE [55] and RPBE [56]. revPBE and RPBE are designed to yield more accurate adsorption energies than PW91 and PBE, and are indeed generally found to do so [56].

The self-consistent solution of the Kohn-Sham equation requires a specification of the wave functions Ψ_i of all electrons of every atomic species. While significantly simplified compared to the original N -particle problem of interacting electrons, DFT calculations involving every participating electron are still computationally impractical. Additional significant simplifications are typically employed. First, core electrons can with impunity be fixed in their atomic orbitals (frozen core approximation). Second, in the pseudopotential approximation the core electrons are even projected out of the problem by describing the outer electrons by pseudowave functions. As a mitigating feature, these pseudowave functions wiggle less violently than do normal atomic wave functions since the strong oscillations close to the nucleus imposed by orthogonalization to core states are left out. This in turn facilitates an expansion in slowly varying plane waves with energies up to an energy cutoff chosen so that proper convergence is achieved.

For surface calculations in particular, a third trick is played to adequately describe a truncated crystal. This is accomplished by making use of so-called supercells, which, when repeated in all spatial dimensions, mimic a semi-infinite crystal. For plane-wave expansions, the supercells are made up of the surface unit cell and a finite number of atomic layers perpendicular to the surface. The resulting slabs are separated by vacuum regions and net slab charges or dipole moments are corrected for in this vacuum region to minimize interactions between slabs. In DFT calculations involving supercells, any

adsorbate or structural defect is replicated parallel to the surface and adsorbate interactions may influence the resulting structure and energy. While this is highly desirable for ordered adsorbate overlayers, for isolated adsorbates or defects one has to enlarge the surface supercell sufficiently in order to avoid these, now artificial, interactions.

Errors originating from the choice of supercell, convergence of relaxations, and energy cutoff can be checked systematically, but errors due to the choice of a particular exchange-correlation energy functional are not easily estimated. Different versions and revisions give slightly different absolute energies (typically within 0.25 eV) and one could pragmatically assume the standpoint that the difference between their outputs is perhaps best viewed as a measure of the inherent uncertainty of DFT calculations. Absolute adsorption or defect-formation energies should thus not be expected to be calculated better than 0.25 eV. When comparing e.g. adsorption energies for similar systems, however, systematic errors tend to cancel and higher accuracy can in general be achieved.

3.2.1 STM image formation

Scanning Tunneling Microscopy (STM) is a local probe technique used for investigating both static and dynamic surface structures [57]. Its principle is simple: A sharp metallic tip is brought into atomic proximity ($z \approx 3\text{-}5 \text{ \AA}$) of a sample surface. The tip and surface wave function decay exponentially into the vacuum gap separating the two and due to vacuum tunneling, a small electron current I_t can be maintained between the tip and sample when a voltage V_t is applied.

The more common method of measurement is the constant-current mode where the tip is raster-scanned across the surface while I_t is kept constant at a set value by adjusting the distance to the surface. The height modulations are recorded at each point of the scan and these form the STM image of the surface topography.

Describing the tunneling process in STM is complicated for several reasons. We have little control over the condition of the metallic tip so describing its wave function becomes a difficult task. Furthermore, the simplifying assumption that the tip and surface are weakly interacting and thus can be treated within a perturbation scheme cannot be justified *a priori*. During tunneling, the tip and surface are so close together that a proper description ideally calls for treatment of the tip and surface as a whole.

Notwithstanding, the most useful STM theory to date is the Tersoff-Hamann (TH) formalism [58,59] which takes as its starting point tunneling theory results from Bardeen [60]. Here states which are approximate solutions to exact tip and sample Hamiltonians are introduced. The tip-sample interaction is then seen to be so weak that it can be neglected and the tunneling current can be evaluated based on the eigenfunctions ψ_ν of the surface and ψ_μ of the tip. It is important to note that ψ_ν and ψ_μ are nonorthogonal eigenfunctions of two different Hamiltonians as a result of the Bardeen approach.

The tunneling current, I_t , with voltage V_t applied, is given by

$$I_t = \frac{2\pi e}{\hbar} \sum_{\mu,\nu} f(E_\mu) [1 - f(E_\nu + eV_t)] |M_{\mu\nu}|^2 \delta(E_\mu - E_\nu), \quad (3.10)$$

where $f(E)$ is a Fermi function, E_ν and E_μ the eigenenergies of ψ_ν and ψ_μ in the absence of tunneling and $|M_{\mu\nu}|^2$ the tunneling matrix element between states ψ_ν and

ψ_μ . The latter is given by

$$M_{\mu\nu} = \frac{\hbar^2}{2m} \int d\mathbf{S} \cdot (\psi_\mu^* \nabla \psi_\nu - \psi_\nu \nabla \psi_\mu^*), \quad (3.11)$$

where the integral is over any surface lying inside the vacuum gap. In Eq. (3.10), we see that the difference between the energy levels of the tip and surface are shifted by eV_t due to the applied bias. Furthermore, the delta function implies elastic tunneling between (for positive bias on the surface) an empty state of the surface and a filled state of the tip, and *vice versa* for negative bias.

Since in most cases we have little control over the state of the tip, we are justified in choosing the simpler model, a spherical tip with local radius R and center of curvature \mathbf{r}_0 , thus retaining only s -wave contributions to the tip wave function. The even lower approximation, a point-like tip, would not be very satisfying since even the size of a single atom is comparable to the width of the vacuum gap. Evaluating $M_{\mu\nu}$, inserting into Eq. (3.10) and substituting typical metallic values for parameters multiplying the sum in Eq. (3.10), one obtains for the tunneling conductance:

$$G_t \equiv \frac{I_t}{V_t} \approx 0.1 R^2 e^{2\kappa R} \rho(\mathbf{r}_0, E_F) \quad (3.12)$$

$$\rho(\mathbf{r}_0, E_F) \equiv \sum_\nu |\psi_\nu(\mathbf{r}_0)|^2 \delta(E_\nu - E_F) \quad (3.13)$$

with $\kappa = \hbar^{-1}(2m\phi)^{1/2}$ the inverse decay length for the wave function in vacuum. Since we retained only s -waves in the tip wave function, $|\psi_\nu(\mathbf{r}_0)|^2 \propto e^{-2\kappa(R+z)}$, so

$$G_t \propto e^{-2\kappa z} = \exp(-1.025 \sqrt{\phi(\text{eV})} z(\text{\AA})). \quad (3.14)$$

Typical work functions ϕ for metals are in the eV range so we see that I_t changes by about an order of magnitude when z changes by 1 \AA . This explains the high resolution obtained in following the surface height and partly why atomic resolution can be achieved at all. The reason is that the strong exponential dependence of G_t causes most of the tunneling current to be run through a single atom—the one protruding furthest from the tip.

Equation (3.12) has a straightforward interpretation. The term $\rho(\mathbf{r}_0, E_F)$ is simply the surface local density of states (LDOS) at the Fermi energy, E_F , evaluated at the center of curvature of the tip, \mathbf{r}_0 . So with constant-current mode STM, we follow the contours of the surface with constant LDOS. This result is very useful since it relates the measured intensity to a property of the surface alone.

A crucial approximation of the TH formalism is the description of the tip wave function which only includes s -waves. While the near complete negligence of the tip geometry is dubious, it corresponds appropriately to the lack of knowledge we have about the condition of the tip. The spherical tip approximation then serves more as a way to include the finite size of the tip. Indeed, when using STM, one often encounters situations where the TH formalism breaks down. Whilst scanning, the tip often changes imaging mode, e.g. the STM image can suddenly invert owing to the influence from orbitals with magnetic quantum number $m \neq 0$ [48], or the imaging mode can simply change abruptly due to different electronic states at the tip apex.

3.2.2 STM image simulation

In Chap. 6 we shall make use of simulated STM images produced by N. Lopez from J. Nørskov's group to support the assignment of observed features on $\text{TiO}_2(110)$. This STM simulation method stems directly from the TH formalism described above. For constant-current operation with small bias, Eq. 3.10 shows that the STM tip follows contours of constant surface LDOS at E_F :

$$I \propto \sum_{\nu} |\psi_{\nu}(\mathbf{r}_0)|^2 \delta(E_{\nu} - E_F) \quad (3.15)$$

Here I is the local intensity in the experimental or simulated STM image. For STM imaging on bare metals, the positions of maxima in the LDOS topography generally coincide with the positions of the atomic nuclei. An adsorbate may however alter the LDOS in the surrounding area so that it is imaged as e.g. a depression even when sitting proud of the surface plane.

This latter effect becomes especially pronounced on oxide surfaces. An illustrative example can be found in Chap. 6 where it is shown that for the $\text{TiO}_2(110)$ surface, STM images are completely dominated by electronic effects causing the measured topography to be inverted compared to what would be expected on geometric grounds. TiO_2 being a semiconductor, it is also necessary to modify the conventional STM image simulation method to include the effect of finite bias since a ~ 1 V bias is required to overcome the 3 V band gap and reach unoccupied states. This can be included by integrating over available states in an energy range corresponding to the experimentally applied bias as follows:

$$I \propto \sum_{\nu} \int dE |\psi(\mathbf{r}_0)|^2 \omega(E) \quad (3.16)$$

$\omega(E)$ is a weight function that determines the contribution from different states. With a sample bias V there is a continuum of states (those with energies between E_F and $E_F + eV$) available for the tunneling process. This implies that $\omega(E)$ must be a window-like function designed to include all available states relevant in the tunneling process. The window-like function used in Chap. 6 is the difference between two Fermi functions, one each for sample and tip. This leads to the following expression:

$$\omega(E) = 1/(1 + \exp(\beta(E - E_F))) - 1/(1 + \exp(\beta(E + eV - E_F))) \quad (3.17)$$

The β factor essentially determines the width of the window function. This is illustrated in Fig. 3.1 where window functions of two different widths are inserted in the calculated LDOS of $\text{TiO}_2(110)$.

As also alluded to above, the TH approach to STM image simulation ignores any effects originating from the tip apex configuration and chemical composition (beyond the effect of an s -wave tip) as well as tip-sample interactions. While the neglect of tip effects confers well to our actual knowledge of and control over the tip state, the tip does have a profound influence on the imaging. An attempt is made at including tip effects in a second class of STM-image simulation methods. These methods go beyond

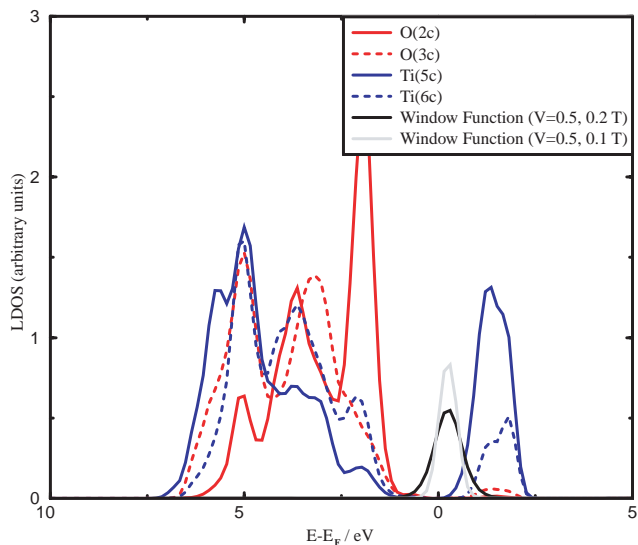


Figure 3.1: The surface LDOS of rutile $\text{TiO}_2(110)$. Contributions from different atomic species with different coordination numbers are as indicated by the figure legend. As will be relevant in Chap. 6, we see that at positive sample biases, the largest contribution to the tunneling intensity comes from five-fold coordinated Ti atoms.

perturbation theory and include a proper description of the interacting sample and tip within a scattering theory formalism.

One prominent implementation, the electron scattering quantum chemical (ESQC) approach due to Sautet and Joachim [61, 62], combines scattering theory and a generalized form of Landauer's theory for electron transport to calculate the tunnel current with adsorbates present². Sample and tip are modelled by two semiinfinite bulk solids connected by a cluster of 1–15 atoms to model the tip apex. Tip effects and tip-sample interactions are thus included. Conduction through the apex cluster is modelled as a scattering process. The atomic orbitals entering into the scattering calculation are obtained from a semiempirical Hückel calculation. An incoming electron from, for example, the tip electron reservoir is assumed to have a (small) probability of penetrating the barrier set up by the tunnel junction and proceed to the sample. Multiple-scattering events are also taken into account and this has been shown to be the main improvement on perturbative approaches such as the TH formalism [65]. The price to pay is a departure from the simple, intuitive concept of the STM topography corresponding to contours of constant LDOS at the Fermi level, but more profound details on the imaging mechanism can be extracted, such as a decomposition of the total tunneling current into separate

²The ESQC approach has been invoked successfully in collaborations between our group and theoretical groups for both simple adsorbates (CO) [63] and large organic molecules [64].

contributions from e.g. adsorbate and substrate, including the interference between the separate contributions, which turns out to have a strong effect on the resulting image.

3.3 *d*-band model

Large-scale computer calculations of adsorption properties can be viewed as computer experiments designed to mimic real experiments. It is however undesirable and computationally expensive to perform full calculations for every situation or system. There is thus a strong need to extract conceptual frameworks that capture the most prominent contributions to e.g. the binding energy of a given molecule to different surface sites. In other words, a connection between electronic structure and surface activity is desired. One such framework, which uses practically applicable concepts to bring out the essential physics involved, is the *d*-band model due to Hammer and Nørskov [66–68].

To introduce this model, we consider the interaction of an adsorbate state with the valence states of metal surface atoms, which distribute themselves into bands. *s* and *p*-derived states are highly itinerant and form broad bands while *d*-state energies fall in a relatively narrow range - a signature of small coupling between the localized *d* states. Figure 3.2a tracks the evolution in the resulting states when an adsorbate state interacts with a progressively narrower metal band. Interaction with a broad (*sp*-like) band leads to broadening into a resonance and a downshift in energy while interaction with a narrow (*d*-like) band leads to a split-up into bonding and antibonding states with energies above and below that of the adsorbate state, clearly similar to formation of molecular bonds. We also observe that as ϵ_d shifts up in energy, distinctive antibonding states are formed above the Fermi level. The consequent depopulation of these antibonding states leads to a stronger adsorbate-metal bond. Notice that when the original adsorbate state lies below the Fermi level, the resulting antibonding states can still shift above the Fermi level. From this discussion, we can extract a general principle: Stronger bonding results when antibonding adsorbate states are shifted above the Fermi level due to interaction with a narrow metal band. The same holds true if bonding states originating from an adsorbate states above the Fermi level shift below the Fermi level.

To illustrate both aspects of the above principle, in Fig. 3.2b the interaction between the CO $2\pi^*$ lowest unoccupied molecular orbital (LUMO) and 5σ highest occupied molecular orbital (HOMO) states and the transition-metal surface (here Pt(111)) is split up into two steps. First note that due to the different symmetries of the $2\pi^*$ and 5σ orbitals, they couple to different *d* orbitals and their interaction with the metal states can thus be treated separately.

The interaction with metal *s* bands is here represented by the projection onto the two CO orbitals of the DOS formed when CO adsorbs on the non-transition metal surface Al(111). The adsorbate states are seen to broaden and shift down in energy. The third set of curves shows the DOS projection of the states formed when CO adsorbs on the transition-metal surface Pt(111). In addition to the *s* interaction, now the resonances formed in the former interaction are split up into bonding and antibonding states lying below and above the resonance. Notice specifically that the bonding $2\pi^*$ -*d* states are shifted below the Fermi level while the antibonding 5σ -*d* states are shifted above the

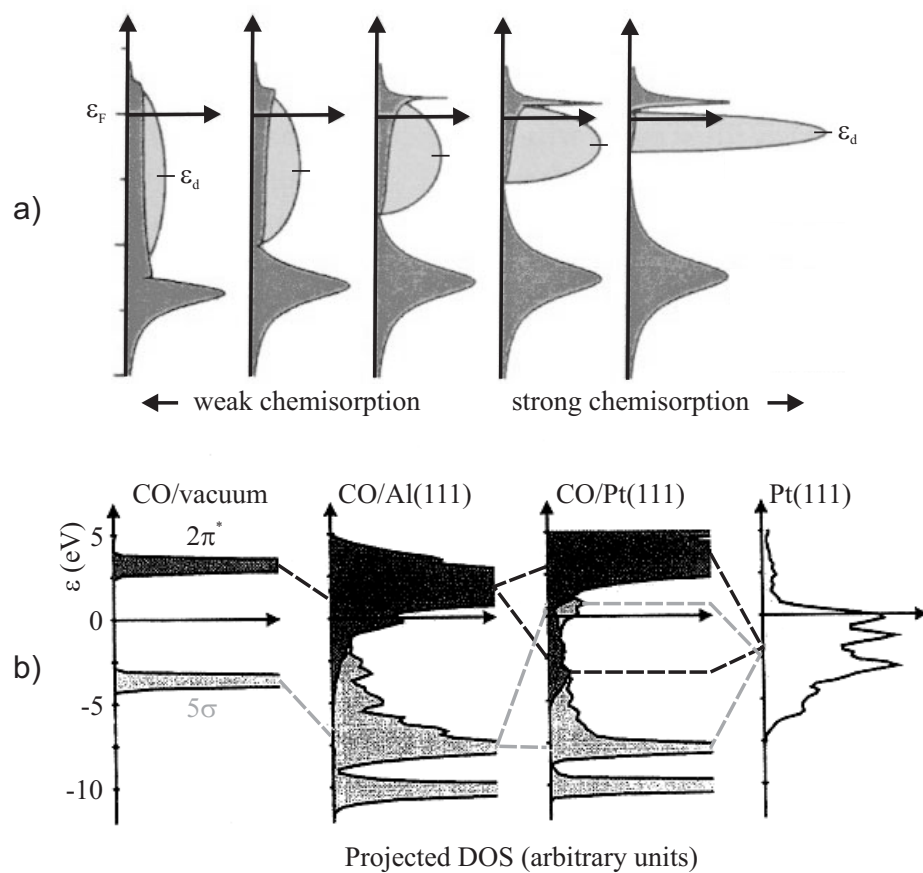


Figure 3.2: Interaction of atomic states with metal electronic bands. (a) Model calculation of the LDOS of an adsorbate state interacting with a metal band in and between the two limiting cases of broad and narrow bands. The band filling degree and interaction strength are kept constant so as the band narrows, the band center ϵ_d moves up. Light grey corresponds to the metal band, dark grey to the adsorbate state after interaction with the metal band. (b) Consecutive interaction of the molecular $2\pi^*$ and 5σ CO orbitals onto metal s and d -bands. The DOS is shown projected onto the $2\pi^*$ and 5σ CO orbitals. Downshift and broadening of the narrow CO orbitals upon coupling to the broad s -band as well as creation of bonding and antibonding states upon coupling to the narrow d -band are clearly observed. Adapted from [68].

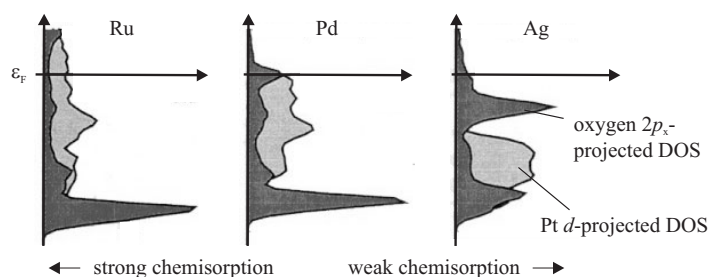


Figure 3.3: Variations in bonding behavior when moving through the transition-metal series represented by the DOS projection onto an atomic O $2p_x$ state (dark grey). The metal d DOS projection (light grey) shows the situation before interaction with oxygen. Adapted from [68].

Fermi level.

Both effects contribute to stronger bonding, as described by the general principle above. The $2\pi^*$ - d and 5σ - d however contribute differently to the bonding, the main difference being that the $2\pi^*$ state lies above the Fermi level prior to the d interaction where new bonding states are shifted below the Fermi level. Detailed calculations show that the $2\pi^*$ interaction dominates the bonding-strength variations between different metal and/or binding sites [68]. In a simplified description where the d -band width is neglected, the size of the $2\pi^*$ - d shift relative to ϵ_d is given by the coupling matrix element V and the difference $\Delta\epsilon = |\epsilon_d - \epsilon_{2\pi}|$ in energy between the d -band center and the adsorbate level. For $|V| \ll \Delta\epsilon$, the second-order perturbation results applies:

$$\Delta E_{\text{ad}} = \frac{V^2}{\epsilon_d - \epsilon_{2\pi}} \quad (3.18)$$

Before moving on, we note that the d -band model agrees very well with earlier conceptual models of CO binding on metal surfaces. The Blyholder model [69], the most frequently cited such model, describes the bonding process as occurring through electron donation from the 5σ HOMO orbital into metal sp and d orbitals and back-donation from the metal into the $2\pi^*$ LUMO orbital with a corresponding weakening of the CO bond. The donation and back-donation steps are in the d -band model separated into the s and d interactions.

It is now clear that the position of the metal d band relative to the Fermi level is crucial in determining the interaction strength between a transition-metal surface and an adsorbate. The position of the d band can be changed in a variety of ways but we shall restrict ourselves to two cases pertinent to later chapters. These are variations from one element to the next and second, variations between different facets of the same element. In other words, the latter effect concerns d -band position variations caused by changes in the local environment of the atom to which the adsorbate binds.

The *first* effect is demonstrated in Fig. 3.3, which shows the d -projected DOS of

the different metals before interaction with an oxygen adsorbate and the oxygen $2p_x$ -projected DOS after interaction. We see that the metal d -band center moves up when moving to the left in the periodic system. This has the effect of shifting more and more antibonding states above the Fermi level. For Ag, most antibonding states originating from the adsorbate- d band interaction are populated but for Ru most antibonding states are shifted well above the Fermi level. They thus become depopulated and stronger bonding results.

It is not very surprising that the choice of metal influences adsorbate binding energies but even on an elemental metal surface, a *second* effect can be exploited to change the d -band position and thus vary adsorbate binding energies. It concerns variations in the surface electronic properties caused by changes in the local geometric environment, e.g. coordination number, of the substrate atoms to which adsorbates bind [70], and will be highly relevant to the investigations CO/Pt in Chap. 5.

Figure 3.4 shows the correlation between the CO binding energy and the position of the local d -band center ϵ_d of the site to which CO binds on different Pt surfaces. The binding energy varies as much as 1 eV (or 100%) between the site with the highest (Pt(100)) and lowest (Pt(111)) coordination number. The explanation for this dramatic variation is again found in the properties of the d -band electrons pertaining to the binding site.

Figure 3.4b depicts how the width decreases and position of the d band shifts up for lower Pt coordination numbers. This is also expected from tight-binding theory since atoms with lower orbital overlap to neighboring atoms essentially become more “free-atom like”. When the d -band width decreases, the d -band center shifts up in response to maintain the band filling degree (for more than half-filled bands). According to Eq. 3.18, when ϵ_d and $\epsilon_{2\pi}$ approach, the binding energy increases. This means that the higher the d band, the stronger the CO binding. We thus expect stronger binding for under-coordinated sites, which is exactly what Fig. 3.4a shows. This effect forms the basis for Chap. 5 where we will see a whole range of structures form as a result of the strong dependence of the CO binding energy on the Pt coordination number.

3.4 Monte Carlo simulations

In Chap. 5 we shall make use of extensive Monte Carlo (MC) simulations in order to determine whether a surprisingly rough structure observed in the CO/Pt(110) system is a true equilibrium structure or rather the result of kinetic limitations. The Metropolis algorithm described below is perfectly suited for this purpose because it is a powerful tool for obtaining equilibrium configurations, which can be compared quantitatively to the experimentally observed structures. The following discussion is based on Refs. [21, 71].

One starts out by choosing a discrete grid, which represents the surface under investigation. On the grid is placed a number of particles which are allowed to interact with each other with specified interaction energies and perform random walk processes on the allowed sites such that the system will tend to approach lower-energy configurations. In a simple sampling MC scheme, all configurations are assumed to appear

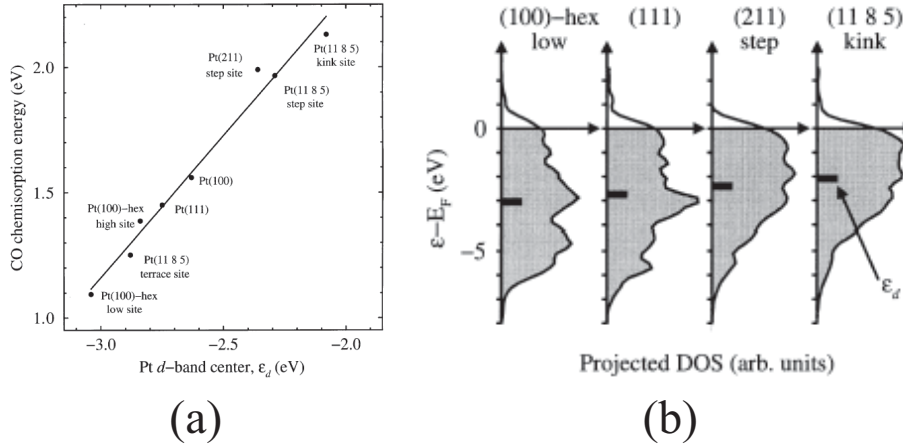


Figure 3.4: (a) Correlation between the CO binding energy and position of the d -band center for the adsorption site. (b) Variations in d -band width and position of the d -band center for progressively more open surfaces. Shown is the projection of the d density of states onto selected adsorption sites in the absence of adsorbates. When moving to the right in the figure, the width decreases and the center moves up. Reproduced from [70].

with equal probability (unity) but in a statistical average of a given observable A only low-energy configurations enter with significant weight:

$$\langle A(\mathbf{x}) \rangle = \frac{\int A(\mathbf{x}) \exp\left(-\frac{E(\mathbf{x})}{k_B T}\right) d\mathbf{x}}{\int \exp\left(-\frac{E(\mathbf{x})}{k_B T}\right) d\mathbf{x}} \quad (3.19)$$

Many redundant high-energy configurations are thus sampled. A way to sample only important configurations would be desirable and can indeed be achieved by using the Metropolis algorithm, a so-called importance sampling method, which allows for much faster convergence towards equilibrium. The basic idea is to reverse the meaning of probability and weight so that configurations enter with probability $\exp\left(-\frac{E(\mathbf{x})}{k_B T}\right)$ and unity weight. In this way, high-energy configurations are avoided.

In a MC simulation employing the Metropolis scheme, sampled states are not independent of each other, but instead the next state is formed from the present one, forming a so-called Markov chain of states. The probability distribution used to determine the next state is thus also only dependent on the present one. Each possible new state, \mathbf{x}_{i+1} , has a transition probability $w(\mathbf{x}_i \rightarrow \mathbf{x}_{i+1})$, which only depends on the energy difference between the two states. The Metropolis expression for w has the form:

$$w(\mathbf{x}_i \rightarrow \mathbf{x}_{i'}) = \min\left(\exp\left(\frac{E(\mathbf{x}_{i'}) - E(\mathbf{x}_i)}{k_B T}\right), 1\right) \quad (3.20)$$

The Metropolis algorithm runs as follows:

1. Determine a start configuration \mathbf{x}_i .
2. Create a new state $\mathbf{x}_{i'}$.
3. Calculate the transition probability $w(\mathbf{x}_i \rightarrow \mathbf{x}_{i'})$ from Eq. (3.20).
4. Choose a random number $r \in [0; 1]$. If $w(\mathbf{x}_i \rightarrow \mathbf{x}_{i'}) > r$, then set $\mathbf{x}_{i+1} = \mathbf{x}_{i'}$. Otherwise set $\mathbf{x}_{i+1} = \mathbf{x}_i$.
5. Repeat step 1–4 until equilibrium is reached.

Instead of using Eq. (3.19) for the average of an observable, now $\langle A \rangle$ can be calculated as the arithmetic average of the M last steps of the simulation run.

$$\langle A \rangle = \frac{1}{M} \sum_{m=N-M}^N A_m \quad (3.21)$$

where A_m is the value after step m . To avoid influence from the initial states, which are influenced by the initial setup, only the last M steps of the total number of steps in the simulation run, N , are included in the average.

As alluded to above, the Metropolis scheme is very effective in obtaining equilibrium configurations. The states leading up to the equilibrated states are physically meaningless so kinetic phenomena cannot be modelled. For this one has to turn to kinetic Monte Carlo methods, but we shall not describe these here as this will not be needed for the investigations on the CO/Pt(110) system in Chap. 5. Further details of the setup of the MC simulations for this system will be given there.

CHAPTER 4

Hydrogen on Cu(110)

This chapter describes the first high-pressure study, H/Cu(110), performed with the HP-STM described in Chap. 2. We demonstrate a close correspondence between previous UHV data and recently acquired HP data. The H/Cu(110) system is a classical example of activated adsorption. The activation barrier for H₂ dissociation on Cu(110) carries with it an extremely low sticking coefficient. Consequently the present system is very sensitive to even minute amounts of impurities with high sticking coefficients, like O₂, in the gas phase. As a result of this, we present the formation of a new oxygen-related structure on Cu(110) formed when exposing the surface to slightly O-contaminated H₂.

4.1 Introduction

The H/Cu system is a classical model system for activated dissociative chemisorption [72–75] and is extremely important from a technological viewpoint in both the methanol synthesis [76] and the water gas shift reaction [7, 77, 78]. Hydrogen adsorption is found to induce $(1 \times 1) \rightarrow$ missing-row (1×2) surface restructuring [79–82]. For the reverse water-gas shift reaction ($\text{CO}_2 + \text{H}_2 \rightarrow \text{H}_2\text{O} + \text{CO}$) in particular, this surface restructuring process is found to have a profound influence on the reaction rate. The experimental data from microreactor experiments [78] are explained by assigning a higher rate for the rate-limiting step, dissociation of CO_2 , on (1×2) reconstructed areas.

Here we present experimental results for the adsorption of hydrogen on Cu(110) and demonstrate the possibility of bridging the pressure gap at the atomic level. *In situ* STM imaging of a metal surface structure, and the accompanying adsorbate-induced reconstruction, in equilibrium with the gas phase at pressures up to 1 bar at room temperature, is demonstrated. A detailed comparison with previous UHV studies reveals that the Cu(110) surface responds identically to hydrogen at UHV pressures and at atmospheric pressures. From the HP-STM data we derive quantitative values for the rate constants for adsorption and desorption that compare favorably with previously reported UHV values.

4.2 *In situ* STM imaging

Figure 4.1 depicts a sequence of STM images of the Cu(110) surface obtained before H_2 exposure (a), at an ambient H_2 pressure of 1 bar (b), and finally after subsequent evacuation of the HP cell (c). It is apparent that upon H_2 exposure at 1 bar the surface reconstructs into the well-known (1×2) missing row structure with every second close-packed $[1\bar{1}0]$ Cu row expelled [32, 80–82]. After evacuation of the HP cell, the surface reconstruction is lifted and only a (1×1) surface structure is observed. This implies that during the time between evacuation of the HP cell and resumption of imaging (~ 1500 s), sufficient hydrogen must have been depleted from the surface for the reconstruction to lift. Subsequent AES and STM measurements showed that no impurities were present on the surface after the high-pressure treatment.

In order to investigate the pressure dependence of the H-induced reconstruction, STM imaging was performed at a range of different H_2 pressures between UHV and 1 bar (marked with arrows in Fig. 4.2). Figures 4.2a and b show two STM images obtained at 2 and 20 mbar H_2 , respectively. At 2 mbar only a (1×1) structure is observed, while at 20 mbar the surface consists of large areas ($>100 \times 100 \text{ \AA}^2$) displaying the (1×2) reconstruction, as well as (1×1) domains (insert Fig. 4.2b). This means that (1×2) nuclei formation starts somewhere between 2 and 20 mbar (light blue area in Fig. 4.2c). The sole observation of the bare Cu lattice at 2 mbar (Fig. 4.2a) — even after hours of exposure — provides a direct proof that we have well-defined conditions with no impurities present in the gas, since practically all molecules have higher sticking probability on Cu than H_2 . At 20 mbar, atom-resolved imaging could only be obtained on non-reconstructed (1×1) domains (insert in Fig. 4.2b). In regions where the (1×2) phase

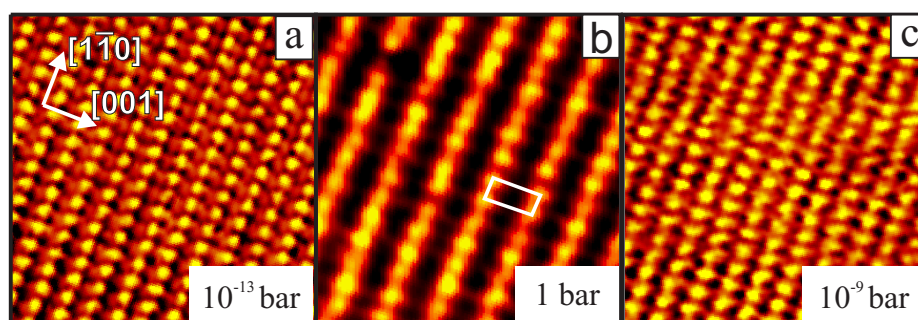


Figure 4.1: A sequence of atom-resolved STM images recorded at $T=298$ K in the HP-STM depicting the Cu(110) surface (a) *before* H_2 exposure. ($I=1.42$ nA, $V=105$ mV); (b) *during* exposure to 1 bar of H_2 (the image is recorded 1 h 50 min. after exposure ($I=1.55$ nA, $V=29.3$ mV); and (c) after ~ 1500 s *after* evacuating the HP cell ($I=1.06$ nA, $V=-4.9$ mV). The unit cell of the (1×2) missing-row structure is indicated in (b) ($2.55 \times 7.22 \text{ \AA}^2$). All figures are drawn on the same scale ($46 \times 45 \text{ \AA}^2$).

had nucleated, protruding domains, which were not stable over time, as well as deeper layers (dark regions), were also observed. The former protrusions (“disordered” structure in Fig. 4.2b) are probably due to rapidly diffusing Cu atoms [83] that are present on the surface during the formation of the (1×2) phase and which interfere with the measurements. In these experiments, Ar was additionally admitted to the HP cell so that for all H_2 partial pressures the total pressure was always 1 bar. This is necessary to avoid discharging between the piezoelectric scanner tube electrodes of the STM in the 10^{-3} to 10 mbar regime.

The binding state of the adsorbed H was determined by TPD. Figure 4.3b shows a TPD spectrum after 15 minutes exposure at 1 bar, recorded after a delay time between exposure and the TPD experiment of 1200 s. The TPD spectrum is characterized by a small peak at $T=340$ K. This is interpreted as H_2 originating from H adsorbed on the Cu(110) surface, consistent with previous studies [72, 84]. The amount of H_2 was calibrated by comparing with TPD spectra obtained from a saturated Cu(110)- (1×2) -H structure prepared in UHV by exposing the surface to atomic H formed by pre-dissociation of H_2 on a hot tungsten filament. The surface prepared in this manner is characterized by a sharp (1×2) LEED pattern (Fig. 4.4) and a TPD peak at $T=345$ K, and is known to saturate at a coverage of $\theta_{\text{sat}} = 0.5$, i.e. 1 H atom per (1×2) surface unit cell [81] (see Fig. 4.3a). Using this latter TPD peak as a reference, the absolute amount of surface H can be determined, see Fig. 4.3b. The low surface coverage of H in these TPD experiments can easily be accounted for by desorption occurring during evacuation and transfer to UHV prior to TPD when the sample is held at room temperature. By varying the time between evacuation and TPD and assuming first-order desorption (see below), the H desorption rate constant is determined to be $k_d = (1.2 \pm 0.1) \cdot 10^{-3} \text{ s}^{-1}$.

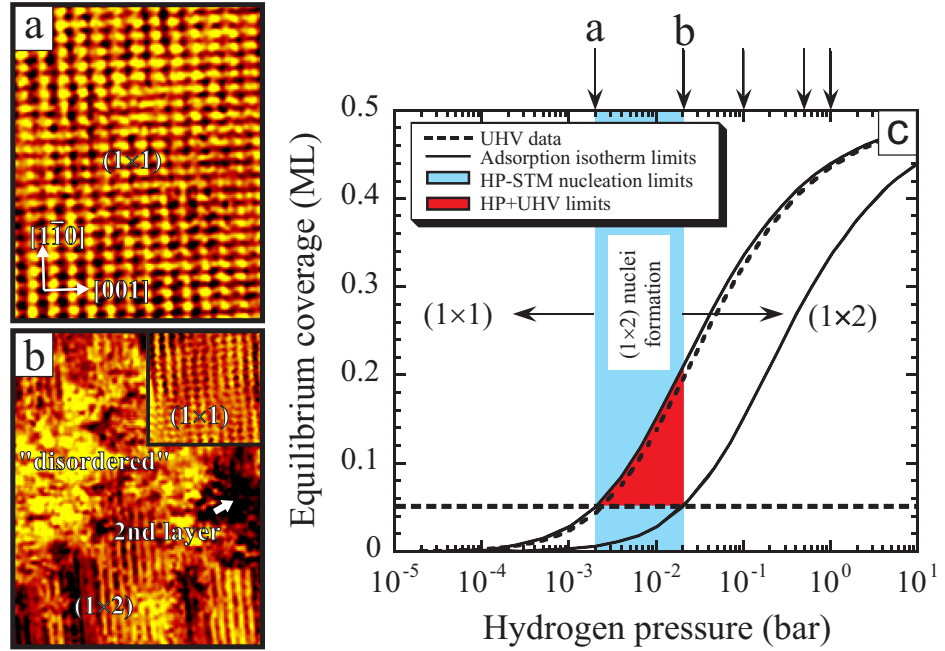


Figure 4.2: (a) STM image depicting the (1×1) surface structure at $P_{H_2} = 2$ mbar ($47 \times 57 \text{ \AA}^2$), and (b) the mixed (1×2) and (1×1) surface structures at $P_{H_2} = 20$ mbar ($178 \times 221 \text{ \AA}^2$). The latter structure is shown with atomic resolution in the insert in (b) ($40 \times 40 \text{ \AA}^2$). Patches of “disordered”, protruding regions (bright color) and holes in the lattice (dark color), respectively, are visible on the surface where the nucleation of the (1×2) restructuring occurs. (c) Pressure dependence of the (1×1)→(1×2) H-induced reconstruction at $T=298$ K. The arrows at the top abscissa show the different pressures at which HP-STM imaging was performed. The light blue area shows the pressure regime in which the (1×2) reconstruction occurs. The region enclosed by the thin solid lines marks the lower and upper limits of the equilibrium coverage vs. pressure as deduced from the HP-STM measurements. The equilibrium coverage is given by $\theta_{eq} = 1/2 + \alpha - \sqrt{\alpha(\alpha + 1)}$, where $\alpha = k_d/4k_a P_{H_2}$. The horizontal dashed line indicates the low coverage limit ($\theta \gtrsim 0.05$) for (1×2) nucleation, as determined from UHV studies. The curved dashed line shows the adsorption isotherm obtained using available UHV data (see text). Finally, the dark red region indicates the combined high pressure and UHV limits where the surface reconstruction is initiated.

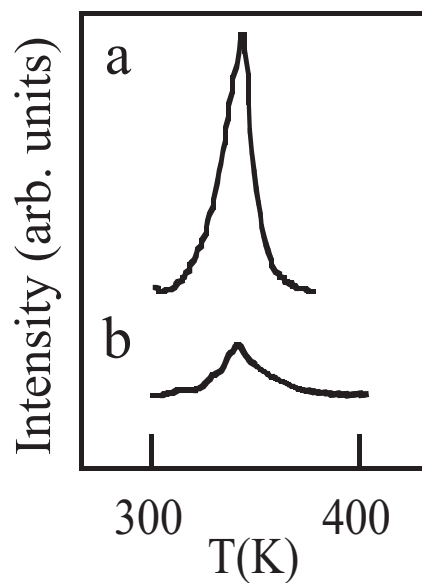


Figure 4.3: TPD spectra showing the H_2 desorption, $m/Z=2$. (a) Spectrum from a saturated Cu(110) ($\theta_{\text{H}} = 0.5$) surface prepared by adsorption of atomic H in UHV at $T=220$ K and (b) from the Cu(110) surface after 15 min. exposure to 1 bar of H_2 at $T=298$ K. The latter spectrum is recorded after a time lapse of 1200 s between evacuation of the HP cell and transfer to UHV. The H coverage is determined to be $\theta = 0.10 \pm 0.02$ in this case. The heating rate was 2 K/s for both spectra.

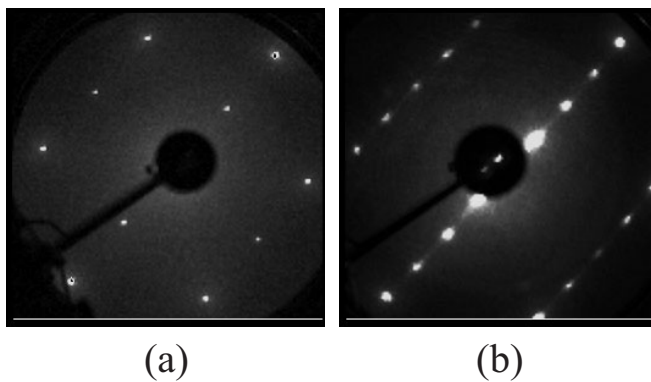
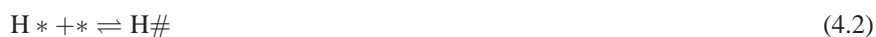


Figure 4.4: LEED pattern from Cu(110) exposed to atomic H. (a) LEED pattern of the clean (1×1) surface, 120.0 eV, and the (b) (1×2) -H surface, 122.8 eV. Half-order spots are clearly recognized in (b).

4.3 Quantitative comparison

A large database of UHV studies of the H/Cu(110) system exists [32, 72, 73, 80–82, 84], which allows us to scrutinize the validity of the “surface science approach” to predict corresponding high pressure phenomena. Adsorption of *atomic* H (Eqs. 4.1 and 4.2) leads to the $(1 \times 1) \rightarrow (1 \times 2)$ reconstruction at $T > 140$ K [80–82]. Above $\theta_{\text{H}} \geq 0.05$, small (1×2) nuclei form. Adsorption of atomic H has primarily been performed by means of pre-dissociation on a hot tungsten filament, although pre-dissociation by thermal cracking in a hot nozzle arrangement has also been reported [84]. Adsorption of atomic H occurs readily, and the sticking coefficient for H produced by thermal cracking in a $T=1815$ K nozzle is $\sim 18\%$ [80]. According to vibrational studies with HREELS, the hydrogen atoms sit in tilted trigonal sites with a mirror axis parallel to the $\langle 001 \rangle$ azimuth.

The relevant elementary steps for adsorption of atomic H can be written as follows:



where $*$ and $\#$ denote adsorption sites on the unreconstructed and (1×2) reconstructed surface, respectively. For dissociative molecular adsorption, the corresponding steps become:



Here we implicitly assume that no free adsorption sites exist on the reconstructed surface since these are induced by the presence of H and cannot exist on a H-free surface.

Dissociative adsorption of H_2 can be achieved by using a molecular beam [72] or a thermal bath [73] to supply the incoming molecule with sufficient internal and translational energy to overcome the dissociation barrier. Reported TPD spectra are similar to those obtained after adsorption of atomic H. No structural analysis has been performed after exposure to molecular hydrogen although TPD experiments suggest that the adsorption state is similar to the case of atomic H. In one case, high-pressure exposure has been used to compensate for the low sticking probability. In this latter study, the adsorption of a H_2 gas was studied in the range $T=470\text{--}720$ K by reactive ‘titration’ experiments with pre-adsorbed oxygen, from which the H_2 sticking probability and the activation barrier for adsorption were deduced [73]. A value of $E_{\text{ad}}=14.3 \pm 1.4$ kcal/mole $= 0.62 \pm 0.06$ eV is reported; this value enters in an expression for the sticking probability as

$$s(T) = s_0 \exp(-E_{\text{ad}}/kT) \quad (4.5)$$

with $s_0 = 10^{0.03 \pm 0.16} \text{ s}^{-1}$. Extrapolation to room temperature yields $s(T=298 \text{ K}) = 3 \cdot 10^{-11} \text{ s}^{-1}$.

For both atomic and molecular adsorption, the saturation coverage is found to be $\theta_{\text{sat}}=0.5$ with respect to the number of Cu atoms in the (1×1) unit cell.

Turning now to the desorption behavior, all authors find a single desorption peak at 330–360 K, which does not shift with coverage [79, 80, 84]. The desorption has been characterized as first order and is proposed to be due to reaction step (4.4), i.e. the desorption rate is proportional to θ_H . This suggests that the rate-determining step is associated with restructuring of the surface (Eq. 4.4) rather than associative H_2 desorption. Two sets of values for the Arrhenius prefactor and activation energy have been reported:

$$k_d = \nu_d \exp(-E_d/kT) \quad (4.6)$$

(ν_d, E_d) = ($5 \cdot 10^{11 \pm 1} \text{ s}^{-1}, 0.88 \pm 0.07 \text{ eV}$) [81] or ($1.6 \cdot 10^{13 \pm 1} \text{ s}^{-1}, 0.8 \pm 0.1 \text{ eV}$) [82].

We may in a very direct way compare the rate constants for adsorption, k_a , and desorption, k_d , derived from previous UHV studies quoted above, with the high-pressure STM data. Neglecting the rate of diffusion into the bulk, which is small [85], the kinetic equation describing the adsorption and desorption is given by

$$\frac{d\theta}{dt} = 2k_a P(\theta_{\text{sat}} - \theta)^2 - k_d \theta = 2k_a P(\theta^2 - (1 + 2\alpha)\theta + 1/4) \quad (4.7)$$

with

$$\alpha = \frac{k_d}{4k_a P}$$

and P the partial pressure of H_2 and $\theta_{\text{sat}} = 0.5$. The first term describes the adsorption process, and is proportional to the background pressure and the deviation from saturation coverage ($\theta_{\text{sat}} - \theta$) squared since H_2 adsorbs dissociatively. The second term, the desorption term, subtracts from the coverage and is found to be first order, as described above. The latter equation can be integrated to yield an expression connecting time and coverage.¹ The final result is:

$$t = \frac{1}{2k_a P(\theta_2 - \theta_1)} \left\{ \ln \left(1 - \frac{\theta}{\theta_2} \right) - \ln \left(1 - \frac{\theta}{\theta_1} \right) \right\} \quad (4.9)$$

¹The details are:

$$t - t_0 = \frac{1}{2k_a P} \int_{\theta_0}^{\theta} \frac{d\theta}{\theta^2 - (1 + 2\alpha)\theta + 1/4}$$

To solve this integral analytically, one needs to factorize the denominator as follows:

$$\theta^2 - (1 + 2\alpha)\theta + 1/4 = (\theta - \theta_1)(\theta - \theta_2)$$

with

$$\theta_1 = 1/2 + \alpha - \sqrt{\alpha(1 + \alpha)} \quad (4.8)$$

$$\theta_2 = 1/2 + \alpha + \sqrt{\alpha(1 + \alpha)}$$

and the integral can be rewritten to:

$$\begin{aligned} t - t_0 &= \frac{1}{2k_a P(\theta_2 - \theta_1)} \int_{\theta_0}^{\theta} \left(\frac{1}{\theta - \theta_2} - \frac{1}{\theta - \theta_1} \right) d\theta \\ &= \frac{1}{2k_a P(\theta_2 - \theta_1)} \left\{ \ln \left(\frac{\theta_0 - \theta_1}{\theta_0 - \theta_2} \right) - \ln \left(\frac{\theta - \theta_1}{\theta - \theta_2} \right) \right\} \end{aligned}$$

We note that $\theta_2 > \theta_1 > 0$ so from equation (4.9) we see that for $t \rightarrow \infty, \theta \rightarrow \theta_1$ so $\theta_1 \equiv \theta_{eq} = 1/2 + \alpha - \sqrt{\alpha(1 + \alpha)}$, the equilibrium coverage.

The time to reach equilibrium coverage at low H_2 pressures is quite long, which is important to keep in mind when preparing the surface. For instance, from equation (4.9) we can calculate the time to reach 95% of the equilibrium coverage at $P_{H_2}=2$ mbar to be ~ 1500 s.

The HP-STM data provide a narrow window for the onset of the (1×2) reconstruction as a function of H_2 pressure ($2 \lesssim P_{H_2} < 20$ mbar). UHV data indicate that (1×2) nuclei formation starts at $\theta \gtrsim 0.05$ [80–82] (horizontal dashed line in Fig. 4.2c). Furthermore, using $\theta_{eq} = 1/2 + \alpha - \sqrt{\alpha(1 + \alpha)}$, this implies that the H equilibrium coverage must be $\theta_{eq} \lesssim 0.05$ at $P_{H_2} = 2$ mbar, and $0.05 \lesssim \theta_{eq} < 0.21$ at $P_{H_2} = 20$ mbar, or equivalently $4.1 \cdot 10^{-3}/P_{H_2}[\text{bar}] < \alpha < 4.1 \cdot 10^{-2}/P_{H_2}[\text{bar}]$, where $\alpha \equiv k_d/4k_aP$. Using these limits, we obtain the region enclosed by the thin solid lines in Fig. 4.2c. This reduces the region in pressure-coverage space where the nucleation of the (1×2) reconstruction occurs to the dark red region in Fig. 4.2c.

The HP-STM data reported here considerably narrow down the uncertainty in α (or k_d/k_a). Using the value for k_d determined from the post-TPD measurements we find that $7.3 \cdot 10^{-3} < k_a < 7.3 \cdot 10^{-2} \text{ s}^{-1} \text{ bar}^{-1}$, which is in good agreement with previously reported values for $k_a = 3.4 \cdot 10^{-2} \text{ s}^{-1} \text{ bar}^{-1}$ [73]. Scrutinizing the rate constants for desorption reported from UHV studies, which show significant spread [72, 81, 82], we find the best agreement with $k_d = \nu \exp(-E_d/k_B T) = 6.6 \cdot 10^{-4} \text{ s}^{-1}$ [81], which is consistent with the α limits imposed by the HP-STM data and the reported k_a values. Figure 4.2c shows the adsorption isotherm using this latter value of k_d (curved dashed line). Clearly the UHV data show remarkably good agreement with the high-pressure data reported here.

4.4 Impurity-related structures

In the high-pressure experiments described above, the gas cleanliness is crucial because of the low sticking coefficient of H_2 on Cu ($s = 3.4 \cdot 10^{-11}$ at $T=298$ K) [73], which means that even minute amounts of impurities (such as CO, O_2) in the gas would dominate the adsorption behavior. Below we demonstrate the outcome of a series of detailed experiments where the influence of gas impurities in the H_2 gas were investigated. We found that the H_2 gas contained oxygen impurities (probably mainly molecular oxygen; the only spectroscopically detected species was O on the Cu surface).

As delivered, the level of O_2 impurities in the hydrogen gas is < 0.2 ppm, but this is, as we will show below, enough for oxygen to completely alter the surface structure and hence the H_2 behavior. This is not surprising considering that the initial sticking coefficient of oxygen on Cu is close to one. To further clean the hydrogen it was necessary to run it through the catalyst bed and molecular sieve as discussed in Sec. 2.2.5.

The findings presented in this section will demonstrate the necessity of carefully considering the handling of gases used in high-pressure experiments. However, it turned out that the results obtained with the "contaminated" gas revealed a new Cu structure, and are therefore interesting in their own right.

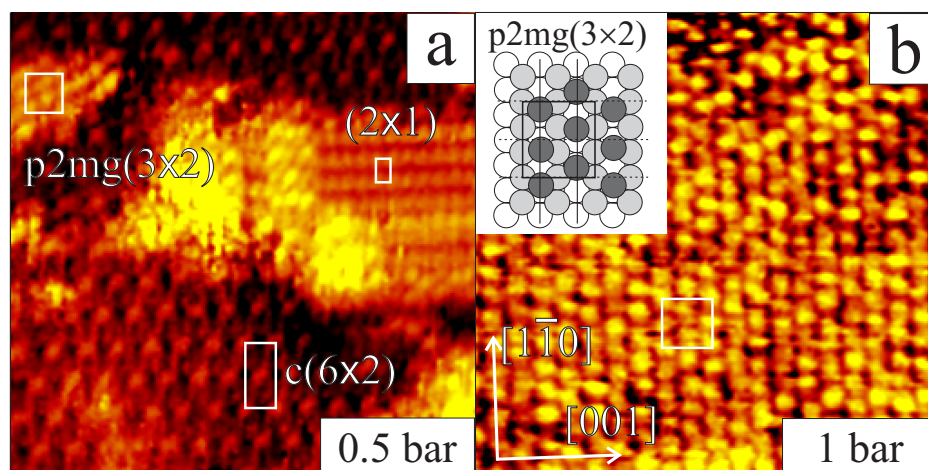


Figure 4.5: Oxygen-induced structures on Cu(110) formed as a result of high-pressure exposure to O-contaminated H_2 gas. (a) Three coexisting structures at a hydrogen pressure of 0.5 bar ($100 \times 100 \text{ \AA}^2$). (b) Fully developed (3×2) - $p2mg$ -O structure at a hydrogen pressure of 1 bar ($70 \times 70 \text{ \AA}^2$). The inset shows the arrangement of top-layer Cu atoms. The (3×2) unit cell is indicated and full and dashed lines mark the mirror and glide lines belonging to the $p2mg$ space group, respectively. From the STM and LEED analysis alone, we are not able to determine the position of O atoms.

Fig. 4.5a shows the Cu(110) surface imaged under 0.5 bar of H_2 *used as delivered*. Three structures coexist at the time of imaging, which despite the fact that no controlled dosing of oxygen was performed, can unequivocally be attributed to oxygen-induced structures. The evidence for this is post-exposure AES analysis, which reveals only O as a main contaminant from the “ H_2 ” exposures. Furthermore, two of the structures seen in Fig. 4.5a have previously been observed in UHV studies of oxygen adsorption on Cu(110): the Cu(110)- (2×1) -O added-row structure and the Cu(110)- $c(6 \times 2)$ -O structure [32].

The third structure visible in Fig. 4.5a, which is fully developed in Fig. 4.5b after long-time exposure (ca. 1 h) at a (contaminated) hydrogen pressure of 1 bar. This latter structure has not been reported before and indicates that high-pressure exposures of the Cu surface to O_2 induce a succession of surface reconstructions of which only a few (those that form at the lowest exposures) have been observed. The new structure found has a pseudo-hexagonal structure with an apparent periodicity of 3.80 \AA in the $[1\bar{1}0]$ direction and 7.20 \AA in the $[001]$ direction, corresponding to a $p(3 \times 2)$ structure with respect to the unreconstructed Cu(110) surface.

A detailed LEED analysis reveals that this structure can be classified as a Cu(110)- (3×2) - $p2mg$ -O structure. Figure 4.6 shows the LEED pattern of the Cu(110) surface for the clean surface (a), after exposure to high-pressure H_2 for 10 min. (b), and after

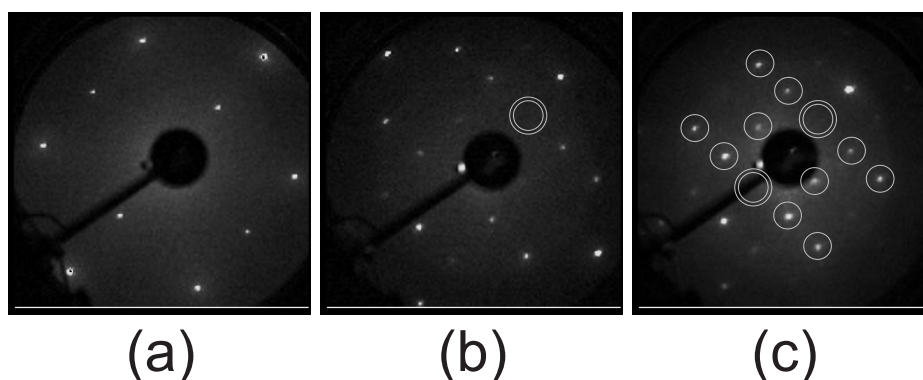


Figure 4.6: LEED patterns from impurity-induced structures. (a) Clean Cu(110) (59.8 eV), (b) Cu(110) exposed to contaminated H₂ for 10 min. (59.8 eV), and (c) as b but annealed to 400 K (78.8 eV). Single grey rings mark $(1/3, x)$ and $(2/3, x)$ reflections, hollow rings marks $(0, n/2)$ reflections missing due to a $(0, 1)$ glide line.

annealing the exposed surface to 400 K (c). This latter annealing treatment improved the surface ordering and produced sharper LEED patterns. From Fig. 4.6, it is evident that the HP-exposed surface indeed exhibits a $p(3 \times 2)$ structure, which is fully consistent with the STM data. The striking feature is the “ I/V characteristics” of the fractional-order spots, namely the $(1/3, 0)$ and the $(2/3, 0)$ (marked with light grey rings in Fig. 4.6b), and the $(0, 1/2)$ (marked with hollow rings in Fig. 4.6b). Whereas the $(1/3, 0)$ and the $(2/3, 0)$ spots are visible at some energies, however weak, and sometimes also simultaneously, the $(0, n/2)$ spots are never observed. The fact that these spots are systematically missing indicates that the structure contains a glide line in the $(0, 1)$ direction, causing the half-order spots along the glide line to be extinguished, thus reducing the possible space group to the $p2mg$ space group.

Upon longtime exposures of Cu(110) in 1 bar H₂ at room temperature, large-scale mesoscopic deformations of the Cu(110) surface are observed. Post-exposure AES indicates that the only major surface species is oxygen originating from the “contaminated” H₂ gas. As depicted in Fig. 4.7, stripes consisting of adjacent troughs and ridges are formed along the $[001]$ direction, and between the stripes, terraces exhibiting the $p2mg(3 \times 2)$ -O structure are observed. The length scale of the stripes is of the order $0.1\text{--}1 \mu\text{m}$. The width of the stripes are in the range $50\text{--}100 \text{ \AA}$ and the height difference of the troughs and ridges is typically 6 \AA with respect to the nearby terrace. The observation of these stripes indicates that the surface undergoes a massive surface reconstruction upon exposure to high doses of oxygen beyond the level of simple surface reconstruction, hence involving significant mass transport. The same structure was observed after evacuation when scanning in UHV. Annealing the sample to successively higher temperatures (403 K, 530 K, 628 K, and 733 K) with subsequent STM imaging in between revealed that the mesoscopic features disappeared. Long-range ordering improved after

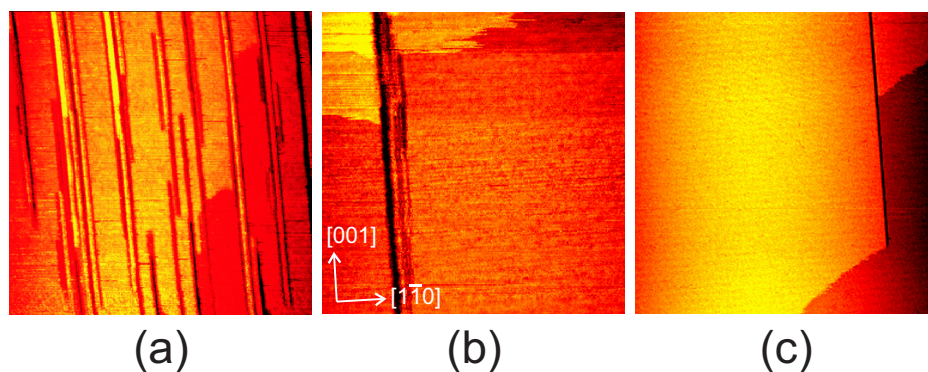


Figure 4.7: Temperature stability of mesoscopic structure created upon exposure to oxygen-containing H_2 . Stripes consisting of adjacent troughs and ridges are formed along the $[001]$ direction. Long-range ordering is improved upon annealing. (a) 300 K, $0.16 \times 0.16 \mu\text{m}$, (b) As a, but annealed to 530 K, $0.11 \times 0.10 \mu\text{m}$, and (c) as b but annealed to 628 K, $0.21 \times 0.216 \mu\text{m}$

annealing to 530 K, and the $p2mg(3 \times 2)$ structure disappeared after annealing to 733 K, leaving only the unreconstructed Cu(110) surface.

The maximum oxygen exposure reached in the impure hydrogen experiments (1 h at 1 bar H_2 with a 0.2 ppm oxygen impurity level at room temperature) is about $5 \cdot 10^5 \text{ L}$. The structure observed after an equivalent exposure to pure oxygen at room temperature is shown in Fig. 4.8. Interestingly, this does *not* produce the $p2mg(3 \times 2)$ structure but rather the $c(6 \times 2)$ structure observed in UHV studies. Exposure to even higher doses at room temperature produces a disordered structure with no apparent order (not shown), which may be a sign of the formation of an oxide layer. The observation of an amorphous oxide layer after room-temperature exposure is consistent with earlier studies [86, 87], where formation of Cu_2O is observed. Higher temperatures are needed for ordered structures to form. We know from the previous section that H_2 by itself induces a reconstruction of the Cu(110) surface with a concomitant transport of Cu atoms so we are inevitably lead to the conclusion that H_2 promotes the formation of the $p2mg(3 \times 2)$ presented above. Having said this, we also cannot exclude the possibility that the $p2mg(3 \times 2)$ structure incorporates H in some form. From a catalysis point of view, the results presented here are quite important since small levels of impurities (especially oxygen, or oxygen-containing species) are almost always present under realistic conditions.

4.5 Conclusion

We have bridged the pressure gap at the atomic level by using of a HP-STM. We have shown that for the H/Cu(110) system, the surface reconstructs into the (1×2) missing-

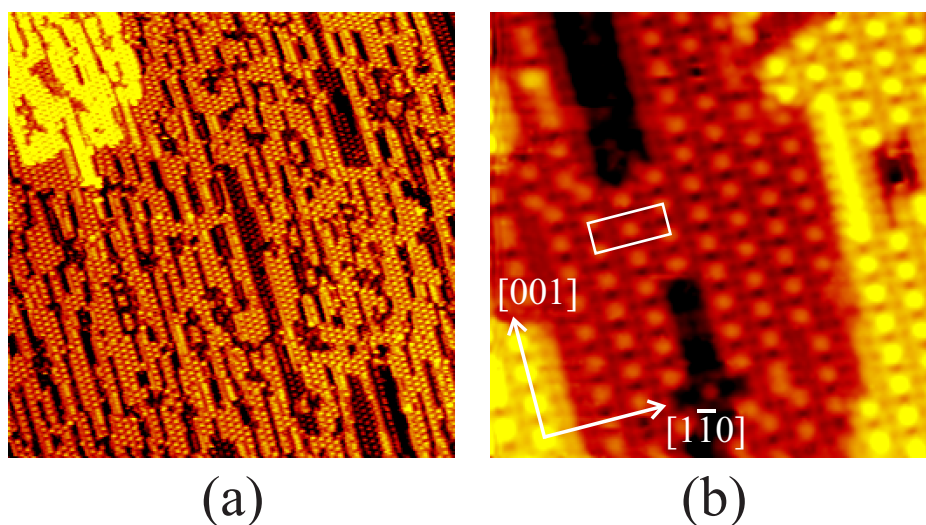


Figure 4.8: Exposure to large doses of pure oxygen (7.2 mbar, 120 s). A disordered $c(6 \times 2)$ structure covers the entire surface. (a) $500 \times 500 \text{ \AA}^2$. (b) $100 \times 100 \text{ \AA}^2$.

row structure at H_2 partial pressures >2 mbar and thus responds identically to H_2 in UHV and at atmospheric pressures. The results imply that raising the pressure is equivalent to lowering the temperature, which is usually what is done in UHV studies in order to study high-coverage structures. This is important since it constitutes the basis for numerous well-characterized and well-controlled UHV studies aimed at elucidating related gas-surface reactions, even at “real” reaction conditions, and it provides support for the surface science approach.

The importance of careful gas handling when carrying out high-pressure experiments with low sticking-coefficient gasses has been proven. The presence of oxygen-induced structures on Cu(110) were shown to completely dominate the surface structure when using hydrogen gas as-delivered, despite the high purity of the as-delivered gas. Further cleaning through a dedicated gas system consisting of a catalyst bed and a molecular sieve was necessary. A new O-induced structure was found and it was demonstrated that the Cu(110) surface reconstructs on both the atomic and the mesoscopic scale upon longtime exposures to oxygen-containing H_2 gas.

CHAPTER 5

CO adsorption on Pt at low and high pressure

This chapter is devoted to a direct comparison between UHV and high-pressure CO adsorption on two different platinum facets, Pt(111) and Pt(110). In the former system, no substrate modifications occur as a result of CO adsorption while the latter case involves extensive substrate restructuring. The investigations on these two systems allow us to draw the conclusion that no new adsorption structures are formed as long as kinetic limitations are taken properly into account. We shall see examples where gas dosing at too low temperatures causes metastable adsorbate and/or substrate structures to be formed due to kinetic hindrances. For both Pt systems, we thus bridge the pressure gap and conclude that no new physics need be invoked to explain any of the results.

5.1 Introduction

CO chemistry on transition-metal surfaces is of enormous technological importance. CO derived from coal and other carbon sources are in so-called Fischer-Tropsch reaction reduced by hydrogen into methane and higher hydrocarbons in the presence of a supported transition-metal catalyst. Simple examples are methane production from synthesis gas



and the formation of methanol



from which a multitude of chemical products are produced.

The most important application for Pt in particular is oxide-supported Pt clusters, which form one of the active components in the automotive three-way catalyst. The Pt clusters serve as a catalyst for oxidation of CO and unburned hydrocarbons [13].

Recently, CO adsorption on Pt surfaces has attracted even more attention due to the poisoning effect of CO in low-temperature fuel cells when Pt serves as cathode or anode material. CO is always present in the H₂ stream which is produced in the steam reforming reaction from hydrocarbons, i.e. the reverse of reaction (5.1). Since CO binds strongly to Pt and blocks H₂ dissociation sites, has to be removed from the gas stream passing through the Pt anode [88]. The use of alloys as anode materials to avoid this poisoning effect has an interesting connection to the discussion of the *d*-band model in Sec. 3.3. One promising candidate is a Ru/Pt alloy where the bonding of CO and H, and thus the H/CO coverage, can be tuned by varying the Ru/Pt ratio [20]. Inclusion of Ru into the Pt lattice can be imagined to shift the metal *d*-band center with a concurrent change in reactivity to obtain a better functioning catalyst. The trick is to tune the *d*-band position to facilitate H₂ dissociation at a high enough rate and at the same time prevent CO from binding too strongly to the H₂ dissociation site. This kind of optimization is a natural part of the design of a real catalyst and the optimal formulation provides the best trade-off between desired and detrimental processes.

Other than its technological importance, knowledge of CO chemistry on transition-metal surfaces lies at the core of our understanding of chemical surface reactions. Despite its relative simplicity, the CO molecule and the substrate transformations induced by it display surprisingly complex adsorption behavior, as will be amply illustrated in this chapter.

On transition metals, CO is bonded through the C atom, mostly with its molecular axis perpendicular to the surface plane. Under some conditions though, the molecular axis has been found to be tilted [89, 90], as we will also see in Sec. 5.3. In Sec. 3.3, CO bonding on Pt was used as an example to illustrate the *d*-band model, i.e. the influence from the metal *d*-band position in determining the adsorption strength of molecules on transition-metal surfaces. Figure 5.1 shows the orbitals significantly involved in the bonding process. During adsorption, backdonation from the metal bands to the antibonding 2π LUMO orbital results in a weaker C–O bond. On the other hand, charge removal from the 5σ HOMO level of CO results in a more uniform charge distribution in the

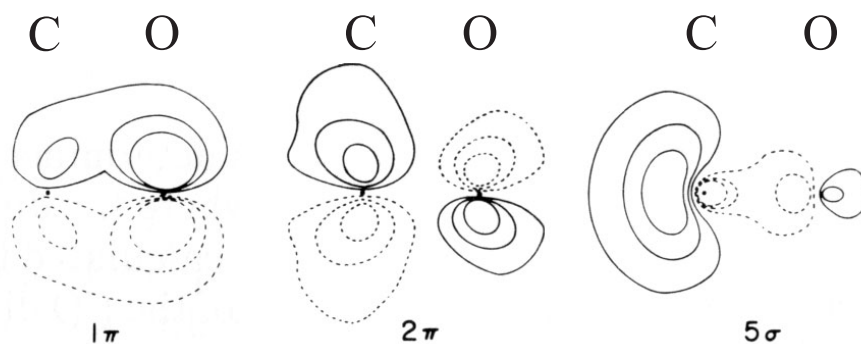


Figure 5.1: Wave function contours of selected CO molecular orbitals. The solid and broken lines indicate contours of opposite sign having absolute values of 0.3, 0.2, and 0.1. Adapted from [91].

1σ level, thus strengthening the C–O bond. This is particularly evident in the gas phase where CO^+ is actually stronger bound than CO. This effect can also be appreciated in Fig. 5.1 where it is evident that the 5σ charge distribution is strongly polarized towards the C end of the molecule and as a result, the 1π charge distribution becomes polarized as well. However, the weakening of the C–O bond through metal- $2\pi^*$ backdonation is stronger than the strengthening of the bond from 5σ charge removal [91].

The following sections are organized such that the order of investigated systems will reflect the degree of their complexity. The simplest case, CO/Pt(111), involves kinetic limitations due to diffusion barriers set up by adsorbate-domain walls. The second case, CO/Pt(110) involves significant substrate transformations but the complex behavior observed in this system can be simply explained based on the d -band model described in Sec. 3.3. The third low-index Pt surface, Pt(100), is briefly discussed in the last section. This surface displays a complicated reconstruction, the so-called Pt(100)-hex-R 0.7° phase consisting of a hexagonal overlayer containing 20–25% more atoms than the underlying (1×1) bulk-terminated structure.

5.2 CO on Pt(111)

5.2.1 Previous UHV and HP studies

Pt(111) has the lowest surface free energy of all Pt surfaces due to its dense hexagonal packing. For this reason Pt(111) is the most abundant facet on supported nano-particles, and high-pressure studies on this surface are therefore of great importance. Studies of CO adsorption on Pt(111) have been performed by many groups over the years.

At 170 K, CO adsorption in UHV leads to a range of structures starting with a $(\sqrt{3} \times \sqrt{3})\text{R}30^\circ$ structure at $\theta=1/3$, which is thought to continuously compress along the high-symmetry $[1\bar{1}0]$ direction [91]. With increasing coverage, a $c(4 \times 2)$ with $\theta=1/2$ is created

and finally a hexagonally close-packed CO overlayer is formed at these low temperatures with a saturation coverage of $\theta \approx 0.68$. Up to $\theta = 1/3$, top-site adsorption is favored but with increasing coverage, bridge sites begin to fill.

For STM studies, it is often found that CO adsorbates are too mobile on metal surfaces to be resolved except at saturation coverages where the adsorbates are “locked” in specific positions by mutual adsorbate-adsorbate interactions. In these situations resolution of the substrate is clearly not possible. A way of circumventing this inherent problem is to compare theoretically calculated STM images of the structure with the experimentally obtained data. Recently, this approach was used by Pedersen *et al.* when comparing theoretically calculated STM images to real STM images of the $c(4 \times 2)$ CO/Pt(111) structure [63]. The structure is easily observed by LEED and STM, and the study by Pedersen *et al.* revealed that the CO molecules were distributed among top and bridge sites on the Pt surface with the top site molecules showing the highest apparent height in the STM. This conclusion seems intuitively reasonable because the adsorbates on top sites are the more protruding ones, but geometrical considerations are not always appropriate when interpreting STM images of adsorbates.

The room-temperature saturation coverage in UHV ($\theta = 0.5$) is rather low considering the van der Waals diameter of CO ($d_{vdw} = 3.2 \text{ \AA}$ [89]).¹ The van der Waals diameter is the typical intermolecular distance in condensed phases of a given molecule, and smaller distances are seldom observed because of the repulsive forces arising from the overlap of orbitals from adjacent molecules. A hexagonal packing of CO with a lattice distance equal to the van der Waals diameter would result in a coverage of approximately 0.75, so there is enough room on the surface for more CO than what is observed in room temperature UHV studies. This suggests that denser phases may be found at higher pressures.

Jensen *et al.* [27] investigated the high-pressure (267–1000 mbar) response of the Pt(111) surface towards CO using STM. A new structure was observed consisting of a hexagonal pattern with a periodicity of $12 \pm 1 \text{ \AA}$. It was suggested that the observed structure was a Moiré pattern due to interference effects between two hexagonal lattices with different lattice constants formed by the CO overlayer and the Pt substrate.² No atomic resolution of CO or Pt was however obtained in [27], for which reason only indirect evidence for the suggested model was presented. The proposed model for the CO layer, in which CO formed a hexagonal lattice oriented parallel to the Pt lattice with a lattice constant of 3.7 \AA , is depicted in Fig. 5.2. Only 1/9 of the CO molecules in the unit cell are positioned in on-top or near-on-top sites, which can be compared with spectroscopic studies using Sum Frequency Generation (SFG). In an earlier SFG study from the same group it was found that the amount of CO adsorbed in on-top sites dramatically decreased when the pressure was raised above 200 mbar [26], compatible with the suggested model in [27]. The SFG study in [26] is, however, contradicted by Freund and co-workers in [40] where similar SFG studies found a $\sim 40\%$ on-top occupancy increase when the CO pressure is raised from low to high pressure. After the presentation of our results a comparison with the two SFG studies will be made.

¹The lattice constant of Pt is 2.78 \AA , for comparison.

²The concept of a Moiré pattern will be explained below.

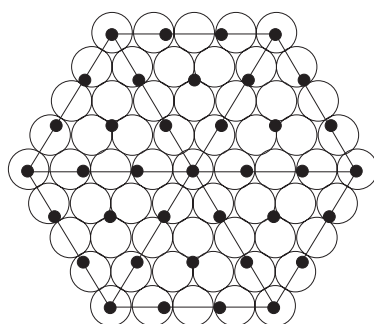


Figure 5.2: Model of a HP CO-overlayer structure on Pt(111) proposed by Somorjai and co-workers in [27]. The large hollow circles represent the Pt atoms and the smaller, dark circles represent the adsorbed CO atoms. The lines connect CO atoms adsorbed in on-top sites, and these are proposed to constitute the Moiré spots.

5.2.2 High-pressure CO/Pt(111)

The gas-inlet system designed to avoid introducing nickel carbonyls into the HP cell has already been described in Sec. 2.2.5. We used standard sample preparation procedures to obtain an atomically clean surface (30 min. 800 V Ar⁺ sputtering, 10 min. annealing at 800 K in 10⁻⁷ mbar O₂ to remove residual carbon impurities followed by 2 min. annealing at 1000 K in UHV). Once the sample was deemed clean by STM, experiments were carried out in the UHV chamber at CO pressures up to 10⁻³ mbar (this relatively high pressure does not affect the chamber base pressure significantly) and in the HP cell up to 1 bar.

After introducing 1 bar of in the HP cell, a hexagonal pattern with approximately the same periodicity as in [27] can be observed immediately with STM. It is however found that two distinct domains of the structure are clearly identified as opposed to the findings in [27], as seen in Fig. 5.3a. In Fig. 5.3b a two-dimensional Fourier transform of the STM image shows the two rotated hexagons more clearly.

The structure found at high pressures of CO can be interpreted as a so-called Moiré pattern: When two hexagonal patterns with slightly different lattice constants are superimposed, an interference pattern resembling the well-known phenomenon of a one-dimensional “beating frequency” between harmonic functions with nearly identical frequencies is observed, as illustrated in Fig. 5.4.

When interpreting the structures formed at high pressures as a Moiré pattern, the relevant parameters are as follows. The angle of the Moiré pattern with respect to the Pt substrate, Ψ_M , the angle of the CO layer with respect to the Pt substrate, θ , the lattice constant in the Moiré pattern, R_M , and the relative lattice constant of CO, $r = d_{CO}/d_{Pt}$.

From measurements on several STM images it is concluded that the pattern found at high pressures of CO is rotated by $\Psi_M = 24 \pm 2^\circ$ with respect to the hexagonal Pt(111) structure. The distance between the spots in the Moiré pattern is found to be $R_M = 11.8 \pm 0.4 \text{ \AA}$ with a smaller uncertainty than in the earlier study. These results fit with a

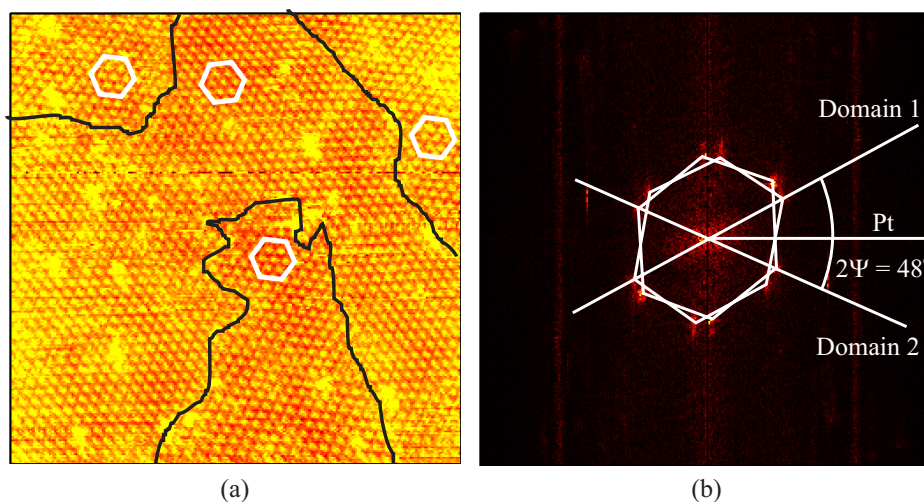


Figure 5.3: (a) Moiré pattern seen in STM images of Pt(111) in a CO pressure of 1 bar ($500 \times 500 \text{ \AA}^2$). Rotational domains are marked by hexagons. The domains in the upper left, upper right and lower center all rotated by the same angle, as marked by the white hexagons. (b) Two-dimensional Fourier transform of the STM image. Two hexagons can be seen each rotated approximately 24° with respect to the close-packed direction of the Pt lattice.

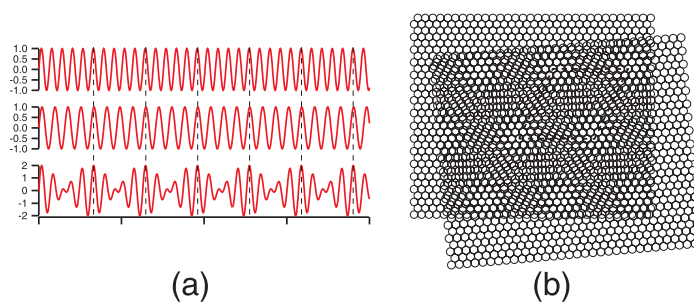


Figure 5.4: The origin of a Moiré pattern. (a) One-dimensional interference (bottom) between two harmonic functions (top and center) with slightly different frequency. The superperiodicity is marked by dashed vertical lines. (b) Moiré pattern formed by interference between two hexagonal lattices. The lattice constants differ by 5% and the lattices are rotated 5° with respect to each other. A unit cell of the Moiré pattern is marked by dashed lines.

$(\sqrt{19} \times \sqrt{19})\text{-R}23.4^\circ$ unit cell and the Moiré pattern hence has the very same periodicity. In the $c(4 \times 2)\text{-}2\text{CO}$ structure found in UHV studies on-top adsorbed CO was seen to have a higher apparent height than molecules adsorbed in bridge sites and we therefore tentatively assume that the protrusions in the Moiré pattern are associated with CO adsorbed in on-top sites.

To unravel the structure of the CO overlayer within the proposed unit cell, i.e. to determine θ and r , *in situ* high-resolution STM images were acquired. Figure 5.5a shows an STM image of the Pt(111) surface at a CO pressure of 960 mbar, and Fig. 5.5b shows a two-dimensional Fourier transform of the STM image. Because of the high resolution in the STM image a large amount of high-order spots from the Moiré pattern is seen in the Fourier transform as a result of anharmonicities in the hexagonal Moiré pattern.³ Specific high-order spots are significantly more intense than other Fourier spots originating from the Moiré pattern. These spots form a hexagon of points all placed at (3×1) -lattice positions, described in units of the fundamental reciprocal lattice vectors of the Moiré pattern. Figure 5.5b shows this hexagon together with the Moiré hexagon.

Based on the Fourier analysis we find a model where the CO molecules form a hexagonally close-packed overlayer rotated $\theta = 9.5^\circ$ with respect to the Pt substrate in the same direction as the 23.4° -rotation of the Moiré pattern as seen in Fig. 5.5b. From Fig. 5.5a it is found that the CO overlayer has a lattice constant of $d_{\text{CO}}=3.4 \text{ \AA}$, i.e. 21% higher than the lattice constant of Pt and hence $r = 1.21$. This results in a CO coverage of $\theta=13/19 \simeq 0.68$, exactly the UHV saturation coverage reported previously [91]. From an interplay between our STM results and DFT calculations performed by B. Hammer we arrive at the lowest-energy structural model shown in Fig. 5.6 with 13 CO molecules per unit cell.

Returning to the SFG studies in [26,40], these results may be compared to our model. In the saturated room-temperature UHV CO structure on Pt(111), the coverage is $\theta = 0.5$ and the ratio of top site to the total number of CO molecules is 1:2. In our model the only on-top molecule is the one assigned to the Moiré spots. However, six other molecules (surrounding the on-top molecule) sit in nearly-on-top sites (marked by red balls in Fig. 5.6). The on-top occupancy is thus almost 7:13 in our case, comparable to the ratio in UHV experiments, but the total coverage is now 13/19 so the on-top occupancy increases by $9/19 \sim 47\%$.

Our experimental results and proposed model are therefore seen to be in good agreement with the SFG experiments presented by Freund and co-workers in [40], where it was found that the SFG intensity of on-top adsorbed CO increased by $\sim 40\%$ when the CO pressure was raised from low to high pressure. Contrary to this, the SFG experiments by Somorjai and co-workers in [26] are not compatible with our findings, since a large decrease in on-top adsorbed CO was found in their study. As it is suggested in [40] the discrepancy between the two SFG studies is probably due to gas absorption of the IR light in the studies presented in [26].

It is interesting to note that in *in situ* electrochemical STM on the present system by Villegas *et al.* [92] a structure identical to the one suggested in our model is actually

³I.e. due to the fact that the atoms are not correctly described by simple harmonic functions. At modest resolution the high-order spots are, however, not seen because these finer details within the unit cell are averaged out by noise and fluctuations in the tip condition.

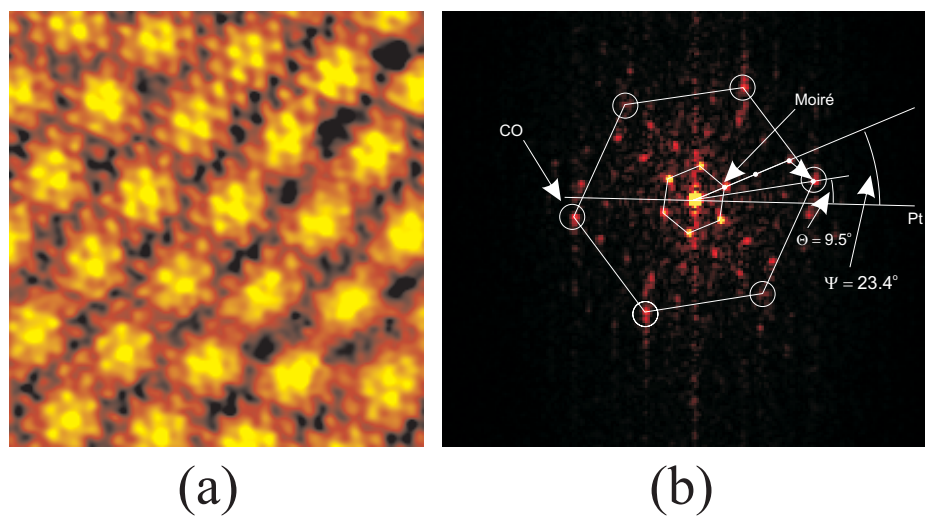


Figure 5.5: (a) High-resolution STM image ($55 \times 51 \text{ \AA}^2$) of the CO overlayer obtained at 1 bar CO. Fourier filtering has been employed to bring out the atomic details. (b) Fourier transform of the STM image. The brightest higher order spots of the Moiré pattern are assigned to the CO layer (marked by white circles). The angle between the CO layer and the Pt substrate is indicated on the figure.

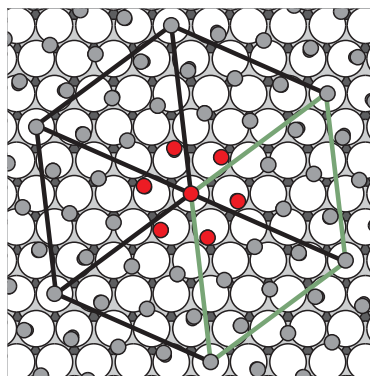


Figure 5.6: The $(\sqrt{19} \times \sqrt{19})R23.4^\circ$ -13CO structure. One CO molecule in the unit cell has been fixed in the on-top position. If alternatively the CO molecule is fixed to the bridge or fcc position the energy is according to DFT calculations by B. Hammer raised by about 0.4 eV per unit cell (3-layer Pt slab). The unit cell of the pattern is indicated with the green solid line. Red balls represent CO molecules adsorbed in nearly on-top sites (See text).

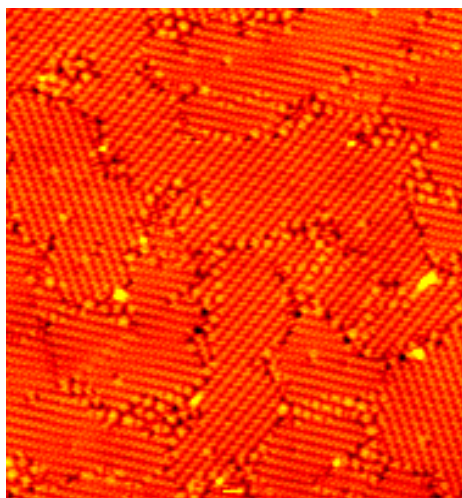


Figure 5.7: Striped domain structure formed from UHV CO adsorption on Pt(111) at 100 K ($348 \times 363 \text{ \AA}^2$).

found at a range of sample voltages, which effectively corresponds to different pressures of CO. It is intriguing that similarities at the atomic level exist between high gas pressures and effective high pressures in electrochemistry. However, in the voltage range, which according to Villegas *et al.* would be comparable to atmospheric pressure of CO, a (2×2) -3CO structure, is found. The (2×2) -3CO structure has a coverage of $\theta = 0.75$, i.e. even more dense than our HP structure and comparable to the van der Waals packing of CO molecules as mentioned above. It would thus be very interesting to image the CO/Pt(111) system at even higher pressures to investigate whether or not the (2×2) -3CO structure would also show up in the gas experiments, but unfortunately we are limited to 1 bar because of the window in the high-pressure cell. The dense (2×2) -3CO structure is in fact postulated to be seen on the similar Rh(111) surface at high pressures of CO [93].

5.2.3 STM observations at low temperature

To investigate the CO/Pt(111) structures at the low-pressure side of the pressure gap, we exposed the Pt(111) surface to CO at UHV pressures and low temperature. Figure 5.7 shows the striped domain structure formed at 100 K. We have not investigated the atomic structure systematically but the structure certainly bears no resemblance to the HP Moiré structure described above. This is consistent with earlier LEED and EELS studies where at 100 K the adsorbate was found to exhibit an island structure [94]. In the same study, annealing to 260 K was found to induce long-range order. At 100 K, the CO molecules are clearly not able to equilibrate and the structure formed is a metastable one, which should not be compared to the HP structure from above.

Indeed, CO exposure at slightly higher temperatures, here 170 K, formed the exact

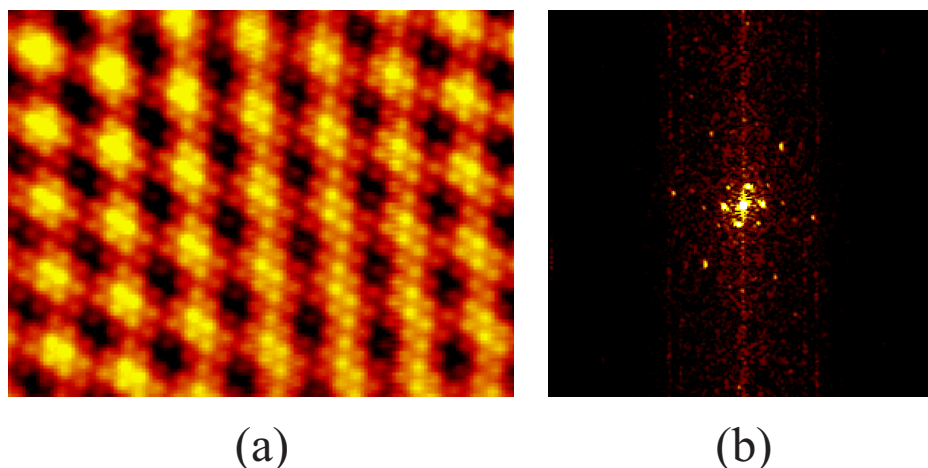


Figure 5.8: UHV CO adsorption on Pt(111) at 170 K. (a) Atomically resolved Moiré structure at 170 K. Fourier filtering has been employed to bring out the atomic details. (b) The corresponding 2D Fourier transform. Peaks corresponding to both the Moiré and adsorbate periodicities are clearly distinguished. Compare to Fig. 5.5b.

same ($\sqrt{19} \times \sqrt{19}$)R23.4°-13CO structure seen at high pressures and room temperature, see Fig. 5.8. The temperature is now high enough for CO to settle into its equilibrium structure. Ertl *et al.* were the first to detect this structure with $\theta=13/19$ [95] by LEED but a correct real-space model was not deduced at that time.

5.2.4 Conclusion

Summarizing, we have achieved atomic-scale evidence for a model describing the structure of CO adsorbed on Pt(111) at a pressure of approximately 1 bar. We have found that CO forms a hexagonally close-packed overlayer with a lattice constant of 3.4 Å. The CO layer is rotated with respect to the Pt substrate with an angle of 9.5°, compatible with the distances and angles found in the Moiré pattern. The coverage of CO in the proposed model amounts to $\theta=13/19 \sim 0.68$, i.e. significantly higher than what was suggested by Somorjai and co-workers, yet lower than a “van der Waals packing” of CO where the coverage would be $\theta_{vdW}=0.75$. In UHV, care must be taken to overcome adsorbate diffusion barrier set up by adsorbate domain walls. A metastable domain structure is formed at 100 K but CO adsorption at 170 K results in the exact same structure as in the high-pressure case. With respect to the pressure gap we thus conclude that raising the pressure is equivalent to lowering the temperature as long as the thermodynamical equilibrium structure remains kinetically accessible.

5.3 CO on Pt(110)

Crystalline materials usually expose planar low-Miller-index facets at low temperatures due to the high energy required to form structural defects like steps and kinks. On the order of 0.25 eV is required to break nearest-neighbor (nn) Pt bonds so very high temperatures (>1080 K) are needed for a sizable fraction of Pt-Pt bonds to be broken spontaneously [96]. However, with the introduction of CO adsorbates, surface roughening proceeds readily even at room temperature. Here we report on the atomic-scale response of the Pt(110) surface to CO adsorption at temperatures in the 300–400 K range and pressures ranging from 10^{-9} –1000 mbar. Depending on temperature and CO pressure, the surface structure changes dramatically. In particular, we observe an extremely rough equilibrium structure at intermediate coverages, which transforms into a well-ordered saturation structure under high CO pressure. We show here that by exposing a Pt(110) surface to CO, the energy required to break Pt–Pt nearest-neighbor bonds in the surface approaches zero and consequently the equilibrium structure of the CO-covered surface is microscopically rough with more than 50% of the atoms associated with steps. The seemingly complex behavior of the CO/Pt(110) system can be explained by a very simple model at all pressures. Furthermore, we shall see that the structure observed at high pressures could have been predicted from UHV data only.

CO adsorption on Pt(110) has been a favorite prototype system for adsorbate-induced structural transformations in the modern surface science era and has been investigated extensively with almost any conceivable theoretical [66, 97–100] and experimental UHV technique: LEED [89, 101–107], ultraviolet photoelectron spectroscopy (UPS) [89, 108], TDS [89, 102–104, 106], high-resolution electron energy loss spectroscopy (HREELS) [89, 109–111], Angle-Resolved UPS (ARUPS) [90, 109, 112], Rutherford backscattering spectroscopy (RBS) [104, 113], nuclear microanalysis (NMA) [104], RAIRS [106, 110, 114, 115], X-ray photoelectron spectroscopy (XPS) [105], work function measurements [102, 105, 107], STM [30, 116, 117], inverse photoelectron spectroscopy (PES) [118], reflectron high-energy electron diffraction (RHEED) [119], SFG [111], microcalorimetry [120], as well as high-pressure (HP) STM [25].

5.3.1 Experimental results

The Pt(110) surface exhibits the well-known (1×2) missing-row reconstruction in its clean state [121, 122], see Fig. 5.9. Gas adsorption alters the delicate energy balance between a bulk truncation and the missing-row reconstruction—the total energy per atom of the (1×2) structure is only 0.27 meV/atom lower than in the (1×1) structure [123]. Adsorption of CO induces a lifting of the (1×2) reconstruction [30]. The $(1 \times 2) \rightarrow (1 \times 1)$ transition is readily observable at the atomic scale with STM through the local motion of the Pt atoms. Note that at all coverages below full monolayer coverage ($\theta = 1$), the CO molecules are not detected by STM at room temperature. This has been attributed to the CO molecules' rapid diffusion and/or frustrated motion [124], i.e. the ability of the on-top-adsorbed CO molecule to vibrate while still staying bound to a Pt atom. These kinds of motion require very little energy and thus proceed rapidly even compared to the fairly high scanning speed obtainable with our STMs.

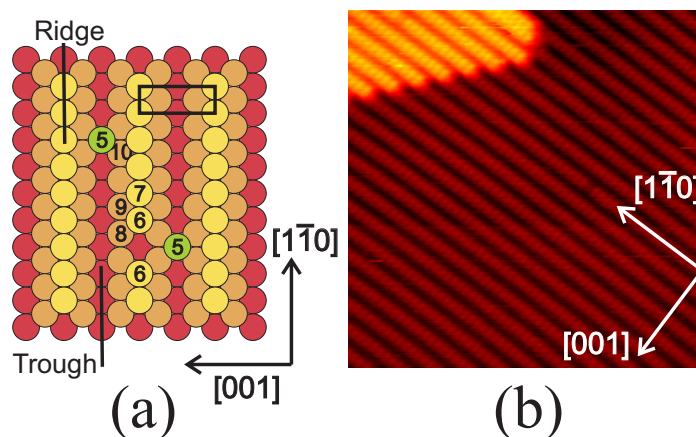


Figure 5.9: Missing-row reconstructed Pt(110) surface and the effect of CO adsorption. (a) Model of the missing-row reconstructed Pt(110)-(1 \times 2) surface. Pt coordination numbers for the perfect surface as well as for various defects are also shown. A (1 \times 2) unit cell is indicated. (b) STM image showing the clean Pt(110)-(1 \times 2) structure. A monatomic step is seen in the upper-left corner (141 \times 155 \AA^2).

CO exposure at room temperature

Figure 5.10 shows a number of stills from an STM movie, i.e. a series of sequential STM images [125], recorded at room temperature, which captures several steps in the CO-induced lifting of the (1 \times 2) reconstruction. We recognize the creation of a “hole” involving 4 atoms in the close-packed rows. Once the first Pt atom has moved from ridge to trough, the remaining steps in the evolution of a hole proceed readily.

A larger-scale STM movie (Fig. 5.11) shows the homogenous nucleation and growth of the moieties of Fig. 5.10. All holes cease growing when 4–6 atoms have been displaced. Further enlargement of a given hole is impeded by attractive interactions in the [001] direction in that Pt atoms (or CO/Pt complexes) are trapped between next-nearest-neighbor rows. Notice that only mass transport at a very local scale is sufficient to completely remove the (1 \times 2) periodicity.

A high-resolution STM image of a partially lifted reconstruction is seen in Fig. 5.12a. We clearly discern the 4–6-membered holes and recognize the 1:1 correspondence between displaced Pt atoms and resulting ridge vacancies. The distinct character of every hole is lost when the holes start coalescing. The resulting structure of room-temperature CO exposure is seen in Fig. 5.12b. Notice the emergence of second-layer Pt atoms, which become accessible to CO adsorption only after the reconstruction is lifted. The end result is a very rough structure with no kind of ordering except a retained preference for Pt atoms to reside in four-fold hollow sites.

We have studied the evolution of the CO-induced lifting of the reconstruction by varying the CO background pressure and counting the number of holes as a function of

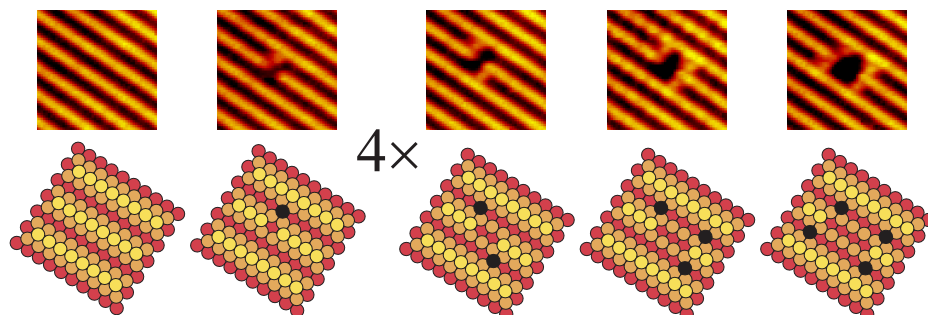


Figure 5.10: Atomistic mechanism for the CO-induced lifting on Pt(110). Time between stills: 7.8 s. “4×” simply indicates that this configuration is seen on 4 consecutive images of which only one is shown.

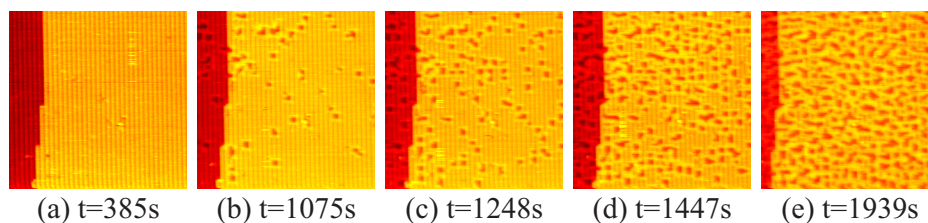


Figure 5.11: Larger-scale still from an STM movie showing homogeneous nucleation and growth of 4–6 membered holes. Size $300 \times 300 \text{ \AA}^2$. $P = 2 \cdot 10^{-9}$ mbar. Time relative to the introduction of CO is indicated below each still. The entire movie can be viewed at our web site: <http://www.phys.au.dk/camp/movies/co01.mpg>.

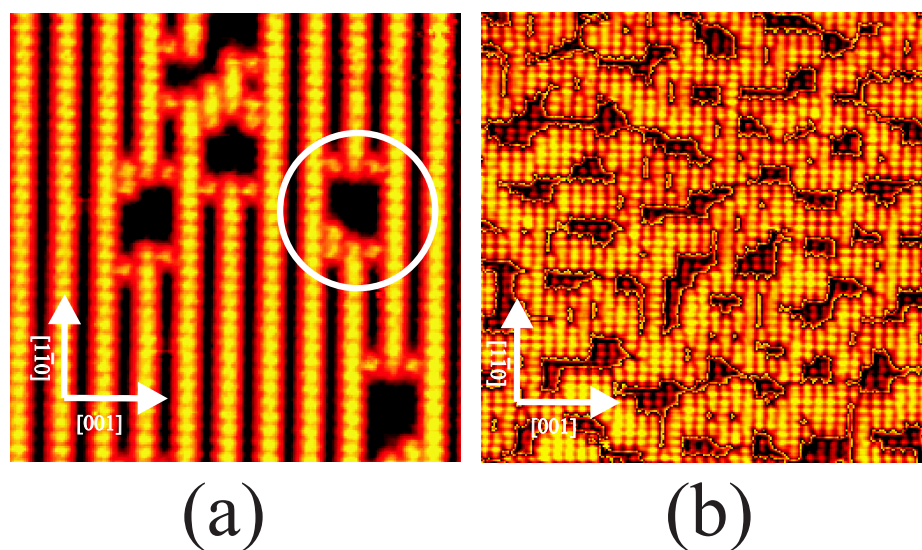


Figure 5.12: Appearance of (a) a partially CO-lifted reconstruction ($92 \times 102 \text{ \AA}^2$) and (b) completely CO-lifted reconstruction at room temperature ($138 \times 154 \text{ \AA}^2$). In (a), the circle marks a 5-membered hole to be considering in the Discussion. In (b), the color scale has been repeated to show the emerging atoms of the second layer. As expected, these are shifted by half a [001] spacing, cf. Fig. 5.9.

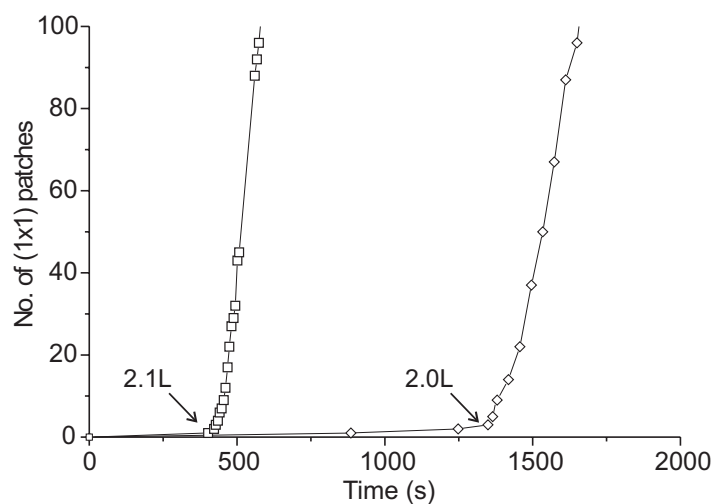


Figure 5.13: Number of holes as a function of time for different CO background pressures. Number of holes as a function of time. \square : $P_{\text{CO}} = 6.7 \times 10^{-9}$ mbar. \diamond : $P_{\text{CO}} = 2.0 \times 10^{-9}$ mbar. The count was done on $275 \times 307 \text{ \AA}^2$ images.

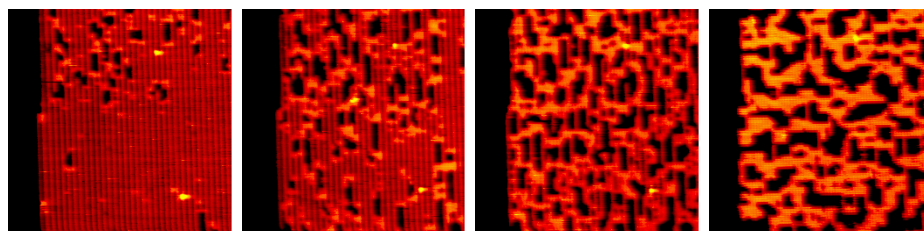


Figure 5.14: STM movie of CO/Pt(110) recorded at 373 K demonstrating relaxation towards thermodynamic equilibrium ($300 \times 300 \text{ \AA}^2$), $P = 2 \cdot 10^{-9}$ mbar. The entire movie can be viewed at our web site: <http://www.phys.au.dk/camp/movies/co02.mpg>.

time. The results are shown in Fig. 5.13. We see that a critical exposure of about 2 L is needed for hole-creation onset, independent of the CO pressure used. The onset of the CO-induced lifting of the (1×2) reconstruction thus starts when a specific critical coverage, which may well be temperature dependent, is reached.

The question now arises whether the observed rough structure presents the thermodynamical equilibrium structure. This can be investigated either by simply keeping the sample temperature at an elevated temperature during CO exposure or by flash-annealing the sample after room-temperature exposure, thereby allowing the Pt atoms to equilibrate.

CO exposure at elevated temperatures

To resolve whether the thermodynamic equilibrium structure is reached, we investigated the structural response of the Pt substrate towards CO adsorption at elevated temperatures, here 373 K. Figure 5.14 shows the evolution, which proceeds in two regimes: First, kinetic limitations dominate through Pt translations akin to those observed at room temperature. Holes form in the close-packed rows, i.e. atoms are displaced from ridges to trough, but the size of the holes is no longer limited to 4–6 atoms since higher thermal activation enables more far-reaching Pt displacements. We note in passing that at 373 K, hole creation commences at a lower exposure (~ 1 L) than at room temperature, indicative of stronger thermal activation.

The creation of the rough structure is followed by relaxation towards equilibrium. Short close-packed Pt strings line up *perpendicular* to the close-packed rows, see last still in Fig. 5.14. The same kind of equilibrium structure can be produced by flash-annealing the sample to 400 K in UHV after room-temperature exposure, as seen in Fig. 5.15. Again a channel-like structure lined up in the [001] direction is formed. In both cases discussed above, desorption will occur, as the lower of the two CO desorption peaks lies at ~ 375 K [89]. The CO coverage will thus be below saturation coverage ($\theta=1$). A large number of steps is observed — in fact about 50% of the Pt surface atoms have fewer than seven Pt nearest neighbors; or, equivalently, 50% of the surface atoms are associated with steps in the close-packed direction.

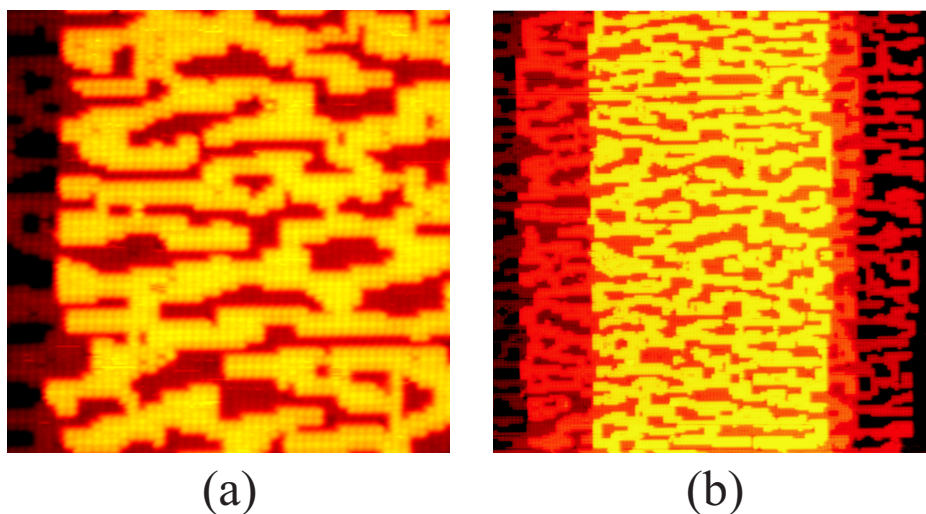


Figure 5.15: The effect of flash-annealing a room-temperature CO-exposed Pt(110) surface to 400 K. (a) $200 \times 200 \text{ \AA}^2$. (a) $500 \times 500 \text{ \AA}^2$.

(2×1) - $p2mg$ -2CO structure

It is also possible to form an equilibrated CO saturation-coverage structure in UHV. Cooling down from 600 K to room temperature in 10^{-7} mbar CO creates a (2×1) - $p2mg$ -2CO structure adsorbed on an underlying (1×1) substrate also found for several other transition-metal (110) terminations, e.g. Ni [124]. In this case, the CO overlayer is so densely packed that the molecules' frustrated motion is impeded and the CO molecules, opposite to the low-coverage case, themselves are imaged as also discussed in the beginning of this section. STM images show a characteristic *zigzag* CO structure covering the entire surface, see Figs. 5.16a-c and Fig. 5.16d for a simple ball model.

The *zigzag* CO structure is only observed at coverages very close to or equal to unity. Slightly below monolayer coverage, the steric hindrance from adjacent CO molecules is insufficient to lock the CO molecules into place. Instead elongated (in the $[1\bar{1}0]$ direction) signatures of vibrating molecules are observed since the molecules' frustrated motion is no longer impeded. In the high-resolution image in Fig. 5.16a, we notice the absence of at least two molecules in the CO overlayer. Molecules adjacent to such imperfections appear larger than other molecules. A missing CO molecule could be the result of an imperfect underlying Pt (1×1) substrate, i.e. a missing substrate atom. A similar effect is observed close to step edges, see Fig. 5.16c. Molecules adsorbed at step edges can be imagined to "lean out" from the step edge and create more room for nearby molecules.

From the results presented above, one realizes that a substrate temperature of 373 K is high enough to sufficiently invigorate substrate Pt atoms to approach their equilibrium structure at a given coverage. Intermediate coverage ($0 < \theta < 1$) structures are easily

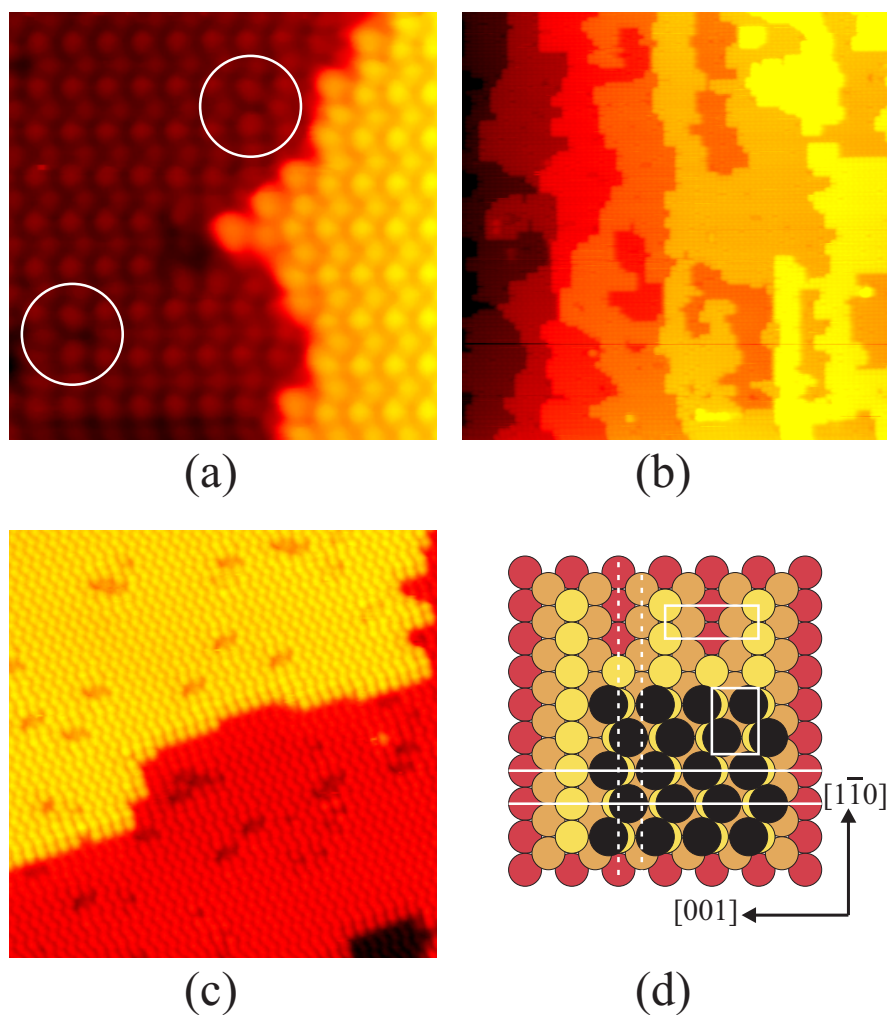


Figure 5.16: Imaging of CO molecules in the (2×1) - $p2mg$ -2CO structure on Pt(110). (a) “Missing” CO molecules in the otherwise perfectly developed structure are indicated by white circles. $50 \times 50 \text{ \AA}^2$. (b) Larger-scale image showing the compaction of Pt atoms into (1×1) areas. $300 \times 300 \text{ \AA}^2$. (c) Relaxation at step edges in the (2×1) - $p2mg$ -2CO structure. $141 \times 147 \text{ \AA}^2$. (d) Ball model of the structure. The substrate atoms diameter (2.78 \AA) and CO molecule van-der-Waals diameter (3.2 \AA) are shown in correct relative proportions. Unit cells of bare substrate and (2×1) overlayer are indicated. The glide line and mirror symmetries belonging to the $p2mg$ space group are indicated by dashed and full lines, respectively.

accessible but a special treatment had to be implemented to produce the full coverage structure in UHV.

Elevated-temperature high-pressure CO exposure

Another question then arises as to the effect of even higher CO pressure than the maximum of 10^{-7} mbar employed above. To this end, our novel HP-STM design allows us to follow the changes in the atomic-level surface morphology at progressively higher pressures up to 1 bar, as discussed in Chap. 2. We are thus again able to bridge the pressure gap at the atomic scale

A high-pressure experiment is always conducted at 1 bar total pressure composed of a given CO partial pressure back-filled with Ar. The CO partial pressure can thus not be adjusted whilst performing STM measurements so only batch experiments are possible. To ensure that only thermodynamic-equilibrium structures are created, all HP experiments reported in the following were carried out at 373 K. This was accomplished by heating the entire HP cell externally.

Even though CO desorption takes place at a sample temperature of 373 K, we expect to reach progressively higher adsorbate coverages when increasing the CO background pressure. Raising the CO pressure, and thus the incoming molecular flux, puts the adsorption system in surface-gas phase equilibrium where a free site created by a desorbed molecule is quickly reoccupied by an incoming molecule. This is where high-pressure experiments differ from UHV experiments at low temperature. At low temperature, no replenishment from the gas phase is needed to maintain a high adsorbate coverage.

Figure 5.17 shows the resulting structures at a range of CO partial pressures. We see how at low pressures the displaced Pt atoms order into the same channel-like structure ordered along the [001] direction described above. The [001] steps are characterized by a low kink density. Higher CO pressures, however, result in kink formation, and consequently step edges become “rounder”, see Fig. 5.17d. The transition from kink-free step edges to rounder edges is found to take place at a CO partial pressure of $\sim 10^{-3}$ mbar where also the first hint of the high-coverage (2×1) - $p2mg$ zigzag structure is observed (not shown). At a CO pressure of 1 bar the channel-like structure has been replaced by islands elongated in the $[1\bar{1}0]$ direction. A zoom-in in (Fig. 5.17f) reveals the (2×1) - $p2mg$ zigzag structure also observed in UHV on both first and second-layer areas. As will be discussed further below, it thus appears that the CO structure observed at 373 K and high pressures from 10^{-3} mbar to 1 bar is indeed identical to the one observed at low pressure.

5.3.2 Discussion

To disentangle the multitude of details presented above, the following discussion is divided into two natural parts treating low and high-coverage structures. The low-coverage discussion furthermore concerns a comparison of the rough structure observed at intermediate coverages to the structure obtained in Monte Carlo simulations.

The observed structures and accompanying transformations depend on CO coverage in a fairly complex way. However, as will be shown below, a simple model in which

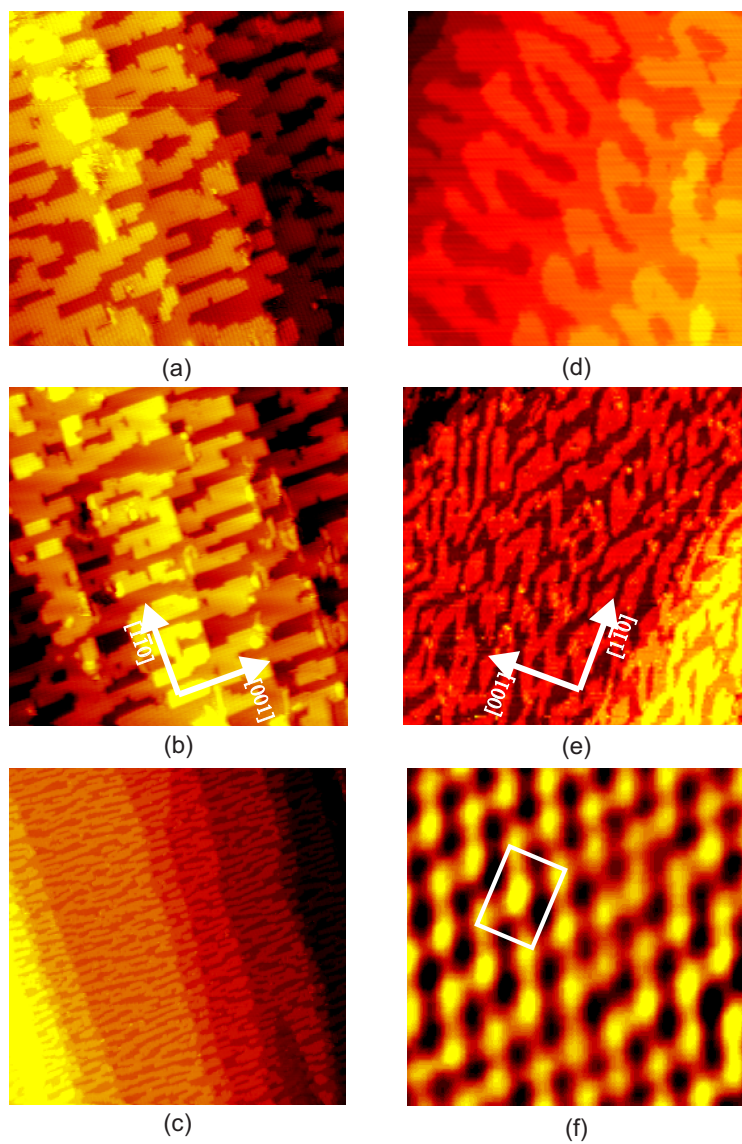


Figure 5.17: STM images of Pt(110) at 373 K and at different CO pressures. Left-column images were obtained in UHV, right-column images under high pressures. (a) 10^{-7} mbar, ($300 \times 300 \text{ \AA}^2$), (b) 10^{-6} mbar, ($300 \times 300 \text{ \AA}^2$), (c) 10^{-5} mbar, ($1000 \times 1000 \text{ \AA}^2$), (d) 10^{-2} mbar, ($700 \times 700 \text{ \AA}^2$), (e) 1000 mbar ($900 \times 900 \text{ \AA}^2$) and (f) 1000 mbar ($28 \times 28 \text{ \AA}^2$).

the CO binding energy depends in a linear fashion on the coordination number of the Pt atom to which it binds, is able to account for all the STM results.

Low-coverage behavior

We start by scrutinizing the creation of the CO-induced holes by going through a simple bond counting process. We consider, as an example, the formation of a five-membered hole where 7 Pt atoms experience a change in the number of nearest neighbors (nn), cf. Figs. 5.9b and the encircled hole in 5.12a. Before rupture of any nn bond, all 7 atoms on the (1×2) terrace have 7 nn and after the creation of a hole, 3 atoms have 5 nn and 4 atoms have 6 nn. The end result of hole formation is thus to lower the average coordination number of the affected Pt atoms.

The van-der-Waals diameter of CO is ~ 3.2 Å, significantly larger than the Pt nn distance of 2.78 Å, so $\theta=1/4$ (one CO per two top-layer Pt atoms) is the highest coverage possible when imposing the criterion of preferred on-top adsorption in the top Pt layer. This is in accord with previous studies in that at room temperature lifting is found to commence when $\theta \approx 0.2$. The concept of a critical coverage is also found in Fig. 5.13 where we measure a critical *exposure* of ~ 2 L since the CO molecules elude detection at sub-monolayer coverages.

For CO adsorption to continue, CO/Pt complexes have to “squeeze out” from the ridges to accommodate more CO and indeed previous studies show that the lifting process is completed — no (1×2) areas are detected — when $\theta \approx 1/2$. These steps only require displacements ranging a few lattice spacings and are readily observed at room temperature as demonstrated in Sec. 5.3.1. As we have seen above, however, at room temperature the resulting structure is metastable and higher temperatures are needed to form the equilibrium structure.

In the following we focus primarily on the rough surface structure at intermediate CO coverages. We will show that it indeed represents an equilibrium structure of the system, where CO adsorption has lowered the step formation energy to a value close to zero. Steps and other defects on the surface are characterized by Pt atoms with a low Pt coordination number, cf. Fig. 5.18a. Our collaborators from Nørskov’s group have studied the adsorption energy of CO on Pt(110) as a function of the Pt coordination number using density functional theory (DFT) [50,56,126]. The calculations are performed with electronic exchange and correlation described within the generalized gradient approximation (GGA, PW91) [127]. The surface is modelled by slabs of nine Pt(110) layers, where the top three layers and the CO coordinates are fully relaxed. The numerical setup is identical to the one described in Ref. [128].

The driving force behind the lifting of the (1×2) reconstruction can be explained within the *d*-band model presented in Sec. 3.3. Fig. 5.18a shows in quantitative terms that CO molecules bond strongly to Pt atoms with a low Pt coordination number, while Pt atoms with a high coordination number bind CO more weakly. On the unperturbed Pt(110)- (1×2) surface, CO prefers to bond to Pt atoms at ridges, since these Pt atoms have a coordination number of 7 in contrast to the Pt atoms on the sides of the troughs with a coordination number of 9. A Pt atom at a step perpendicular to the close-packed direction or a single Pt atom in the troughs have coordination numbers 6 and 5, re-

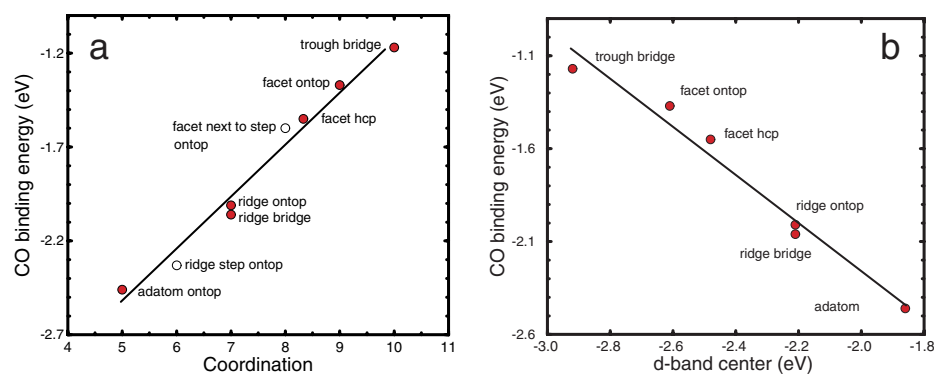


Figure 5.18: (a) Calculated CO chemisorption energies at different positions on the Pt(110) surface versus the mean coordination number of the nearest Pt atoms. With open symbols we include data for CO adsorption on a Pt dimer on Pt(110) (coordination number 6) from Feibelman [129] and on a Pt(100) surface (coordination number 8) from Hammer *et al.* [70], see Table 5.1 for details. (b) Data for Pt(110) plotted as a function of the average energy of the d -states to which the CO interacts. As the metal coordination number is reduced the local d -band narrows and moves up, leading to stronger bonding.

spectively (see Fig. 5.9), and they therefore bind CO even stronger than Pt atoms at the ridges. The important point in the present context is that the extra bonding of CO to the low-coordinated Pt atoms is of the same order of magnitude as the energy required to form the defect with a low coordinated Pt atom. The difference in adsorption energy on e.g. an adatom (coordination number 5) and on the ridge (coordination number 7) is found to be 0.45 eV. This should be compared to the energy of forming an adatom, which we calculate to be essentially the same, 0.45 eV.

The accuracy of the DFT calculations only allows us to say that the effective defect formation energy in the presence of CO is close to zero. Nonetheless, we note that even a slightly positive step formation energy will lead to a surface with many steps at finite temperatures due to the higher entropy of the defected surface. Based on the DFT calculations it therefore seems very likely that CO adsorption be able to break up the Pt(110)-(1×2) surface completely at room temperature as observed experimentally.

To substantiate that the experimentally observed rough structure at $\theta_{\text{CO}} < 1$ is the actual equilibrium structure, we compare it in more detail to the structure expected from DFT calculations. Our collaborators in J. Nørskov's group have performed Monte Carlo simulations of the equilibrium structure using interaction values deduced from DFT calculations as simulation parameters. In the simulations the total energy of the system is written as

$$E = \frac{1}{2} \sum_{i,j} V_{ij} \quad (5.3)$$

where i and j runs over all Pt atoms in the first two layers and over the CO molecules.

Parameter	Value (eV)	Remarks
$V_{\text{CO/Pt}}(\text{coord}=5)$	-2.46	a
$V_{\text{CO/Pt}}(\text{coord}=6)$	-2.33	b
$V_{\text{CO/Pt}}(\text{coord}=7)$	-2.01	a
$V_{\text{CO/Pt}}(\text{coord}=8)$	-1.60	c
$V_{\text{CO/Pt}}(\text{coord}=9)$	-1.37	c
$V_{\text{Pt,Pt}}(\text{nn})$	-0.45	a
$V_{\text{CO,CO}}(\text{nn})$	0.06	d
$V_{\text{Pt,Pt}}(\text{nnn})$	0.10	e

Table 5.1: Parameters used in MC simulations. (nn): nearest neighbors. (nnn): next-nearest neighbors. a: This work. b: The energy difference $V_{\text{CO/Pt}}(\text{coord}=6) - V_{\text{CO/Pt}}(\text{coord}=5) = E_{\text{dis}}(\text{“empty” dimer}) - E_{\text{dis}}(\text{dimer with 1 CO ontop})$ is estimated from calculations by Feibelman [129]. c: The energy difference $V_{\text{CO/Pt}}(\text{coord}=7) - V_{\text{CO/Pt}}(\text{coord}=8,9)$ is estimated from calculations on Pt(111) [70]. d: Estimated from calculations by Feibelman [129]. e: Estimated from calculations on Au(110) [130].

CO can adsorb on all Pt atoms in the two outermost layers. All interaction energies are deduced from DFT calculations as shown in Table 5.1. The reconstruction energy of the clean Pt(110) surface needed to obtain the nnn interactions between Pt has not been calculated. Instead, it was estimated from calculations on Au(110) [130] by scaling the reconstruction energy of Au(110) with the surface energies of Pt(110) and Au(110) [131]. This number turned out to be important only for simulated structures found at $\theta_{\text{CO}} \lesssim 0.2$. 100×100 surface unit cells are simulated starting from the perfect missing-row (1×2) reconstructed surface. CO is then adsorbed to a specific coverage and equilibrated at 300 K by running 10^4 trial moves per site using the Metropolis algorithm described in Chap. 3. Snapshots at three coverages are shown below the corresponding STM images in Fig. 5.19. The absolute experimental coverage after annealing was determined as the ratio between the integrated areas of thermal desorption spectra from the annealed structure and the full coverage (2×1)-p2mg phase and was determined to be $\theta_{\text{CO}} = 0.8 \pm 0.1$. Clearly a good qualitative agreement is found.

From the simulations, the equilibrium number of defects/steps as a function of CO coverage can be calculated, as presented in Fig. 5.20a (A step is defined as a Pt atom with a coordination number lower than 7). The number of steps shows a maximum of 90% around a CO coverage of 0.7. We have not investigated this extreme coverage experimentally but at a CO coverage of 0.8 the MC simulation shows about 60% steps, in good agreement with the experimental value. At a more detailed level, we can compare the experimental and theoretical values for the presence of Pt rows of different lengths at the coverage 0.8, Fig. 5.20b. The experimental results show fewer rows with 2 Pt atoms in the $[1\bar{1}0]$ than does the simulation, but given the fact that no fitting of the parameters has been made and the fact that the experimental determination of the CO coverage is somewhat uncertain, the agreement is quite satisfactory. We therefore suggest that the rough surface at a CO coverage around 0.8 is a direct observation of *adsorption-induced roughening*.

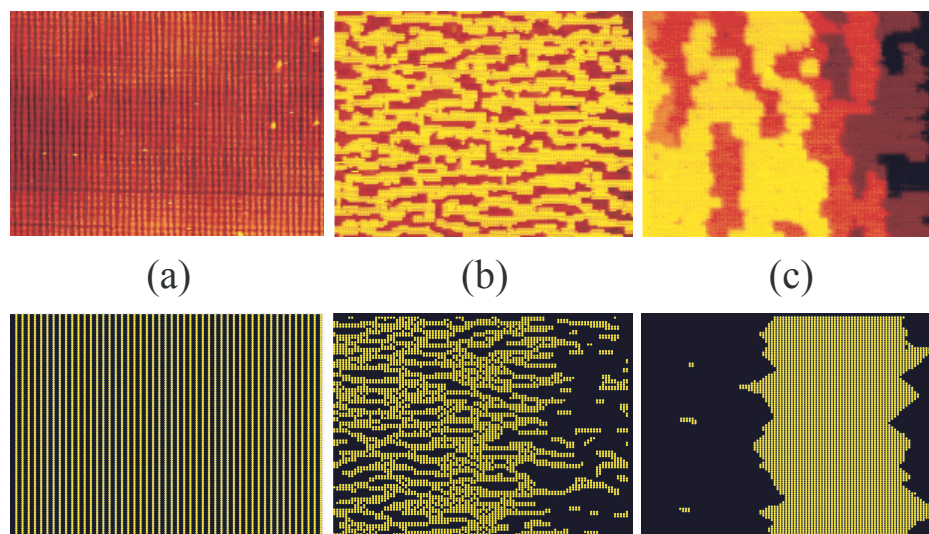


Figure 5.19: STM images (top) of Pt(110) at different CO coverages and corresponding snapshots from a Monte Carlo simulation (bottom) of the surface structure at 300 K and at the three two coverages ($400 \times 280 \text{ \AA}^2$). (a) $\theta=0$, (b) $\theta \simeq 0.8$, and (c) $\theta=1$, the latter imaged in a 10^{-7} mbar CO background. The images are taken at 300 K as explained in the text. All MC parameters are deduced from DFT calculations.

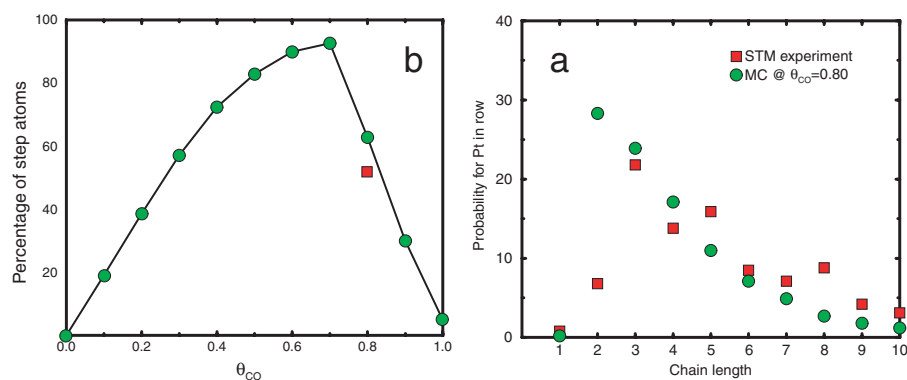


Figure 5.20: (a) Step density calculated at 300 K based on DFT parameters of Table 5.1 shown as a function of the CO coverage. The experimental observation at a coverage of 0.8 is included as a square. (b) A comparison of measured and calculated probabilities of finding Pt rows of different lengths.

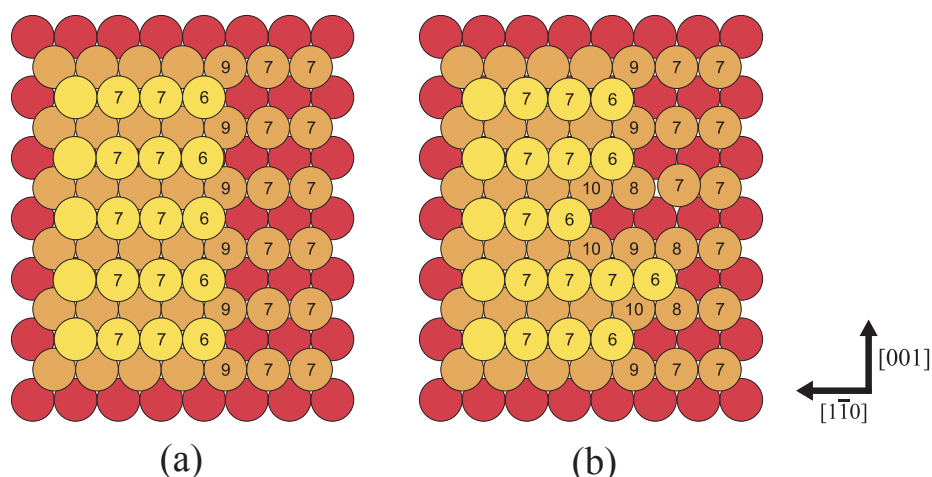


Figure 5.21: Ball model of the kink formation process on a Pt(110) surface showing the coordination number of the Pt atoms involved. (a) Kink-free [001] step edge. When the CO coverage is less than unity, CO is only adsorbed on the low-coordinated sites (<8 nearest neighbors), and the kink-free configuration is therefore the energetically favored configuration. (b) Kink formation. When the CO coverage is close to unity, the energy difference between the two configurations is close to zero and the higher entropy of the kinked step edge is therefore favored at finite temperatures.

High-coverage behavior

The considerations above only included coordination number changes in top-layer Pt atoms. When the Pt (1×2) reconstruction is lifted, however, the next Pt layer is made available for CO adsorption. At most half of the second layer is exposed because the top layer Pt atoms effectively constitute half a monolayer when compacted into the (1×1) phase. The exposed part of the second layer is a full (1×1) layer with a Pt coordination number of 7; higher coordination numbers (8–10) are found at step edges, as seen in Figs. 5.9a and 5.21. Even while the lifting process occurs, adsorption must take place on both first and second-layer atoms, initially at coordination number 7 sites. At ever higher coverage, adsorption is forced to take place at less energetically favored 8–10-coordinated sites, see Figs. 5.9a and 5.21. Here we recognize the driving force behind the line-up of short, close-packed Pt rows along the [001] direction observed at intermediate coverages (Fig. 5.15 of Sec. 5.3.1): The lined-up structure does not contain a lower number of step atoms (coordination number 5–6 in the top layer) than would a structure with no kind of ordering of the short close-packed rows. It rather minimizes the average coordination number of occupied Pt sites in the second layer.

For coverages close to saturation, the energy gained in the kink-free channel structure vanishes due to adsorption on second-layer, high-coordinated Pt atoms. Entropic

effects (higher disorder) are then manifested as kinked or “rounded” step edges, as was observed at a pressure of 10^{-2} mbar in Fig. 5.17d. The formation of a kink is illustrated in Fig. 5.21 where we recognize the higher average coordination number of the kinked structure. At even higher pressures, channels coalesce to form extended (1×1) substrate areas with the characteristic *zigzag* (2×1) - $p2mg$ -2CO pattern seen in Figs. 5.16 and 5.17f.

Our results shed new light on a previous high-pressure STM study of the CO/Pt(110) system. [25] This being a pioneer experiment in the area of high-pressure STM, the design did not enable atomic resolution. Furthermore, McIntyre *et al.* made use of a transfer cell between crystal cleaning and HP imaging which raised the background pressure during transfer to 10^{-5} mbar. After heating at 425 K for 5 h in 1 bar CO, McIntyre *et al.* observed large flat terraces displaying no missing-row reconstructions separated by multiple-height steps and groups of steps with a corrugation amplitude of 42 Å. Due to the lack of atomic resolution, no further details could be extracted of the atomic structure on the flat terraces.

We also observe extended terraces at high pressures and the mechanism for their creation was presented above. Atomically-resolved images of the (2×1) - $p2mg$ -2CO structure created on the flat terraces allow us to confidently conclude that the pressure gap has indeed been bridged for this system. Contrary to the findings of McIntyre *et al.* we do, however, not observe any large-scale changes, i.e. the well-known mesoscopic “corrugated-iron” structure [132, 133] is not modified even after over-night exposure to 1 bar CO at 373 K. The level of gas cleanliness may be the point where the study by McIntyre *et al.* differs from the present study and this could explain the discrepancies.

5.3.3 Conclusions

The classic prototype system for adsorbate-induced substrate transformations, CO adsorption on Pt(110), was investigated in great detail with STM in the temperature range 300–400 K and pressure range 10^{-9} –1000 mbar. The overall behavior is summarized well by the step-density plot in Fig. 5.20: At first, adsorption at top-layer Pt sites dictates a step density increase through the adsorbates’ preference for low-coordinated sites. When second-layer Pt atoms become exposed, adsorption continues here as well, and adsorption on high-coordinated second-layer sites is minimized by forming the low-kink-density channel structure. This continues until a CO coverage of $\theta \approx 0.7$ where adsorption on high-coordinated second-layer Pt sites removes the preference for the low-kink-density structure and an entropically favored kinked structure is formed. Finally, the energetically favored structure at saturation consists of low-step-density (1×1) substrate areas with a close-packed (2×1) - $p2mg$ -2CO layer on top. This transition to a (1×1) substrate is also explained by the strong dependence of the CO binding energy on the coordination number of the Pt atom to which it binds.

A temperature of 373 K was shown to facilitate the formation of equilibrated structures. At intermediate coverages, a rough structure was observed. From a detailed comparison to MC simulations, we consider this structure to be a manifestation of adsorption-induced step formation.

Adsorption-induced micro-roughening is not limited to the CO/Pt(110) system. Any adsorbate which is attracted to a step atom by an energy comparable to the step formation

energy should induce disordering on any facet. CO also binds strongly to steps of other Pt surfaces [70], and the same has been established for NO, O, N, and C on a number of different transition metals [9, 134, 135]. The underlying reason is that the step atoms with a low coordination number have high energy *d*-electrons, which interact more strongly with adsorbate states [66, 67]. For CO/Pt(110) this is illustrated in Fig. 5.18b. It should be stressed, though, that the strength of the effect is system specific [135].

The effect is particularly strong at fcc(110) surfaces because the metal atoms along steps perpendicular to the close-packed rows are so far apart that each of them can accommodate an adsorbate without strong adsorbate-adsorbate interactions. The coverage can become large at high gas pressures, and adsorption-induced step formation may be possible in general. Our suggestion is that for a number of gas/metal systems high pressures of gases will induce substantial changes in the morphology of the surface at high temperatures. One immediate consequence is that we must expect that, e.g., catalysts can change morphology as a function of gas composition and pressure, and that the distribution of active sites, and thus the catalytic activity, is self-regulated by gas adsorption.

At saturation ($\theta=1$), the Pt substrate heals and forms (1×1) terraces. At pressures above $\sim 10^{-3}$ mbar, a saturated (2×1) -*p2mg*-2CO layer adsorbed on a (1×1) substrate is formed. This structure can also be formed in UHV by cooling from 600 K in a 10^{-7} mbar CO background.

As a common feature at all coverages, substrate transformations are found to proceed through minimal displacements. In particular, a given Pt atom is found to remain on its native terrace.

In conclusion, we emphasize that no new CO phases were observed when raising the CO pressure to 1 bar. The Pt(110) surface thus responds identically to CO under UHV and high-pressure conditions. For this system, however, raising the pressure is *not* exactly equivalent to lowering the temperature since at low temperature the rearranging Pt substrate atoms would not be sufficiently thermally activated to form the equilibrium structure at a given coverage. The high-coverage equilibrium structure can, however, be formed under UHV conditions by cooling the sample in a CO background pressure as discussed above. In the present case, UHV data are still adequate to predict the surface structure at high pressure and elevated temperature. In general one must thus take into account pertinent activation barriers for e.g. substrate equilibration when making conjectures as to the high-pressure response of an adsorption system.

The static structures observed in our HP-STM studies may have limited relevance to real catalytic conditions, since during reactions, adsorbate structures are anything but static. The fundamental implications of our HP studies are however substantial since we demonstrate that no new physical concepts need be introduced.

To lower the bridge across the pressure gap even further, one needs to initiate studies under realistic *reaction* conditions. For the Pt(110) system, reaction studies have been attempted in the case of high-pressure (up to 1 bar total pressure) CO oxidation [136]. In this study, a new reaction mechanism is found consisting of sequential oxidation and reduction with CO, the so-called Mars-van Krevelen redox mechanism. The formation of Pt oxide is not observed in UHV but as in the case of RuO₂ discussed previously [22], the pressure gap has in this case also transformed into a materials gap and the real feat lies in the identification of the true active catalytic material.

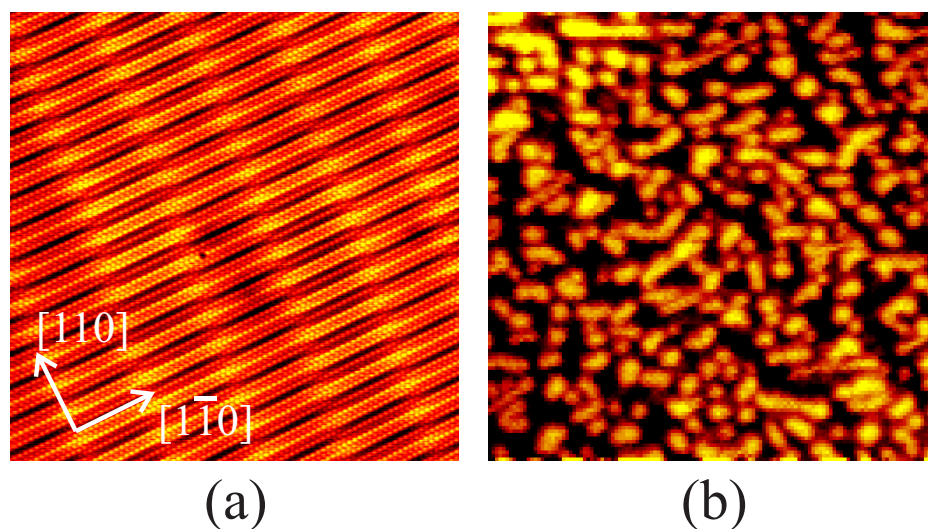


Figure 5.22: Lifting of the Pt(100)-hex-R0.7° reconstruction with CO. (a) Atomsically resolved image of the reconstructed Pt(100) surface ($450 \times 450 \text{ \AA}^2$). (b) Island structure observed upon room-temperature CO exposure ($500 \times 500 \text{ \AA}^2$). Adapted from [137, 138]

5.4 CO on Pt(100)

5.4.1 Previous UHV studies

The Pt(100) surface exhibits a pseudo-hexagonal outermost layer, the so-called hex-R0.7° structure, on top of the square bulk termination, as do the (100) surfaces of Ir and Au. Figure 5.22a shows an atomsically resolved STM images of the Pt(100)-hex-R0.7° structure. In matrix notation, the structure is written $\begin{pmatrix} N & 1 \\ -1 & 5 \end{pmatrix}$, with $N=12-14$ and four rotational domains exist.

CO is known to lift the hex reconstruction and create a (1×1) bulk-terminated substrate. The close-packed hexagonal overlayer contains 20–25% more atoms than the underlying square lattice and as a result, these “extra” atoms are expelled from the top layer and form (1×1) islands when the reconstruction is lifted. $\sim 25\%$ of the surface is then covered with the islands formed from the expelled atoms. In addition, no changes are observed in the original step structure so the islands form exclusively from the expelled atoms. The hex $\rightarrow (1 \times 1)$ transformation proceeds by anisotropic growth of (1×1) areas heterogeneously nucleated at steps and structural imperfections [139]. The growth is much faster along the $[0\bar{1}1]$ direction than along the $[011]$ direction and the resulting islands are elongated in the faster growth direction of the (1×1) phase.

With LEED, CO is found to form a $c(2 \times 2)$ structure with $\theta=1/2$ [140]. Additional adsorption results in $(\sqrt{2} \times 3\sqrt{2})R45^\circ$ ($\theta=2/3$) and $c(4 \times 2)$ ($\theta=3/4$) structures [141]. The $c(2 \times 2)$ structure is thought to contain on top-adsorbed CO only while at higher coverages ($\theta > 1/2$), at least two different adsorption sites are occupied. A sample temperature

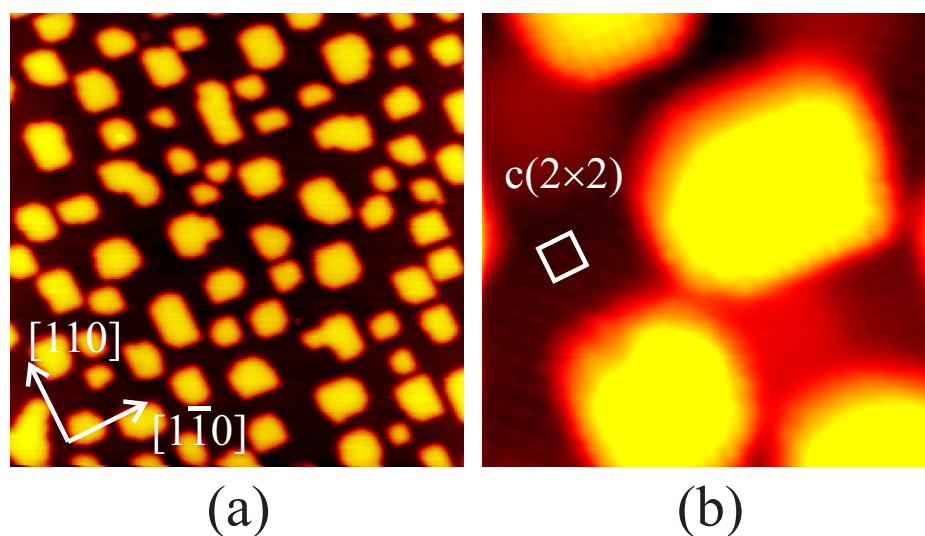


Figure 5.23: CO/Pt(100) annealed to 403 K. (a) Uniformly distributed square islands ($500 \times 500 \text{ \AA}^2$). (b) Patches of the $c(2 \times 2)$ -CO structure are visible ($100 \times 100 \text{ \AA}^2$) [142].

of 395 K is required to observe a well-ordered $c(2 \times 2)$ pattern by LEED [140]. Cooling in a CO background was found to create a well-ordered $c(2 \times 2)$ pattern as well.

5.4.2 Preliminary results

We have in our group performed preliminary UHV studies on the CO/Pt(100) system. Figure 5.22a shows an atomically resolved image of the hex-reconstructed surface. CO exposure at room temperature results in a disordered island structure similar to that observed by Borg *et al.* [139]. After CO exposure, small islands cover $\sim 25\%$ of the surface, corresponding to the excess amount of Pt incorporated into the hexagonal overlayer (Fig. 5.22b). From the STM image, it looks like more than 25% of the surface is covered by Pt islands but this is due to a tip-broadening effect. Once corrected for this effect, we get the quoted number. STM movies show the same anisotropic growth of the (1×1) phase as reported previously. The anisotropic growth is a result of the strongly anisotropic diffusion observed for this system [137].

We observe the $c(2 \times 2)$ -CO structure after annealing the room-temperature structure of Fig. 5.22b to 403 K, see Figs. 5.23a+b. Based on TPD data [143, 144], at this temperature only a small amount of CO is expected to desorb. The annealing produces a uniform distribution of approximately square (1×1) islands formed as a result of the now square substrate. Patches of the $c(2 \times 2)$ -CO structure can be observed between the Pt islands, see Fig. 5.23b.

We note that this behavior resembles that observed on Pt(110) where a sample temperature of 370 K is required to equilibrate the substrate during CO exposure and only

cooling in a CO background forms the saturated $(2\times 1)-p2mg$ structure. A future high-pressure CO experiment on Pt(100) will thus be performed at elevated (~ 400 K) temperature to allow the Pt substrate to equilibrate. We then expect to observe a high-coverage CO structure. To facilitate comparison to the HP experiments, a corresponding UHV experiment must be carried out at low temperatures to reach high coverages. It will however be necessary to lift the hex reconstruction prior to low-temperature CO exposure e.g. by cooling in a CO background. With the same substrate structure in the two pressure regimes, we expect to find identical high-coverage structures at high pressure/high temperature and low pressure/low temperature.

CHAPTER 6

Vacancy-related phenomena on $\text{TiO}_2(110)$

This chapter concerns the most recent studies in this thesis and as such presents a tale in its making. Our incentive for entering the metal-oxide field was to use our HP-STM setup to study gas-induced morphological changes of supported metal clusters. It however turned out that the understanding of the influence from the substrate, $\text{TiO}_2(110)$, lacked crucial pieces of information and more fundamental studies had to be conducted before adding the complexity introduced by high gas pressures. Here we present two studies illustrating the profound impact from intrinsic surface defects, O vacancies, on the dissociation of water and the nucleation and growth behavior of gold nano-clusters. The chapter concludes with a short account of a study of the dissociation behavior of Br_2 on $\text{TiO}_2(110)$. Specifically, we demonstrate the absence of hyperthermal motion following dissociation.

6.1 Introduction

While former chapters in this thesis concentrated on the adsorption behavior of elemental metal surfaces, we now take one step up in complexity into the expanding research area of metal oxides. Metal oxides today play important roles in such diverse areas as corrosion protection, sensors, catalysis, etc. and attract considerable technological and commercial interest.

For catalytic applications in particular, metal oxides are widely used as support material for the actual catalyst material. The traditional support material has been introduced as a means to disperse the catalytically active component and prevent it from sintering during reaction. Recently, however, it has been realized that the support material can have a significant impact on the behavior of a given catalyst formulation. Novel implementations of oxide supports have appeared in which the support takes an active part in the catalytic reaction. The most prominent example is the use of cerium oxide as the oxygen-storage component of the gasoline three-way catalytic converter [13], where cerium serves as an oxygen-liberating component under fuel-rich excursions from the ideal stoichiometric fuel/air ratio. The liberated O spills over to dispersed Pt clusters, which provide the locus for the actual oxidation process. Pt mainly oxidizes unburned hydrocarbons and CO while dispersed Rh clusters reduce nitric oxides (NO_x) to N₂, hence the term “three-way catalyst”.

An example of an oxide in a commercial sensor application is the lambda sensor measuring the O₂ content in the engine exhaust prior to entering the three-way catalyst. This sensor consists of a yttria-stabilized ZrO₂ electrolyte supporting high-surface-area Pt. Under fuel-rich conditions, the Pt component oxidizes unburned hydrocarbons and CO in the engine exhaust and becomes reduced itself. During lean-burn cycles, i.e. at fuel/air ratios below the stoichiometric one, the sensor absorbs O. The voltage drop across the sensor is strongly dependent on the O₂ content and its signal is fed back to a control computer adjusting the fuel/air weight ratio in the combustion chamber to the stoichiometric value around 14.6 [13].

TiO₂ in particular is one of the metal-oxide catalysts that has attracted most research interest over the past thirty years. Part of the interest stems from the ability of photo-activated TiO₂ to split water [145, 146]. Additional interest derives from the role of TiO₂ as a support for metal catalysts, particularly since Haruta *et al.* [10] demonstrated that Au acts as a catalyst for low-temperature CO oxidation when dispersed as nano-clusters on TiO₂ supports. There is however still an ongoing debate concerning the actual mechanism responsible for the catalytic activity of finely dispersed Au particles on the TiO₂(110) surface. The role of surface defects in water dissociation and the nucleation and growth of Au nano-clusters on TiO₂(110) will be the subjects of Secs. 6.5 and 6.6, respectively.

Although of comparable technological importance to metals, oxides have until very recently largely escaped atomic-scale characterization by traditional surface-sensitive techniques owing to the inherent difficulties in applying charged-particle techniques to an insulating sample. Great progress has however been made with the introduction of thin oxide films on metal substrates. This has for example enabled detailed investigations of alumina (Al₂O₃), which has a wide band gap of 8 eV, in the form of a 5 Å ordered

film on top a NiAl(110) single crystal [8]. It should be noted here that atomic force microscopy (AFM) is an emerging technique, which holds the promise of providing atomic resolution on all substrate. Recently this has been demonstrated on the α -Al₂O₃(0001) surface [147]. Another class of oxides—to be identified below—presents the possibility of bulk conduction when slightly reduced and surface science studies on these materials has progressed substantially during the last decade.

6.1.1 Electronic structure of metal oxides

This section aims at identifying the electronic properties, which make metal oxides stand out from metals. A recurring feature is the concept of *ionicity*, which describes the strong desire of O atoms to exist in a Ne 1s²2s²p⁶ configuration and thus formally create an O²⁻ anion. The metallic species in the oxide then formally acquires a net positive charge. As we shall see, the concept of formal charge is especially useful to describe the properties of oxides. To a first approximation it is then appropriate to imagine a metal oxide as a set of spatially localized charges bound together by Coulomb forces. This approximation works better for non-transition metal oxides such as MgO and Al₂O₃ while for transition-metal oxides such as TiO₂ and Fe₂O₃, a substantial contribution to the bonding is of covalent origin but concepts arising from ionicity remain relevant.

The above-mentioned concept of ionicity has profound implications when structural imperfections arise. Coulomb forces are strong and long range so in ionic crystals there is a high tendency to maintain *local charge neutrality* at all times. This explains the creation of a so-called *F-center*¹ created upon removal of an O ion from the crystal lattice. The ion effectively leaves a positively charged vacancy behind but the strong tendency for local charge neutrality then causes two electrons to spatially localize around the vacancy. This *F-center* exhibits discrete electronic states as do free atoms and typically absorb electromagnetic radiation in the visible region. A concrete example of a blue TiO₂ *F-center* is described in Sec. 6.2.1.

In Chap. 5 we showed that on metal surfaces, the chemisorption behavior and reactivity depend critically on local structure, in the case of Pt quantified in terms of the atoms' coordination number. In addition to this effect, for metal oxides a further complication kicks in as a result of the inherent ionicity of their surfaces, namely the effect on reactivity from local *stoichiometry*. To be specific, surface *F-centers*, i.e. O vacancies, can have significant impact on the surface chemistry of oxides. This will be demonstrated in Sec. 6.5 for the case of water on TiO₂(110).

It is also of conceptual interest to subdivide metal oxides into two subgroups: the non-transition-metal oxides and the transition-metal oxides. In the former group, the cation only bonds via *s* or *p* orbitals and can only exist in one oxidation state, e.g. the alkali earths always carry a formal charge of +2, like in MgO. Cations in transition-metal oxides supply bonding *d* orbitals and are polyvalent. This already opens up the possibility of creating at least one oxide per valency with its own structure. For many transition metals there even exists several stable crystal structures for a given cation valency, so-called polymorphs, as will be described for TiO₂ below.

¹From the German word *Farbzentrum*.

6.1.2 Adsorption on metal oxides

Since metal-oxide surfaces generally expose both cationic and anionic species, new and more complex pathways for adsorption are opened as compared to adsorption on metal surfaces. One generally distinguishes between several different bonding interactions, including [148]:

- acid/base or donor/acceptor (without electron transfer)
- oxidation/reduction (with *electron* transfer)
- oxidation/reduction (with *O* transfer)

Surface cations are generally Lewis acids and act as electron acceptors while surface anions (O²⁻) are Lewis bases and donate electrons to acceptor adsorbates.

The first type of interaction does not induce actual electron transfer but should rather be visualized as orbital overlap between empty “acceptor” orbitals and filled “donor” orbitals. This situation is the closest parallel to conventional adsorption on metal surfaces and includes e.g. the adsorption of H₂O molecules on Ti surface cations on TiO₂ to be described below.

A redox reaction occurs in the second type of interaction through electron transfer, a simple example being alkali adsorption on metal oxides. On transition-metal oxide surfaces, however, the existence of several cation oxidation states opens up the possibility of a “redox” reaction through O transfer. This behavior is firmly established on e.g. CeO₂, as described in Sec. 6.1, and RuO₂ [22, 149]. Oxidation of carbon monoxide proceeds through the transfer of a lattice O atom to the CO molecule. For the case of RuO₂(110) it has even been established that defect sites need not be involved for this reaction to occur. As long as a fresh supply of O arrives from the gas phase, the catalytic cycle can run without interruption.

6.2 Rutile TiO₂

Having sketched some general properties of metal oxides, we now turn to a specific case, rutile TiO₂, which has emerged as a model compound to understand the surface physics and chemistry of transition-metal oxides. This prominent position mainly owes itself to the conducting nature of the slightly bulk-reduced crystal so that the whole arsenal of surface-science techniques, as well as standard sputter-anneal cycles, can be employed. Following the increasing number of experimental studies, a large number of numerical calculations have appeared and today the structure of the different rutile TiO₂ facets is known in great detail [35].

TiO₂ is the material of choice for photochemical hydrogen production from water [146, 150] and for biocompatible implants [151]. It also exhibits unusual biocidal properties, i.e. it can photocatalytically oxidize any organic material when exposed to normal levels of sunlight. This effect has obvious sanitary applications for self-cleaning windows and windscreens, reducing the density of pathogenic bacterial colonies, etc.

Photocatalytic oxidation even adds a lesser environmental burden than oxidation upon weathering [152].

Three polymorphs of TiO₂ exist at room temperature: Rutile, anatase, and brookite, each of which occurs naturally. Powder samples contain a mixture between the rutile and anatase polymorphs but only the rutile polymorph can presently be manufactured in bulk samples. This is the main reason that the majority of experimental studies has been conducted on this polymorph but very recently, theoretical and experimental surface studies of the perhaps even more important anatase polymorph have appeared [153–157] thanks to improved sample-preparation techniques. As a matter of fact, the anatase polymorph even displays superior characteristics compared to the rutile polymorph when used for e.g. photocatalytic processes [146] or especially dye-sensitized solar cells [158].

The expanding database of experimental and theoretical studies have concentrated on the rutile polymorph in the hope that it may act as a prototype system where consensus is first established. In spite of these extensive efforts, open questions still remain and this chapter aims to resolve one of these unresolved questions, namely the detailed mechanism for water dissociation on rutile TiO₂(110) [159–161].

The remaining part of this chapter will be organized as follows: First, the structure of bulk rutile TiO₂ and its intrinsic defects are presented as the defects present in the bulk are intimately related to surface defects. Second, as STM will be the main experimental method, it is important to understand in detail the imaging mechanism. Therefore a description of the voltage-dependent imaging of the pristine surface and its intrinsic defects follows. Keeping these results in mind, we then pursue the controversial subject of water dissociation on the rutile TiO₂(110) surface.

6.2.1 Bulk rutile TiO₂ structure

Bulk TiO₂ has a tetragonal unit cell, as shown in Fig. 6.1, with two Ti and thus four O atoms per unit cell. Each Ti atom is surrounded by six O atoms to form slightly distorted octahedra with the four equatorial bond length equal (1.946 Å) and the two apical bonds about 2% longer (1.983 Å). The crystal lattice is built up of these octahedra sharing one corner along <110> type directions and long axes alternately rotated by 90°. This results in O atoms being three-fold coordinated in a planar arrangement.

Depending on the degree of reduction of a given crystal, several different defect-related structures form. The maximum valency for Ti is +4 but a plethora of suboxide phases down to Ti₂O exists. Consequently TiO₂ phase is reduced quite easily through the creation of O vacancies (*F*-centers, see Sec. 6.1.1) and Ti interstitial ions, which manifest themselves as a pronounced color change of the sample from an initial pale yellow over light blue to opaque black for an increasing degree of bulk reduction. Ti interstitials reside at octahedrally coordinated sites in the crystal structure and diffuse more readily than O vacancies, as demonstrated by secondary ion mass spectrometry (SIMS) [162]. The nature of the dominant species is determined by the degree of bulk reduction. It has been determined by electron paramagnetic resonance (EPR) that at low degrees of reduction, both O vacancies and Ti interstitials are present at about equal concentrations. For higher degrees of reduction, the Ti interstitials agglomerate into extended defects, so-called Crystallographic Shear Planes (CSPs), while the vacancy

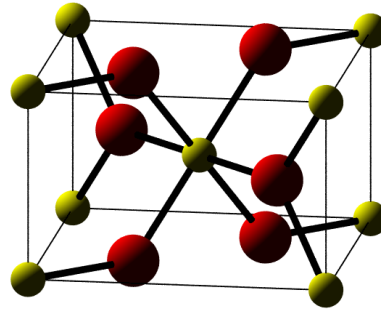


Figure 6.1: The structure of bulk rutile TiO_2 . Yellow: Ti, Red: O.

concentration steadily increases [163].

The creation of O vacancies and Ti interstitials is equivalent to introducing donor impurities so the color centers also induce n -type doping of the bulk crystal and adjoining bulk higher conductivity [164]. Whatever the exact mechanism, the fact that bulk reduction can be achieved by simple annealing in vacuum makes TiO_2 single crystals ideal for the experimentalist.

The easiest way to produce clean and well-defined surfaces is conventional sputter-annealing cycles. As indicated above, vacuum annealing reduces the bulk crystal but preferential sputtering of O surface atoms contributes as well because the surplus of surface Ti after sputtering diffuses to the bulk [162]. During a series experiments on a given crystal, the degree of bulk reduction increases steadily since at the annealing temperature needed to recover from sputter damage and form extended terraces, further bulk reduction is inevitable. Eventually the bulk is reduced to an extent where suboxidic structures start forming at the surface and the old crystal has to be exchanged for a fresh one. Consequently the experimental results presented here originate from a number of samples, but we have found no indications that this should present a problem.

The above facts are important to keep in mind in order to obtain reproducible results since the reduction state of the bulk has profound implications for the surface structure, as will be discussed immediately.

6.3 Structure of the rutile $\text{TiO}_2(110)$ surface

Ramamoorthy *et al.* calculated the surface energies for different low-index terminations of rutile TiO_2 [165]. The (110) surface was found to be the most stable termination. The (110) surface is also expected to be the most stable termination on the basis of bond-counting arguments since the average coordination numbers of Ti and O are maximized as compared to any other termination. Figure 6.2 shows a ball model of the $\text{TiO}_2(110)$ surface. Included is also a number of intrinsic and extrinsic modifications pertinent to the following discussion. The structure of this facet is that of a simple bulk termination,

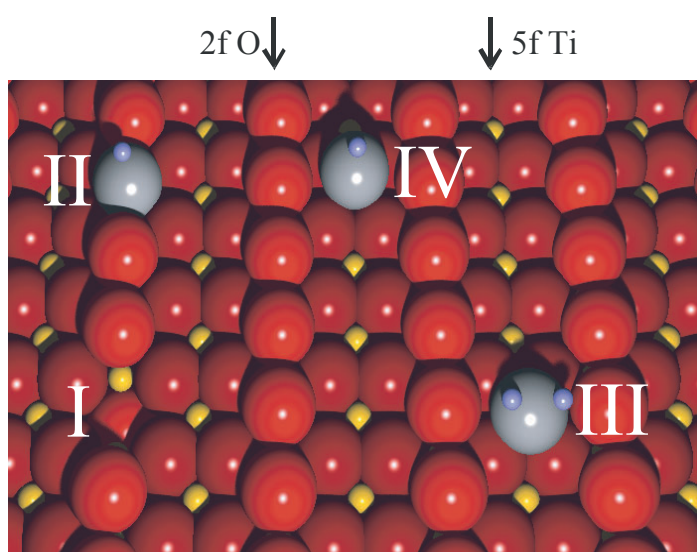


Figure 6.2: Ball model of the $\text{TiO}_2(110)$ surface. The relevant included species on the surface are: I) O vacancy, II) bridging hydroxyl group, III) terminal hydroxyl group and IV) water molecule. Red: O. Yellow: Ti. Blue: H.

barring the expected relaxations due to the lowered coordination numbers relative to the bulk. The two most prominent features on the pristine surface are the rows of five-fold coordinated (5f) Ti atoms and two-fold coordinated “bridging” O atoms in the [001] direction, i.e. both are one-fold *undercoordinated* compared to the bulk. All other atoms retain their bulk coordination. The 5f Ti atoms can be imagined to be formed upon removal of one apical O from all octahedra aligned with their apical bonds perpendicular to the surface. The second apical O resides subsurface while the four O atoms next to 5f Ti are equatorial oxygens (and apical oxygens in adjacent octahedra). The bridging O rows are equatorial O atoms coordinated to six-fold coordinated (6f) Ti atoms, coplanar with the 5f Ti atoms, sitting in octahedra aligned parallel to the surface.

The relaxations of the (110) surface have been the subject of a number of theoretical investigations [165–169]. The calculations generally agree with ion-scattering [170, 171] and surface XRD (SXRD) [172] experiments on the sign of the relaxations while magnitudes seem difficult to reconcile. In particular, experiments find a dramatic inward relaxation of the bridging oxygens of $0.27 \pm 0.08 \text{ \AA}$, implying a Ti-O bond shortening of 12%, while calculations find at most half this value. The reason for this discrepancy has recently been explained by the existence of an anisotropic and anharmonic rigid-unit soft vibrational mode where equatorial TiO_4 units containing the bridging O move in concert perpendicular to the surface plane [173]. This kind of concerted motion has not been included in the analysis of the SXRD data where each atom was assumed to move independently of its neighbors.

6.3.1 Sample preparation

The TiO₂ samples (eSCeTe Single Crystal Technology B.V., The Netherlands) were prepared by multiple cleaning cycles (20 min. 600 eV Ar⁺ sputtering, 40 min. annealing at 1000–1100 K). As discussed above, these cleaning cycles have the effect of reducing the bulk TiO₂ crystal. It is well-known that sputtering preferentially removes O [174] but luckily for the experimenter, the TiO₂(110) surface is forgiving with respect to sputter damage, which can be healed by simple vacuum annealing through transport of excess Ti³⁺ to the bulk [162].

Several complicating features must be added to the deceptively simple scheme described above. First, it is necessary to use a low acceleration voltage for sputtering since the surface reorders rather slowly. Failure to recover from sputter damage results in small irregular terraces. This effect is partially connected to the fact that a precise and reproducible temperature readout is not easily maintained since the thermal contact between thermocouple wires and sample is difficult to control since the thermocouple wires do not adhere well to the backside of an oxide crystal. Small changes to the exact relative configuration of thermocouple wires and sample seem to change the temperature readout by as much as 50 K. This number is then inextricably the precision of the temperature reading and it is thus necessary to check the quality of the clean surface after annealing and, if required, reanneal at a higher temperature or for a longer period of time.

In addition to sputtering and annealing, a reoxidation step can be introduced after sputtering to control the surface stoichiometry, as will be discussed below in Sec. 6.3.3.

6.3.2 Appearance in STM

Before proceeding further, it is important to discuss the “normal” appearance of the TiO₂(110) surface when imaged with STM. Later in Sec. 6.4 we will discuss the voltage-dependent imaging. Figure 6.3 shows a typical STM image of the bare surface. Rows of high local density of states run in the [001] direction. These could naïvely be assigned to rows of bridging O atoms, since these sit proud of the surface by 1.2 Å. It however turns out that with a positively biased sample, i.e. tunneling from occupied tip states into unoccupied sample states, the largest contribution to the tunneling current originated from 5f Ti-derived states, as first pointed out by Diebold *et al.* [175]. This competition between electronic and geometric effects gives rise to STM images where high and low regions are inverted compared to what would be expected on geometric grounds. Simulated STM images based on DFT confirm this as shown in Fig. 6.4a.

6.3.3 Surface defects

The second prominent feature in the STM images in Fig. 6.3 is the bright spots in between bright 5f-Ti rows. The density of this so-called “Type-A defect” [176] is intimately connected to the degree of bulk reduction (“color”) of the bulk crystal. We observe that the density of this feature increases monotonically during a series of experiments while the crystal color changes from transparent to black. The correlation

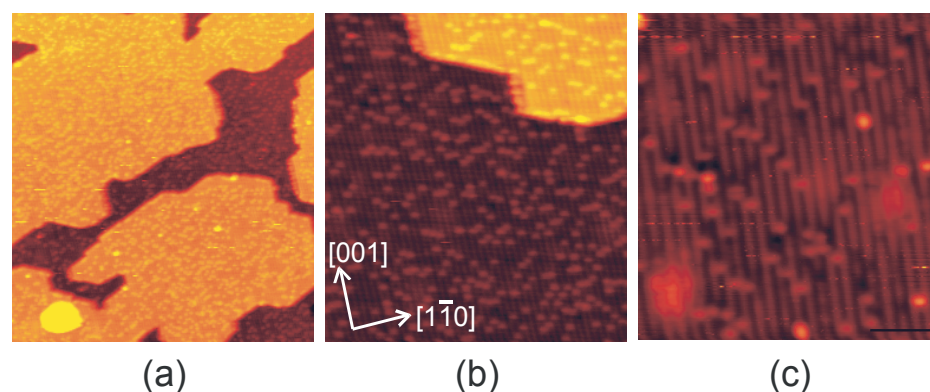


Figure 6.3: STM images of the clean $\text{TiO}_2(110)$ surface. (a) $700 \times 700 \text{ \AA}^2$, $V = 1259 \text{ mV}$, $I = 0.46 \text{ nA}$, (b) $300 \times 300 \text{ \AA}^2$, $V = 1497 \text{ mV}$, $I = 0.49 \text{ nA}$, (c) $100 \times 100 \text{ \AA}^2$, $V = 1250 \text{ mV}$, $I = 1 \text{ nA}$

between the degree of bulk reduction and density (and type) of surface defects has been investigated systematically by Li *et al.* [163].

The chemical nature of the Type-A defects has been the subject of some controversy in the literature. From the above discussion and the fact that high contrast in STM images originates from 5f-Ti atoms, see Fig. 6.4a, it is natural to assume the type-A species to be O vacancies. Our STM simulations support this assignment, see Fig. 6.4b. Recently, however, Suzuki *et al.* [177] observed an increase in the type-A density when exposing the surface to atomic hydrogen, leading to the conclusion that the type-A species should be bridging hydroxyl groups, see Fig. 6.2.

Many other types of surface defects can be found, e.g. subsurface (“Type B” [176]) defects, suboxidic surface species [178–183], or crystallographic shear planes [184], but these only occur for heavily reduced samples. We have been careful only to use slightly reduced samples displaying no other defect structures than Type A defects. This kind of discrimination is easily done by inspection with STM. Although many other interesting effects have been reported in the literature, we shall not discuss these features to any further length.

The density of Type-A defects can to some extent be controlled by using crystals with varying degrees of bulk reduction or by introducing a high-temperature ($\sim 1000 \text{ K}$) oxidation step after sputtering. Sputter damage is already repaired by Ti transport to the bulk during vacuum annealing, which effectively means that the surface is reoxidized by the bulk, hence the term “bulk-assisted reoxidation”. Introducing an oxygen ambient during annealing, however, results in “regrowth” so that extra stoichiometric layers are added [185–191]. When exposed to oxygen, the surface acts as a sink for interstitial Ti and a gradient in chemical potential is set up, which drives Ti to the surface. Here Ti reacts with O to form the new layers. The resulting surface structure is heavily dependent on the degree of bulk reduction, oxidation temperature and time, and gas pressure but

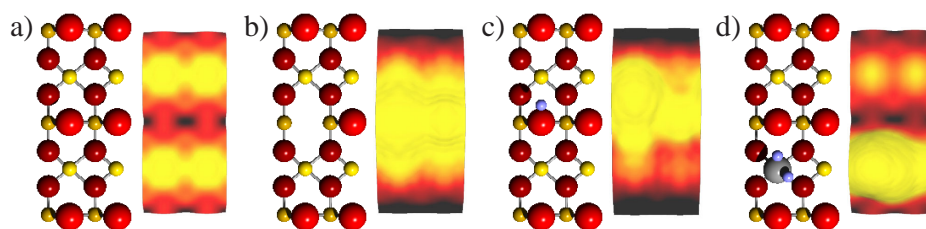


Figure 6.4: Ball-and-stick model and corresponding DFT-based simulated STM image at 1 V showing the appearance of (a) vacancy-free surface, (b) bridging O vacancy, (c) bridging OH group and (d) water molecule atop a five-fold coordinated Ti atom. Red atoms: O, yellow atoms: Ti, blue atoms: H. In (c) the OH bond is tilted $\sim 47.9^\circ$ with respect to the surface normal. Another equivalent configuration exists with a tilt of -47.9° , which would make the simulated STM image symmetric.

we have made sure to use only slightly reduced (“light-blue”) samples and annealing temperature high enough to ensure the creation of a (1×1) top layer. This procedure is also recommended by Diebold *et al.* [35].

The above procedure provides a means of tuning the Type-A density but the final defect density is still dependent on the bulk reduction state as an equilibrium between Ti diffusing into and out of the bulk is maintained during regrowth. It should be noted that it is probably not possible to prepare a 100% stoichiometric surface owing to the necessity of using conducting, and thus bulk reduced, samples. This will have important consequences when we discuss our results on water dissociation on $\text{TiO}_2(110)$ in Sec. 6.5.

The determination of the chemical nature of the Type-A defects will be a crucial point in the following presentation and discussion of our experimental studies of the clean $\text{TiO}_2(110)$ surface and its reaction with water. The ability to unambiguously identify a given surface defect will be a prerequisite for drawing any conclusions on the water dissociation mechanism on $\text{TiO}_2(110)$, as will become apparent later in the last section of this chapter.

6.4 Voltage-dependent STM imaging

Profound insight into the origin of STM image contrast and voltage dependence imaging is of utmost importance before embarking on any serious investigation on a metal-oxide surface. First of all, as we have seen above, for $\text{TiO}_2(110)$ the image contrast is dominated by electronic effects and is inverted compared to what would be expected on geometric grounds. Difficulty also arises when making conjectures about the appearance of structural defects and adsorbates. This is why theoretical input has proven indispensable in aiding the reconciliation of observed features. Added to these complications is the fact that imaging of a metal-oxide surface is strongly dependent on the tip apex configu-

ration and extreme care has to be taken in order to bring out salient features. This section describes and discusses a systematic investigation of the voltage-dependent imaging of $\text{TiO}_2(110)$ surfaces where all of these points will be illustrated.

Our STM software facilitates concurrent image acquisition of a given area, pixel by pixel, but at two different tunneling voltages and/or currents, so-called “double scans”. This approach brings out clearly the contrast changes associated with voltage changes. Put differently, thermal drift and piezo creep are effectively cancelled and this facilitates straight-forward determination of the relative positions of high-contrast features at different voltages. Furthermore, we gain the advantage that we can be sure the tip has not changed between scans. Even small tip changes would have made it difficult to interpret the voltage dependent imaging behavior.

These points are illustrated in Fig. 6.5 showing double scans at different voltages using the most frequent (“normal”) imaging mode. In the literature most published images are recorded in this mode and it has been shown, Fig. 6.4a and [175], that bright rows correspond to 5f Ti rows. Tunneling parameters of +1.25 V on the sample and 1 nA are representative of typical tunneling values. We find that a stable tunneling current can be maintained down to ~ 0.5 V. Scanning at negative bias is not practical since one has to use high negative voltages (< -3 V) in order to overcome the band gap.

The contrast in 5f Ti rows increases with lower voltage as would be expected when approaching the tip closer to the surface. At the lowest voltages, atomic corrugation appears along the 5f Ti rows. Type-A defects stand out clearly at tunneling voltages above 1 V, see Fig. 6.4b, but their relative contrast decreases for decreasing tunneling voltage and they almost disappear at the lowest voltages.

The above findings are not surprising but we frequently encounter a second, “enhanced” mode. This mode is stable for extended periods of time enabling the acquisition of double scans as in the normal mode. Figure 6.6 demonstrates the dramatic image (re)inversion occurring at low voltages. We also notice some influence from subsurface defects but these do not change the overall conclusion that bridging O rows are imaged at low voltages, i.e. at small tip-sample separations. This interpretation is supported by theoretical studies, which predict this very behavior [175, 192–194]. From this point on, however, we shall report “normal” imaging mode images only in order to avoid confusion.

We mainly include these latter double scans to point out that images published in the literature [178, 181] displaying two features per unit cell must have been recorded in this mode. The images in the latter reference were recorded with high current and low voltage (+0.75 V and 2.0 nA) but owing to the lack of the double scan feature it was not possible to unambiguously determine the identity of each species.

Returning now to the chemical nature of the Type-A defects, the first hint at a possible reconciliation of the two propositions put forth in the literature comes from double scans performed on the pristine surface but after leaving the crystal in the UHV chamber about 2 h at $< 10^{-9}$ mbar after the end of the annealing cycle, see Fig. 6.7. We see how the imaging of seemingly equivalent Type-A defects respond differently to a decrease in voltage, e.g. in the case marked by the white circle. Scrutinizing this and many similar high-quality images, we even detect two, and only two, distinct Type-A defects. Their main difference in appearance is their extent in the [001] direction (e.g. 6.6 Å vs. 4.8 Å)

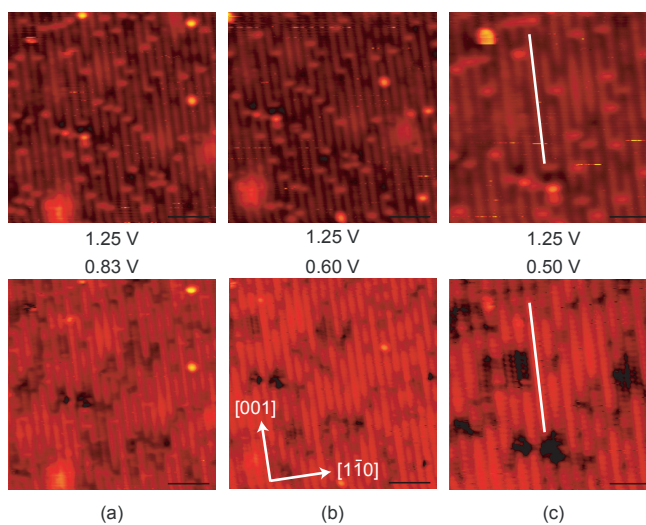


Figure 6.5: Three sets of double scans in the “normal” imaging mode on $\text{TiO}_2(110)$. A white line is drawn in (c) to indicate that 5f Ti rows are imaged as protrusions at all voltages. (a+b) $100 \times 100 \text{ \AA}$. (c) $70 \times 70 \text{ \AA}$. All images $I_t = 1 \text{ nA}$.

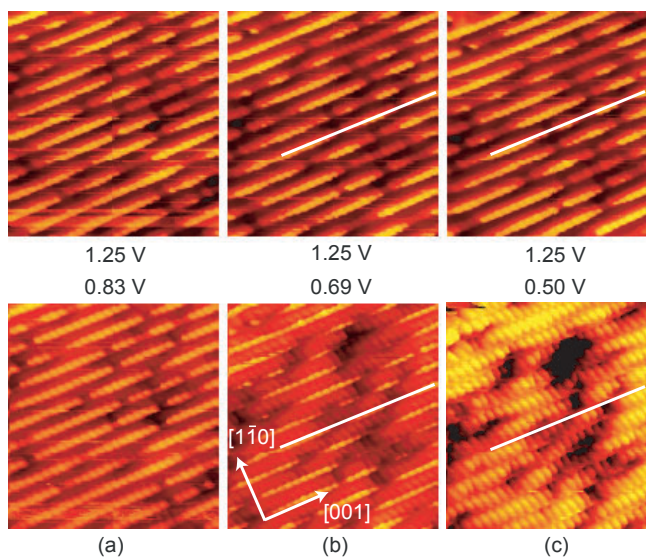


Figure 6.6: Three sets of double scans in the “enhanced” imaging mode. A white line is drawn to indicate that regions of high contrast shift from 5f Ti rows to 2f O rows. (a-d) $70 \times 70 \text{ \AA}$, $I_t = 1 \text{ nA}$.

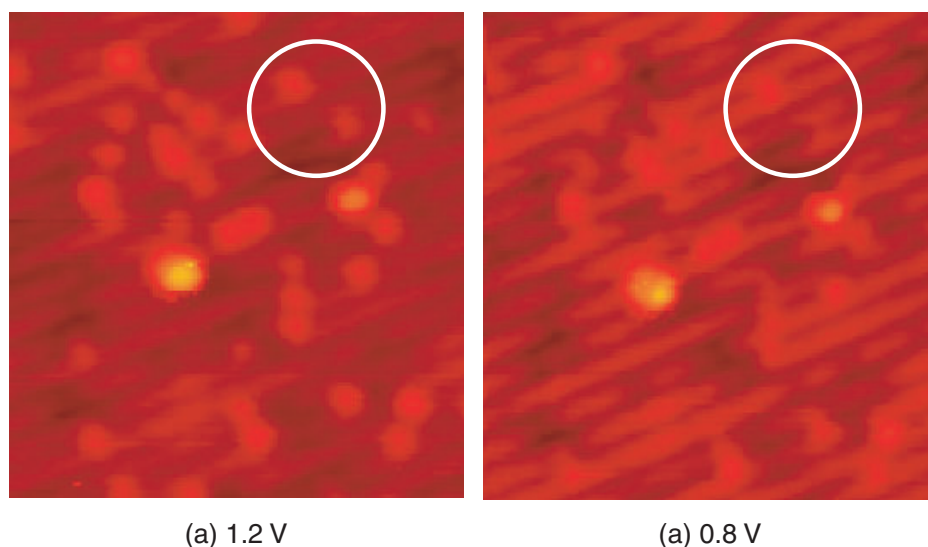


Figure 6.7: A first indication of the existence of two distinct Type-A defects. The white circle marks an occurrence where the imaging of two neighboring Type-A defects respond differently to a decreasing tunneling voltage. (a+b) $300 \times 300 \text{ \AA}$, $I_t = 1 \text{ nA}$.

and their apparent height (e.g. 0.4 \AA vs. 0.2 \AA), see the line scans in Fig. 6.8. This kind of distinction cannot be made between images, i.e. each image has to be scrutinized separately, since different tip conditions change the absolute values for the extent and height. We hence propose that the Type-A is not merely one but two different species, tentatively proposed to be O vacancies and bridging hydroxyl groups. At this point it is not possible to exclude a different chemical nature of one or both types but the above proposition will be amply validated in the next section on water dissociation. With this working hypothesis at hand, the STM image simulations in Fig. 6.4b+c allows us to preliminarily conclude that the slightly higher and wider species are O vacancies and the second species are bridging hydroxyl groups. This is the starting point for the next section on water dissociation on TiO₂(110).

6.5 Water dissociation on TiO₂

6.5.1 Motivation

Water adsorption and dissociation on TiO₂ is of fundamental interest as an example of a simple surface chemical process with significant applications. Recent great interest in titania was initially derived from the discovery of photoelectrolysis on rutile TiO₂ [145, 150] but many more technological applications have emerged. An illustrative example is the insertion of a (hopefully) biocompatible implant consisting of Ti metal. In air, Ti

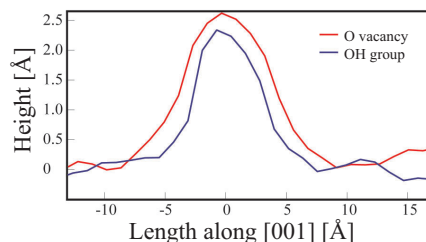


Figure 6.8: Line scans along the [001] direction showing the different heights and extensions of O vacancies and bridging hydroxyl groups.

is always covered by an thin TiO_x layer so this is the material the bodily fluids encounter after the surgical procedure. Water and hydrated ions being very light compared to cells, they rapidly cover the implant surface, forming a hydration, or so-called Helmholtz, layer [195], and any cell is bound to meet a water-saturated Ti oxide layer. Although the detailed structure will be dynamic, its structure is likely to be very different from that of liquid water [151]. This further emphasizes the importance of understanding the water adsorption and dissociation processes in detail.

Earlier experimental studies report a minor degree (few %) of water dissociation on TiO₂(110) [159–161, 196] while theoretical studies predict the dissociated state [197–200], or mixed dissociated-molecular states [201], to be most energetically favorable. From these theoretical studies it has been realized that conclusions about the reaction path depend heavily on the exact three-dimensional geometry of the final products [198, 202]. Furthermore, recent calculations predict dissociation to be endothermic [203]. Thus, even for this simple process we do not have a clear picture of the dissociation energetics and the active site for dissociation.

In this section we use a combined experimental and theoretical approach to show that, at low coverages, water dissociation takes place exclusively on defect sites associated with O vacancies. We demonstrate that a direct correlation exists between O vacancies before water exposure and surface hydroxyl groups after water exposure. By the use of DFT we indeed show water dissociation to be energetically feasible only at the defect sites.

6.5.2 DFT calculations

For theoretical modelling, our collaborators from Nørskov’s group performed DFT calculations applied to periodic slab models.² Simulated STM images have been obtained

²Each slab contains three O–Ti₂O₂–O planes and slabs are separated by 10 Å of vacuum. Water is adsorbed only on one side, and the resulting dipole moment has been corrected for in the vacuum region. The ionic cores have been described by ultrasoft pseudopotentials [204] and the one-electron valence states are expanded in plane waves with kinetic energies up to 340 eV. A Monkhorst–Pack grid of (8×4×1) **k**-points has been used for the smallest (1×1) surface unit cell and reduced appropriately for larger super cells. Electron densities

by applying the Tersoff-Hamann approximation [58] where the tunneling current is proportional to the LDOS. The effect of finite bias has been introduced by adding up contributions from states lying between the Fermi level and the applied voltage as in a previous study of the TiO₂ surface [175]. The voltage considered to model the images is 1 V, similar to the voltage used in the STM experiments (see below). The simulated images have been obtained at a constant density of $3 \cdot 10^{-6} \text{ e}/\text{\AA}^3$, since at this value experimental and theoretical corrugations for the stoichiometric surface are similar.

6.5.3 Experimental results and discussion

Exposing the clean samples (Fig. 6.9a) to a low dose (10^{-2} L) of water at room temperature leads to the situation shown in Fig. 6.9(b).³ We again observe the bright Ti rows and type-A defects between the Ti rows. As discussed above, both vacancies and hydroxyl groups give rise to protrusions but vacancies are clearly more extended than hydroxyl groups.

If we compare Figs. 6.9(a), the clean surface, and 6.9(b), the surface after water deposition, the number of type-A defects has doubled. For the clean surface in Fig. 6.9(a) the type A defects are almost exclusively O-vacancies, while in Fig. 6.9(b) the type-A defects are OH groups. If we instead expose the surface to 10^{-2} L of water at low temperature (180 K), Fig. 6.9(c), we again observe a doubling of the type-A defect density, but an additional brighter feature is present, which we ascribe to molecularly adsorbed water. From the atomically resolved STM images (see Fig. 6.9(d)) we determine the adsorption site of molecular water to be on top 5f Ti atoms. Furthermore, Fig. 6.9(d) confirms that all OH groups are situated at bridging O sites; we never observe terminal OH groups. This suggests that water adsorbs dissociatively in O vacancies and via proton transfer to a neighboring bridging O atom creates two bridging hydroxyl groups per initial vacancy. O vacancies thus act as the active site for water dissociation on the TiO₂(110) surface.

We note that even at low temperatures, we do not observe pairs of OH groups which could be assigned to originate from a single water-dissociation event. This implies that either i) the H atoms are mobile even at low temperatures or ii) after dissociation, the dissociation fragments repel each other. Some repulsion must exist between OH groups since it is evident that they distribute evenly across the surface and we specifically never observe adjacent OH groups. More insight could be gained by recording STM movies of (possibly) diffusing H atoms.

A prerequisite for dissociation to occur is the mobility of water molecules and hence their ability to reach the active sites. From time-resolved STM movies⁴ [125] we have

have been self-consistently determined with the PW91 exchange-correlation functional [127] by iterative diagonalization of the Kohn-Sham Hamiltonian. Fermi population of the Kohn-Sham states ($k_B T = 0.2 \text{ eV}$) and Pulay mixing of the resulting electronic density have been employed. Energies are extrapolated to $k_B T = 0 \text{ eV}$ and their final evaluation has been performed using the revised version of the Perdew-Burke-Ernzerhof (RPBE) exchange-correlation functional [56].

³Deionized water, cleaned via freeze-pump-thaw cycles, was introduced into the UHV chamber through a leak valve.

⁴See: <http://www.ifa.au.dk/camp/hot0021.htm>

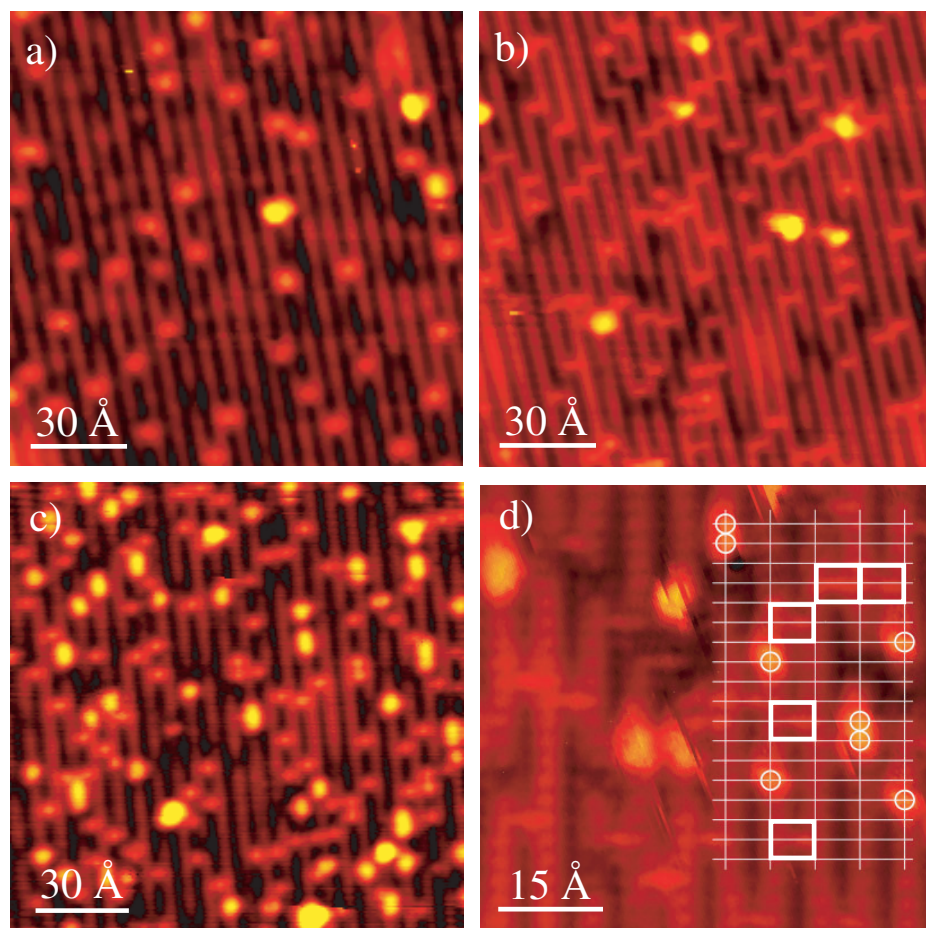


Figure 6.9: The $\text{H}_2\text{O}/\text{TiO}_2(110)$ system. (a) The bare surface imaged at room temperature. (b) After 10^{-2} L of H_2O exposure at room temperature. (c) After exposure to 10^{-2} L of H_2O at 180 K, imaged at 160 K. (d) Same conditions as c. A grid is superimposed to identify the water adsorption site (marked by circles) and the location of an OH group (marked by squares). The small amount of very bright spots in (a) and (b) is unidentified pollution.

observed that the water molecules diffuse at 160 K at time scales of seconds, consistent with Henderson's findings [160].

TPD spectra obtained after submonolayer water deposition at low temperature show two peaks at ~ 290 K and ~ 490 K. When annealing higher than 290 K, we no longer observe the bright feature associated with molecularly adsorbed water. Annealing above 490 K leads to the disappearance of the OH species, reverting to the initial surface defect density. Correlating TPD and STM data we can thus conclude that the higher temperature peak is associated with recombinative desorption of the bridging hydroxyl species, in agreement with Ref. [205].

DFT calculations support the above interpretation in that they show dissociation of water to be energetically favorable *only* at O vacancies (see Fig. 6.10). When we consider "low" coverages (0.25 ML water coverage, (2×2) super cell), the dissociation of water on the perfect TiO₂(110) surface is endothermic by 0.23 eV, in line with [203]. Since the water molecule binds quite strongly to the surface by 0.56 eV, the dissociated state is even more endothermic relative to molecular adsorption. This is in contrast to the result of an earlier calculation by Lindan *et al.* [201]. Here dissociation is found to be exothermic on the perfect TiO₂(110) surface.⁵

Including now the effect of 0.25 ML of O vacancies, we find water dissociation to be strongly exothermic, even with respect to molecularly adsorbed water (see Fig. 6.10). Dissociation at O vacancies gives rise to two equivalent bridging OH groups on the surface where the water O has been incorporated into the vacancy. The reason for the larger reactivity of the vacancies is clearly associated with the high-energy defect. When water dissociates, the coordination shell of the Ti underneath the vacancy is refilled, resulting in the exothermicity.

To further substantiate the results presented above, we carried out a number of quantitative water exposure experiments at room and low temperature for surfaces with different initial surface defect densities (O vacancies and hydroxyl groups originating from the low but finite water background pressure in the UHV chamber). The defect density can be tuned in a reproducible way by using crystals with varying degrees of bulk reduction and by varying the annealing time in oxygen background and/or UHV. Note that at room temperature, hydroxyl groups have still not desorbed (as H₂O) from the surface, as illustrated in Fig. 6.9b, while water molecules have desorbed.

Figure 6.11(a) shows a plot of the type-A defect density at different stages in the experiments, where first the clean surface was exposed to a certain amount of water (see "Deposition" column). Subsequently, the sample was flash-annealed to 873 K (indicated

⁵We also find this at high coverages. For a (1×1) unit cell dissociation is exothermic relative to molecularly adsorbed water by 0.2 eV, the reason being that at this high coverage chains of hydrogen-bonded OH groups can form along the [001] direction. We note that a small exothermicity may be counteracted by entropic effects and that exothermicity is a necessary, but not sufficient, condition for dissociation. Only for very exothermic processes do we expect the barrier for dissociation to be small. These findings are in line with a recent Car-Parrinello simulation [206]. Here the dissociated state with two bridging OH groups is found to be stable although a water molecule placed in a vacancy does not dissociate spontaneously, i.e. dissociation in a vacancy is found to be an activated process. In the calculation by Lindan *et al.* [201] the unit cell used is such that all OH groups have nearest neighbors in the $[1\bar{1}0]$ direction, and this is likely to be the reason for stronger bonding. The high coverage limit is, however, of limited interest for the understanding of the initial low coverage dissociation of water considered here.

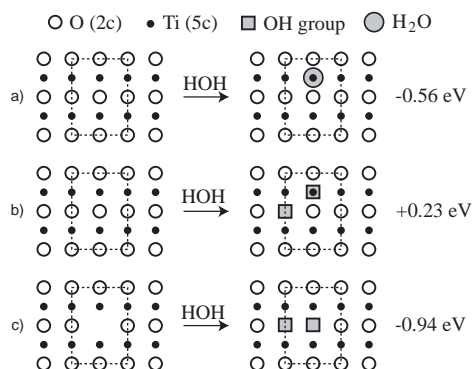


Figure 6.10: Energetics for processes associated with water adsorption processes at low coverages. (a) Molecular adsorption on TiO_2 ; (b) dissociative adsorption at a 5f Ti atom; (c) dissociative adsorption at an O vacancy. The unit cell employed in the calculations is indicated.

with “Flash”) and in some cases another deposition was carried out. Upon normalization to the initial vacancy density and correction for the presence of both type A species it becomes apparent that the density of type-A defects double, as shown in Fig. 6.11b. This is in agreement with our previous explanation that for every initial O vacancy, two hydroxyl groups are created. Hydroxyl groups are desorbed upon annealing but can be recreated upon another water exposure. This demonstrates unambiguously that the active sites for water dissociation on $\text{TiO}_2(110)$ are O vacancies.

It should be mentioned at this point that other pathways for water reactions may well exist when O in the form of a molecular adsorbate (O_2), superoxo (O_2^-), or peroxy (O_2^{2-}) is present on the surface. The possibility arises because a highly reactive O species is created upon O_2 exposure of a $\text{TiO}_2(110)$ surface exhibiting O vacancies. This species (adsorbed ontop 5f Ti) is created whenever the reduced surface is exposed to O_2 since one atom fills the vacancy and the other fragment is free to subsequently participate in the formation of one of the above mentioned species [207]. Which one of the species is actually created is still a matter of controversy but it has been suggested that i) the O adatom left from the O_2 filling a vacancy may abstract a hydrogen atom from a water molecule adsorbed on 5f Ti [208] or ii) water may protonate a peroxy ion to hydroperoxy (HOO^-) since this species has been shown to participate in photocatalytic oxidation on titania surfaces [207, 209].

6.5.4 Conclusion

From an interplay between experiment and DFT calculations we have determined the active site for water dissociation on the defected rutile $\text{TiO}_2(110)$ surface to be an O vacancy. In order to reach this conclusion we have used our ability to distinguish the

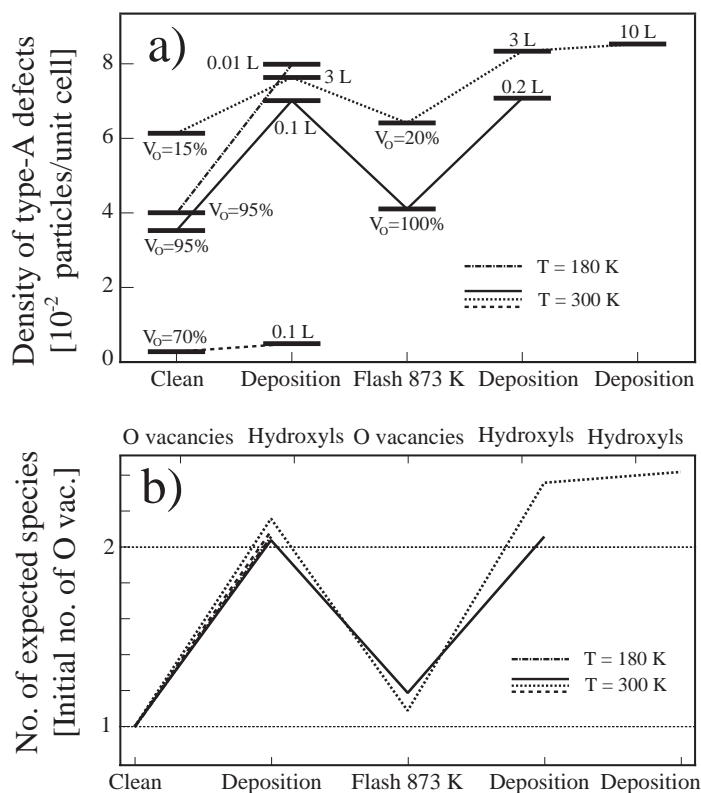


Figure 6.11: Quantitative analysis of the number of type A defects before and after exposure to H₂O. (a) Density of type A defects for different, widely varying starting configurations. (b) Corrected and normalized type A defect density plot demonstrating the 1:2 correspondence between the density of O vacancies and hydroxyl groups. Above each step the type of species expected to be present on the surface is noted. In cases where vacancies are the expected species, we correct for the presence of hydroxyl groups by letting two hydroxyl groups count for one vacancy. V_O denotes the percentage of O vacancies in the total density of type A defects.

two defect species, O vacancies and bridging hydroxyl groups, in high-resolution STM images. We have presented evidence for the vacancy dissociation mechanism on the adsorbate-free surface but further complications are likely to exist when O-containing adsorbates are present on the surface. At present we are pursuing the question of the rather complex O-related chemistry on the TiO₂(110) surface.

6.6 Nucleation and growth of Au on TiO₂(110)

6.6.1 Motivation

As mentioned in the introduction to this chapter, our original purpose for entering the metal-oxide field was to study pressure-induced morphology changes of supported metal clusters. Having characterized the bare TiO₂(110) surface in detail, we are now prepared to investigate the properties of metal clusters deposited onto it. An especially interesting metal is Au, which displays a surprisingly high activity for CO oxidation when dispersed as nano-clusters on TiO₂ [10]. It has been shown that the size of the Au clusters has a significant effect on the catalytic activity, with a maximum in activity for ~ 30 Å wide Au clusters [11, 210]. As in the case of water dissociation on TiO₂(110), we however found that essential pieces of fundamental insight are currently lacking and it was therefore necessary to investigate the nucleation and growth of Au clusters on TiO₂(110) in more detail.

It is important to investigate the exact nature of the metal/oxide bond to understand not only the growth mechanism of metal clusters, but also to reveal the fundamental processes behind the catalytic activity of oxide-supported metal catalysts [15, 16]. It is speculated that surface defects may alter the electronic configuration of Au nano-particles to enable catalytic reactions such as CO oxidation. Small Au₈ clusters on another oxide support, MgO(100), were recently shown both experimentally and theoretically [12] to be active for CO oxidation only if the Au clusters nucleate at O vacancies.

Here we present a detailed study of the interaction of Au nano-particles with bridging O vacancies. Through an interplay between high-resolution STM and DFT we show that the nucleation and growth of Au clusters on the rutile TiO₂(110) surface is intimately related to the presence of surface O vacancies, and that larger Au clusters bind very weakly to the stoichiometric surface. By monitoring the temperature dependence of the Au cluster size distribution and the O vacancy density we find that an O vacancy accommodates 3-5 Au atoms on average. We show that medium-sized clusters (area ~ 250 Å²) are destabilized at room temperature (RT), providing evidence for mobility of Au-vacancy complexes. A new growth model for Au/TiO₂(110) is presented.

6.6.2 Experimental results and discussion

Au was deposited from an e-beam evaporator (Oxford Applied Research). The evaporation rate was calibrated from STM measurements of Au deposited at 300 K on a Ni(111) surface (see e.g. [211]) to be 0.01 ML/min.⁶ A +2.5 kV potential was applied

⁶One monolayer is defined as the packing density of an Au(111) plane, $1.39 \cdot 10^{15}$ atoms·cm⁻²).

to a nearby electrode in order to hinder any charged Au atoms from impinging on the sample surface. In all images shown, the sample was cooled down from, or kept at, the deposition temperature during imaging. During sample transfer to the STM a short rise in temperature occurs, estimated to be 10–20 K. As will be shown below, Au clusters bind very weakly to the stoichiometric surface. As a consequence, they can be dramatically influenced by the scanning process: at currents higher than 1 nA, a majority of Au clusters disappear from the scanning area. A new preamplifier has been developed to facilitate the lowest possible tunneling currents and high feedback gains. All presented STM images are acquired with <0.1 nA and 1.2 V.

Figure 6.12a shows an STM image of the clean surface prior to Au deposition. In the previous section, we demonstrated the ability of our STM to distinguish between O vacancies and OH groups, the latter originating from the dissociation of water molecules at O vacancy sites. In the present study, special care has been taken to avoid water contamination, and we can therefore safely assign the bright spots between Ti rows to single O vacancies.

After Au deposition, we observe Au clusters on the surface (Figs. 6.12b–d). The size of the clusters depends on the deposition temperature. At the lowest temperature (130 K), most of the clusters contain only a few atoms and are homogeneously distributed on the terraces. High-resolution STM images reveal that the smallest protrusions found (Fig. 6.13a, height ~ 1.7 Å, width 10 Å) are located on the bridging O rows. We assign these to single Au atoms adsorbed in a bridging O vacancy (further evidence will be provided below). With increasing deposition temperature, the average cluster density decreases and the average cluster size increases accordingly, see Fig. 6.12c+d. At 210 K, the clusters are still distributed homogeneously on the terraces but contain on average 10 atoms. However, at 300 K (RT) the clusters preferentially nucleate at step edges and contain ~ 30 atoms.

To quantify the interaction of Au clusters with O vacancies, we have in high-resolution STM images counted the number of vacancies as well as the number of clusters before and after Au deposition at the different deposition temperatures (Fig. 6.15). When Au is deposited, we find that at all investigated temperatures, the density of O vacancies decreases. This decrease is clearly not due to a “shadowing” effect from the Au clusters since they occupy < 15 % of the surface area, and thus cannot account for the observed decrease in number of vacancies. At the lowest temperature, we find close to a 1:1 correlation between the increase in number of Au clusters and the decrease in the number of O vacancies. At higher temperatures, the decrease in the number of O vacancies is considerably larger, indicating that the clusters trap several O vacancies beneath them, as seen more vividly in Fig. 6.14. This shows unambiguously that the clusters bind at O vacancy sites at all investigated temperatures.

In Table 6.1 we have further quantified and summarized the experimental findings of Fig. 6.15 and listed the number of Au atoms per cluster, the vacancy/cluster ratio and finally the number of Au atoms per vacancy for different sets of deposition temperature and Au coverage. It should be stressed here that the numbers are averaged over many STM images. We notice from Table 6.1 that the number of O vacancies trapped under each Au cluster increases with deposition temperature for a fixed coverage, but most importantly, we find that the number of Au atoms per O vacancy is 3–5 in all cases.

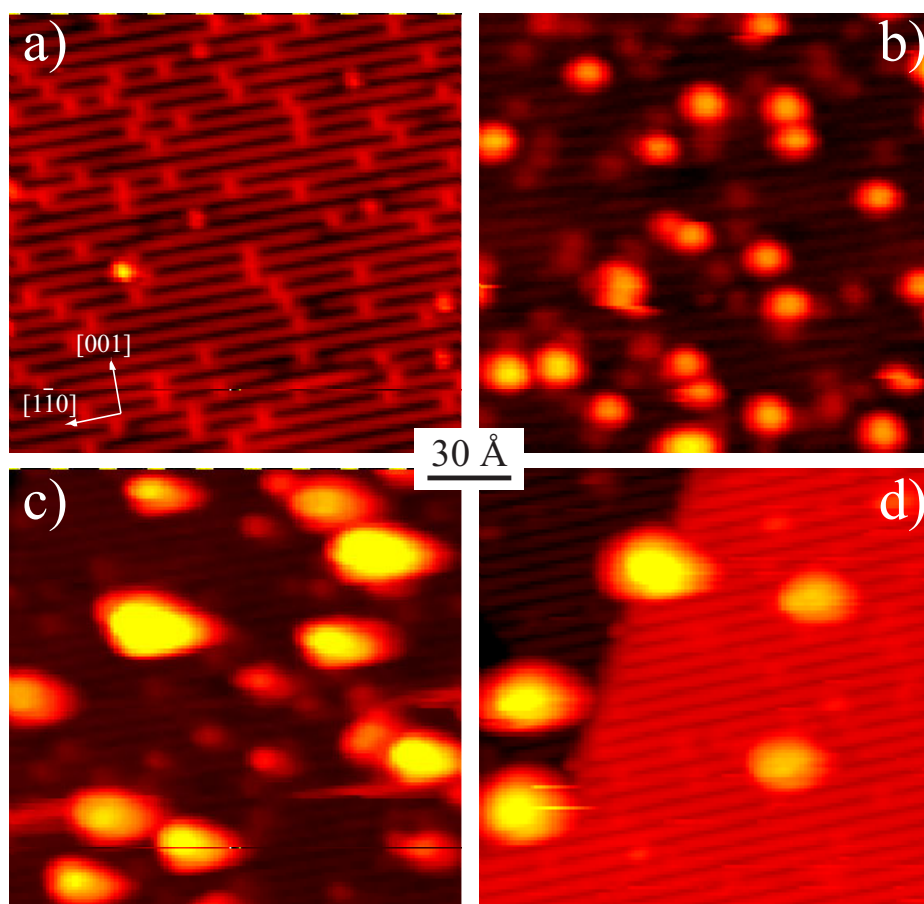


Figure 6.12: (a) Clean $\text{TiO}_2(110)$ surface with bridging O vacancies. (b) to (d) $\text{TiO}_2(110)$ surface after 0.04 ML Au deposition at 130 K, 210 K and 300 K, respectively.

Coverage (ML)	T (K)	Au atoms/clust.	Vac./clust.	Au atoms/vac.
0.005	125	1-3	1	1-3
0.005	300	7	2	3
0.02	151	5	1	5
0.04	130	5	1	5
0.04	210	9	3	3
0.04	300	28	9	3

Table 6.1: Interaction between O vacancies and Au clusters grown at different temperatures and coverages.

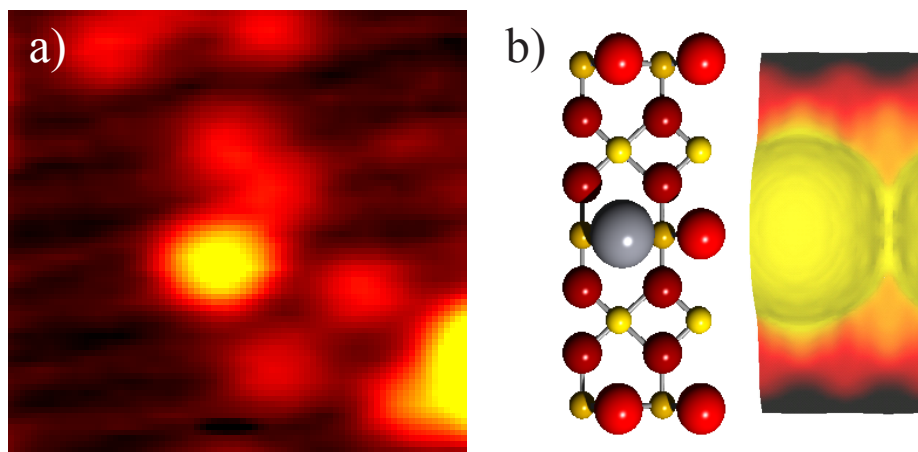


Figure 6.13: (a) A close-up STM image of one of the smallest clusters observed, note the location on top of the bridging O row. (b) Simulated STM image of a single Au atom trapped in an O vacancy. A model of the (2×2) surface unit cell used in the calculations is included.

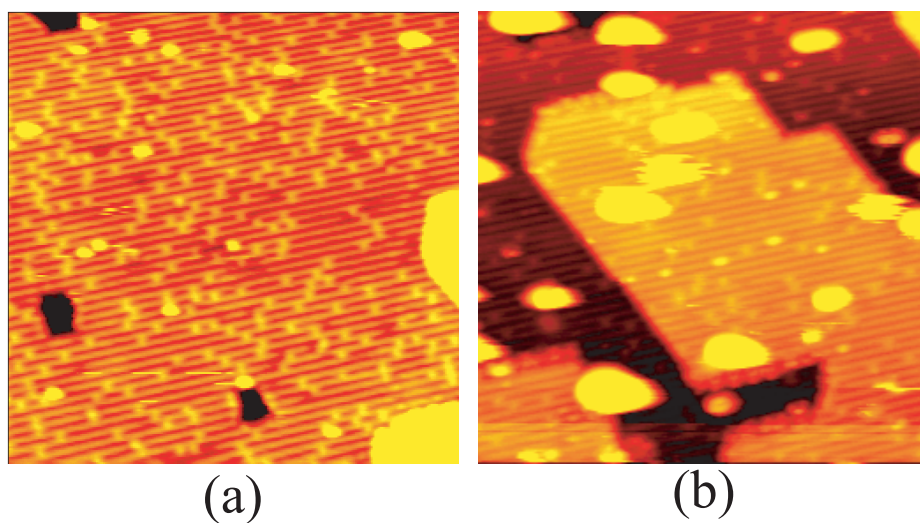


Figure 6.14: Illustration of vacancy-density decrease after Au deposition at room temperature. (a) Image of the bare surface ($300 \times 300 \text{ \AA}^2$). (b) Image after 0.04 ML Au deposition. The decrease in bright features between bright rows is clearly seen.

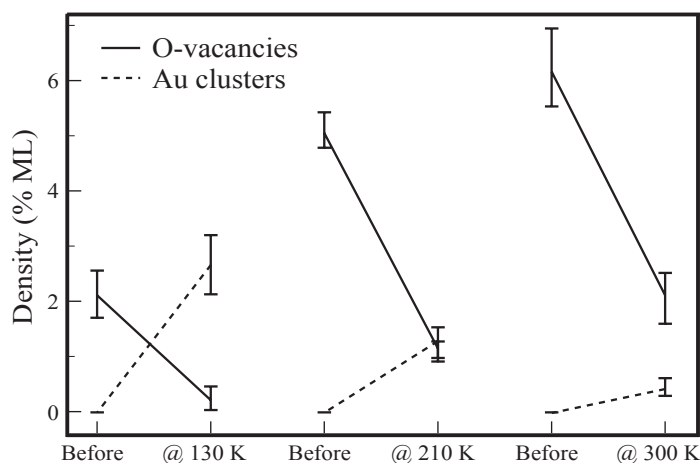


Figure 6.15: Density of O vacancies and Au clusters before and after deposition of ~ 0.04 ML Au at different temperatures. 1 ML = 1 vacancy or cluster/TiO₂(110) unit cell = $5.13 \cdot 10^{14} \text{ cm}^{-2}$.

N. Lopez from J. Nørskov's group used DFT to determine the binding site of Au on the stoichiometric and reduced TiO₂ surfaces. It is found that Au is very weakly bound to the stoichiometric surface. A single Au atom binds by 1.55 eV to the stoichiometric surface, but adsorption of a full Au monolayer (as a model of a larger cluster) is almost a thermoneutral process [212] (this fact is consistent with the difficulties arising when imaging the Au/TiO₂(110) system by STM as previously stated). The Au-Au interactions thus dominate for larger clusters and makes the Au-TiO₂ adhesion extremely small.

For a single Au atom, the most stable configuration is found to be adsorption in an O vacancy site. This configuration is more stable by 0.45 eV than Au adsorbed on the most favorable site at the stoichiometric surface (on top of a bridging O atom), and by 0.80 eV with respect to adsorption on top of a five-fold coordinated Ti atom. The Au bond on the stoichiometric surface originates from bond polarization while the Au-vacancy bond is covalent with a very small (if any) charge transfer. This is different from Au adsorption in a vacancy on MgO where significant charge transfer occurs [12].

The smallest protrusions between Ti rows observed experimentally are only reproduced in simulated STM images when a single Au atom substitutes the missing bridging O atom (see Fig. 6.13b). These findings confirm the interpretation that the smallest protrusions centered on the bridging O rows are single Au atoms trapped at O vacancies.

For low coverages, the attachment energy of a cluster adsorbed at a vacancy, i.e. the energy gained by increasing the number of Au atoms by one (inset in Fig. 6.16), has been calculated. One finds a relative instability of a cluster containing two Au atoms compared to a single atom adsorbed on the O vacancy and a diffusing Au atom (on the Ti [001] row). In addition, Au₃ is more stable than an adsorbed dimer, indicating relatively

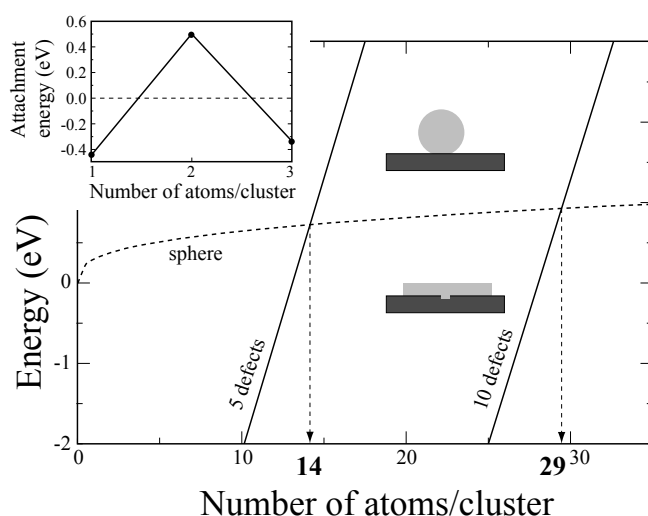


Figure 6.16: Transition between Au adsorption on O vacancies and diffusion. Solid lines represent the energy for the Au disk adsorbed on a given number of O vacancies (indicated in the graph). The dashed line shows the limit for diffusion, and the dashed vertical arrows indicate the actual number of Au atoms in the cluster at which the transition occurs. The inset shows the attachment energy for Au_n (n=1-3) adsorption on TiO₂(110).

higher stability of the trimer towards decomposition. Moreover, Au₄ has an electronic configuration similar to Au₂ [213] and we expect it to bind weakly to a vacancy.

For large clusters, the stability of a monolayer cluster (represented by a disk attached to a varying number of vacancies) to the stability of a 3D Au cluster on the stoichiometric surface (represented by a sphere)⁷ can be compared through a continuum-like model. This model gives an estimate for the number of Au atoms stabilized per vacancy. The results are summarized in Fig. 6.16. If no vacancies are attached to the Au cluster, a 3D cluster is always the more stable configuration but if vacancies are included, a 2D island up to a certain size will be more stable than a 3D (freely moving) cluster. The maximum number of Au atoms stabilized by a group of vacancies is given by the intersection of the curves representing the two configurations. With a large number of vacancies under the deposit, such as 5 or 10, the maximum number of Au atoms per vacancy that can be stabilized and adsorbed in a disk-like structure is about 3. This correlates very well with the experimental observations in Table 6.1.

To investigate the mechanism of nucleation and growth of Au clusters in light of the strong Au-vacancy interaction presented above, we plot in Fig. 6.17 the size distribu-

⁷The energies are as follows: for the disk $E_{\text{disk}} = E_{\text{d}}n_{\text{d}} + \gamma_0 \cdot N \cdot 2 + E_{\text{edge}} \cdot N^{1/2}$ and for the sphere $E_{\text{sphere}} = \gamma_0 \cdot N^{1/3}$. E_{d} is the Au binding energy to a vacancy (= -2 eV); n_{d} is the number of vacancies; γ_0 is the surface energy (= 0.3 eV/atom); N is the number of Au atoms; E_{edge} is the edge energy (= 0.6 eV/atom).

tions of Au clusters grown at different temperatures. At low temperature, the growth results in many small clusters, as also seen in Fig. 6.12. Upon heating, or depositing Au at RT, we observe fewer but larger clusters and the cluster size distribution becomes bimodal. The smallest protrusions, i.e. single Au atom-vacancy complexes, can also be observed after deposition up to 300 K, although their relative number decreases with increasing temperatures. When analyzing sequences of STM images we find no evidence for diffusion of single Au atom-vacancy complexes at any investigated temperature. We thus interpret the bimodal size distribution together with the stability of the smallest clusters as a sign of cluster growth through diffusion of clusters above a certain critical size [214]. Clusters nucleate primarily at O vacancy sites, but upon further growth, a single O vacancy can no longer stabilize the cluster, and the cluster-vacancy complex will then diffuse. Whilst diffusing, it can encounter either another cluster (coalescence) or other surface defects. In the former case, a larger cluster is formed that may continue to diffuse as well. If the cluster-vacancy complex encounters other O vacancies it can bind to them and will therefore stabilize on the surface. It is not surprising that larger clusters formed after growth at, or annealing to, RT are found at step edges since the step edges can be considered as a collection of O vacancies.

The bimodal growth model differs from other models proposed to explain Au growth on TiO₂(110) [215, 216]. Parker *et al.* [216] have shown that the onset of 3D growth corresponds to a coverage of 0.086 ML and 0.15 ML on the stoichiometric and the thermally reduced TiO₂(110) surface respectively (1 ML is defined as the packing density of an Au(111) plane, $1.39 \cdot 10^{15}$ atoms·cm⁻²). Based on the present findings, we assume that the 0.064 ML change in transition coverage originates from the presence of O vacancies, and considering a typical vacancy density of 6–7% ML (1 ML is here 1 vacancy/unit cell), we calculate that each vacancy binds ~3 Au atoms, the same number as deduced from Table 6.1.

The critical cluster size for this growth mode can be deduced from the bimodal size distribution at RT in Fig. 6.17. We observe a minimum in the cluster population starting at 250 Å², i.e. clusters containing 5 to 7 atoms. Conversely, clusters containing 3 to 5 atoms are stable. This value correlates nicely with the amount of Au atoms found per vacancy (see Table 6.1).

6.6.3 Conclusion

We demonstrated through a combined STM and DFT study that bridging O vacancies are the active nucleation sites for Au clusters on the rutile TiO₂(110) surface at all investigated temperatures (110–300 K). A single Au atom-vacancy complex is stable up to room temperature and a single O vacancy can bind 3 Au atoms on average. For larger clusters, the Au-substrate interface contains a high density of O vacancies, which enhances the binding of Au particles to the substrate. These pieces of information may be key elements in explaining why Au nano-particles are catalytically active for low-temperature CO oxidation on the TiO₂(110) surface [10, 11]. A new growth model involving coalescence of diffusing Au-vacancy complexes, is shown to explain previous and present observations of the Au/TiO₂(110) system.

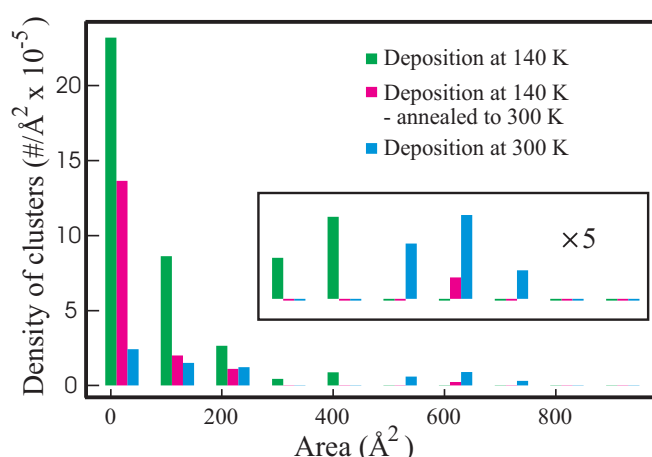


Figure 6.17: Size distributions of Au clusters on TiO₂(110) for different deposition temperatures and annealing. All counts compare the size distribution after 0.02 ML Au. All areas were measured at a threshold level of 1 Å above the medium position of the (110) plane on which the clusters were positioned. Bin sizes of 100 Å² were used.

6.7 Absence of “cannon-ball” effect in Br/TiO₂(110)

In recent years, a subject of lively debate has been so-called “hot” adatoms [217–221]. When a diatomic gas molecule dissociates on a surface, a molecular bond is broken and two new bonds to the surface are formed. If this process is exothermic, energy is released and dissipated. One available dissipation mechanism is coupling to lattice phonons, releasing energy as heat, but an increasing number of experimental data suggests other possible channels for energy release. One or both of the fragments could gain a large amount of kinetic energy, transiently enhancing their lateral motion beyond that of usual thermal diffusivity [217].

The subject of transient mobility is interesting for two main reasons: First, it is of general academic interest to unravel the atomistic fundamental details of the adsorption process and second, transient mobility may also have an impact on other activated processes on surfaces such as reaction and desorption in catalytic processes [217]. In this respect, the concept of “hot” adatoms lies somewhere between the two well-established categories of surface reactions: The Langmuir-Hinselwood mechanism, where thermalized adsorbed species react, and the Eley-Rideal mechanism, where gas molecules impinge on adsorbed atoms or molecules and react directly. The transient energy of atoms would make it possible to overcome reaction barriers that would otherwise be inhibited at a given temperature [222]. The present study of bromine on TiO₂ is, however, mainly of fundamental interest.

If an adsorbed molecule has its axis in an upright position, one could imagine that one or both of the fragments might be “shot” away into a region outside the surface

where the chemisorption potential was less corrugated. This would dramatically diminish the scattering of adsorbate(s) and thereby facilitate a long-range excursion. This effect has been termed the “cannon-ball” mechanism because of the resemblance to classical ballistic motion, and recently it has been proposed by Diebold *et al.* that such a mechanism is indeed responsible for unusually large intra-pair distances observed after dissociative adsorption of chlorine on the TiO₂(110) surface [220]. In this study, Diebold *et al.* observed an average intra-pair distance of 26 Å, and they even found that in a rather large amount of the Cl-pairs, the atoms were separated by protruding O rows. These results indicated that the dissociation fragment(s) had spent an extended period of time in a less corrugated part of the potential, and it was concluded that the findings exemplified the “cannon-ball” mechanism. Diebold *et al.* suggest that the two inequivalent surface species (Ti and O) create an inhomogeneous potential energy surface, and they propose that this is the main reason for the large separation. Accordingly, the previously lacking experimental evidence for long-ranged transient mobility is explained by the fact that only dissociation on metal surfaces with a homogeneous chemisorption potential was considered. The troughs existing on the TiO₂(110) surface would, according to Diebold, cause a *channelling* motion of the “hot” adsorbates and thereby create very large separations, no matter if one of the adsorbates is shot out like a cannon ball or both of them are just moving swiftly in the troughs of the surface.

If the arguments by Diebold *et al.* are correct, we expect a similar effect for the dissociation of other halogens on TiO₂(110). This has led us to test whether the proposed model is a general mechanism for halogens on this surface or if chlorine is just a curiosity.

In the following we will describe experiments aiming at clarifying whether dissociative adsorption of bromine on TiO₂(110) proceeds via a cannon-ball mechanism. In order to reach unambiguous conclusions, the energy barrier for diffusion of bromine on the surface has been estimated. A correlation analysis clearly indicates that the dissociation of bromine proceeds in a very different way than that of chlorine.

6.7.1 Transient motion of bromine

When depositing bromine on the TiO₂(110) surface, large protrusions appear in STM images on top of 5f Ti rows. Figure 6.18a shows a typical STM image after deposition of bromine at room temperature (RT). The large protrusions are assigned to bromine atoms, and this assignment is tested by varying the deposition current and time. It was found that the number of protrusions on the rows scaled linearly with the amount of bromine dosed. Room-temperature experiments do not, however, bring conclusive evidence of whether bromine is dissociated or not, since no clear sign of pairing is seen. When dosing and scanning at low temperatures (<170 K), pairing is however clearly observed (See Fig. 6.18b). This indicates that the large protrusions are indeed associated with single bromine atoms, and in most cases it is even possible to assign atoms to distinct pairs originating from a single dissociation event.

We have observed and analyzed Br diffusion at 256 K where diffusion events occur at a low enough rate to follow the motion of individual atoms. From a detailed analysis,

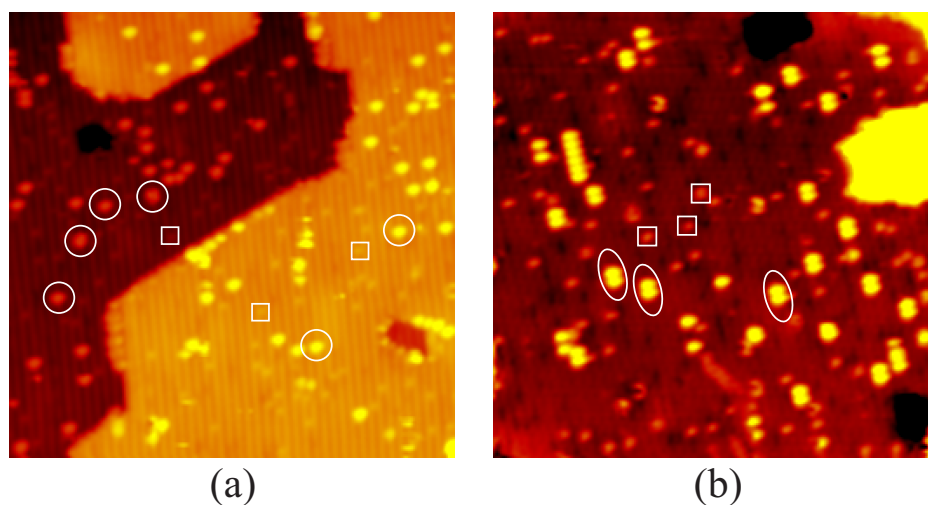


Figure 6.18: (a) STM image ($300 \times 300 \text{ \AA}^2$) of bromine on TiO₂(110) deposited and scanned at room temperature. The image clearly shows protrusions on the bright rows (marked with circles), which are attributed to single bromine atoms. Smaller protrusions on dark rows are the usual O vacancies (marked with squares). (b) STM image ($300 \times 300 \text{ \AA}^2$) of bromine on TiO₂ deposited at 170 K and scanned at 133 K. Pairs of bromine atoms are marked with ellipses. Some impurities are also seen (marked with squares), but they are easily distinguished from the bromine due to a different apparent height.

we extracted a value for the diffusion barrier of

$$E_d = 0.7 \pm 0.1 \text{ eV} \quad (6.1)$$

assuming an Arrhenius dependence and choosing a standard value for the Arrhenius prefactor of $\nu = 10^{12} \text{ s}^{-1}$. The uncertainty is evaluated by varying the prefactor in the Arrhenius by four orders of magnitude around the chosen value. This diffusion barrier is high enough for us to safely say that the expected displacement of the atoms during a experiment performed at temperatures lower than 200 K is orders of magnitudes lower than the relevant distances in the experiment, and it is therefore concluded that diffusion is of no importance when analyzing the transient mobility of bromine atoms.

To quantify any transient motion we performed an autocorrelation analysis of the bromine atoms similar to the procedure in [220]. Figure 6.19 shows the analysis as a 2D plot (a) and as a one-dimensional section along the row (b). The color scale can be read as the (non-normalized) probability of finding a second bromine atom at a certain distance relative to a single bromine atom. A clear peak is seen at 2-3 nearest-neighbor distances *in* the same row, whereas no other peaks are seen. These results are significantly different from the distribution of chlorine atoms in Diebold’s studies. In [220],

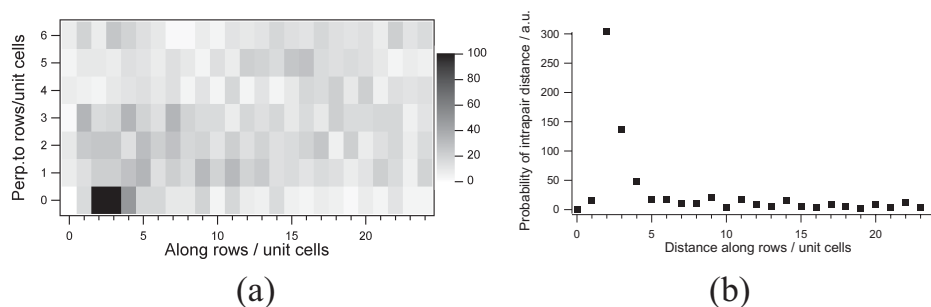


Figure 6.19: (a) Autocorrelation analysis of bromine atoms on TiO₂. The bromine was deposited at 170 K and the STM images were obtained at 110–140 K (b) One-dimensional section of the two-dimensional autocorrelation analysis showing pair correlation along the rows.

clear peaks were found in the same row at 6–9 nearest neighbor (nn) distances and in adjacent rows at 6 nn distances, showing an average separation of the atoms of 26 ± 2 Å.

From our studies we can conclude that the cannon-ball mechanism is *not* a general mechanism for the dissociative adsorption of halogens on TiO₂(110). Our bromine results show no sign of long-range transient motion, but to clarify whether the distribution shown in Figure 6.19 shows any sign of short-range transient motion it is necessary to investigate nearest neighbor and next nearest neighbor interactions. This could be done by observing the distribution of bromine atoms at higher temperatures, where the higher mobility ensures that equilibrium structures are formed.

One may think of different explanations for the discrepancies between the chlorine and the bromine adsorption. Firstly, the chemisorption energy of bromine may be so low that almost no energy could be released for transient motion. Theoretical calculations has been started by B. Hammer and M. D. Rasmussen from University of Aarhus to investigate if this is the case. Secondly, it is possible the interpretation of the data in [220] is wrong. Two arguments for this may be:

- The chlorine diffusion is not completely negligible at the scanning temperature in the experiment (RT). In [220] it is even mentioned that about 10% of the atoms move between consecutive images.
- In a recent combined theoretical and experimental study by Vogtenhuber *et al.*, a considerable amount of the chlorine atoms was found to adsorb in O vacancies. These adsorbates *can* be identified, but in [220] they were not considered [223].

Summarizing, we have shown that the “cannon-ball” mechanism is *not* a general mechanism for the dissociative adsorption of halogens on TiO₂(110). The reason for the divergences between chlorine and bromine adsorption is not yet clearly resolved, but possible causes for the differences between the two experiments have been mentioned.

CHAPTER 7

Summary and outlook

This thesis described three detailed sets of HP-STM experiments where correlations across the pressure gap between surface science and heterogeneous catalysis have been established. Of the three systems (H/Cu(110), CO/Pt(110), and CO/Pt(111)), only the latter does not exhibit adsorbate-induced substrate transformations. As such, this adsorption system is the simpler of the three although a complicated hexagonal adsorbate overlayer was formed. We detected the $(\sqrt{19} \times \sqrt{19})R23.4^\circ$ structure both at high pressure/room temperature and in UHV/low temperatures. It is important to establish this relationship since the CO/Pt(111) system has previously been used as an example of the opposite, i.e. to illustrate the inequivalence between studies of surfaces in catalytic conditions of high pressure and surface science studies carried out in high vacuum [27, 47].

The H/Cu(110) is a classic example of activated adsorption with an activation barrier so high that no H₂ dissociates and adsorbs as H in UHV. Adsorption can however be forced to take place by exposing the Cu(110) surface to atomic H. The substrate then responds by transforming from the bulk-truncated (1×1) structure to a missing-row (1×2) structure. The same structure is found when applying a high pressure of H₂, i.e. when supplying (part of) the incoming molecules with sufficient translational energy to overcome the dissociation barrier. We carried this qualitative correspondence further by locating the pressure range within which the (1×1)→(1×2) transformation starts to take place. From this values for the adsorption and desorption rate constants could be extracted. A quantitative comparison to available UHV data again showed a 1:1 correspondence.

The CO/Pt(110) system transforms in the opposite sense to the previous system, i.e. CO adsorption causes a (1×2)→(1×1) transformation of the formerly bare substrate. From UHV studies it was found that the transformation does not run to completion at

room temperature and we located the temperature range (~ 400 K) necessary to reach thermodynamic equilibrium by comparing our STM results to Monte Carlo simulations based on interaction parameters taken from *ab initio* DFT calculations. High-pressure CO exposure results in the saturation coverage (2×1) -*p2mg*-2CO structure also found in UHV.

We have shown that for the investigated *adsorption systems*, no new concepts need be introduced to explain the structures formed upon high-pressure gas exposure. With respect to the so-called pressure gap we thus conclude that raising the pressure is equivalent to lowering the temperature as long as the thermodynamical equilibrium structure remains kinetically accessible.

In the near future we will put the predictions on the CO/Pt(100) system in Chap. 5 to the test. We expect this system, which is also reconstructed in its clean state, to behave similarly to the CO/Pt(110) system since CO adsorption lifts the hex reconstruction and (1×1) areas are formed upon which CO is expected to form identical ordered overlayers in UHV at low temperature and at high pressures.

In continuation, we presented a study concerning the influence from surface oxygen vacancies on the chemistry of adsorbed water on TiO₂(110). From this study we concluded that the oxygen vacancy site acts as the active dissociation site on the TiO₂(110) surface. To reach this conclusion, we invoked our ability to—supported by *ab initio* STM image simulations—distinguish between oxygen vacancies and hydroxyl groups, which appear almost identical in STM images.

Expanding on this insight, we subsequently presented a study of the nucleation and growth of Au clusters on TiO₂(110). We showed that oxygen vacancies act as the active Au nucleation site and that each vacancy can stabilize three Au atoms on average. A quantitative analysis revealed that this number remains valid for large clusters so that several vacancies become trapped beneath a Au cluster. We hence propose a novel growth model involving vacancy-cluster diffusion, which explains previous and present observations on the Au/TiO₂(110) system.

The next step is to bridge the pressure gap for the Au/TiO₂(110) system as well. Our demonstration of the influence from oxygen vacancies on the nucleation and growth behavior of Au clusters immediately suggests experiments to investigate the stability and sintering behavior of Au clusters under high oxygen pressures. Imaging in high oxygen pressures however introduces the additional complication that a new tip material must be implemented since tungsten reacts readily with oxygen. Work along these lines has however already appeared in the literature [224] but the connection to the influence from oxygen vacancies has not been considered. We expect future high-pressure STM studies to shed new light on this connection.

In a broader perspective, a progression towards conditions more like those employed in real catalytic processes requires new experimental approaches. In our group, we are currently constructing a reaction cell to be connected to the HP-STM cell. With this setup, we will be able to make a direct correlation between the atomic-scale structures observed by HP-STM and their reactivity. The hope is to study reactions at the atomic level, as they occur, much like has been demonstrated under UHV conditions [225, 226]. Furthermore, we will be able to study systems, where a chemical reaction takes place between the surrounding gas and the substrate. New materials will form, which

will no doubt be found to exhibit a different catalytic behavior than the initial material. A prominent example, Ru transforming into RuO₂ under high oxygen pressures, has already been discussed [22,24,227,228]. This situation is outside the realm of the above conclusion, which only concerned adsorption systems. However, the pressure gap has effectively transformed into a materials gap and the real challenge lies in identifying the actual catalytically active material. As the changes in material brought about by the catalytic environment are potentially reversible, it is imperative to study catalytic surfaces *during reaction* to properly characterize their active phase. This necessarily implies a departure from the study of static structures as those described in this thesis. Attempts along these lines have barely been made to date but a few studies using photon-in/photon-out techniques, most notably Sum-Frequency Generation (SFG) [8], or STM [136] have appeared very recently.

Bibliography

- [1] J. H. Sinfelt, "Role of surface science in catalysis," *Surf. Sci.* **500**, 923–946 (2002).
- [2] G. Ertl, "Reactions at well-defined surfaces," *Surf. Sci.* **299/300**, 742–754 (1994).
- [3] *Surface Science: The First Thirty Years*, C. B. Duke, ed., (Elsevier Science, Amsterdam, 1994).
- [4] F. Besenbacher, I. Chorkendorff, B. S. Clausen, B. Hammer, A. M. Molenbroek, J. K. Nørskov, and I. Stensgaard, "Design of a Surface Alloy Catalyst for Steam Reforming," *Science* **279**, 1913–1915 (1998).
- [5] G. A. Somorjai, *Surface Chemistry and Catalysis* (Wiley, New York, 1994).
- [6] P. Stoltze and J. K. Nørskov, "Bridging the "Pressure Gap" between Ultrahigh-Vacuum Surface Physics and High-Pressure Catalysis," *Phys. Rev. Lett.* **55**, 2502–2505 (1985).
- [7] C. V. Ovesen, B. S. Clausen, B. S. Hammershi, G. Steffensen, T. Askgaard, I. Chorkendorff, J. K. Nørskov, P. B. Rasmussen, P. Stoltze, and P. Taylor, "A Microkinetic Analysis of the Water-Gas Shift Reaction under Industrial Conditions," *J. Catal.* **158**, 170–180 (1996).
- [8] H.-J. Freund, H. Kuhlenbeck, J. Libuda, G. Rupprechter, M. Bäumer, and H. Hamann, "Bridging the pressure and materials gaps between catalysis and surface science: clean and modified oxide surfaces," *Topics Catal.* **15**, 201–209 (2001).
- [9] M. Mavrikakis, P. Stoltze, and J. K. Nørskov, "Making gold less noble," *Catal. Lett.* **64**, 101–106 (2000).
- [10] M. Haruta, N. Yamada, T. Kobayashi, and S. Iijima, "Gold Catalysts Prepared by Coprecipitation for Low-Temperature Oxidation of Hydrogen and of Carbon Monoxide," *J. Catal.* **115**, 301 (1989).
- [11] M. Valden, X. Lai, and D. W. Goodman, "Onset of Catalytic Activity of Gold Clusters on Titania with the Appearance of Nonmetallic Properties," *Science* **281**, 1647–1650 (1998).
- [12] A. Sanchez, S. Abbet, U. Heiz, W.-D. Schneider, H. Häkkinen, R. N. Barnett, and U. Landman, "When Gold Is Not Noble: Nanoscale Gold Catalysts," *J. Phys. Chem. A* **103**, 9573–9578 (1999).
- [13] R. J. Farrauto and R. M. Heck, "Catalytic converters: state of the art and perspectives," *Catal. Today* **51**, 351–360 (1999).
- [14] C. T. Campbell, "Ultrathin metal films and particles on oxide surfaces: Structural, electronic and chemisorptive properties," *Surf. Sci. Rep.* **27**, 3–111 (1997).
- [15] C. R. Henry, "Surface studies of supported model catalysts," *Surf. Sci.* **31**, 235–325 (1998).
- [16] M. Bäumer and H.-J. Freund, "Metal deposits on well-ordered oxide films," *Prog. Surf. Sci.* **61**, 127–198 (1999).
- [17] K. H. Hansen, T. Worren, S. Stempel, E. Lægsgaard, M. Bäumer, H.-J. Freund, F. Besenbacher, and I. Stensgaard, "Palladium Nanocrystals on Al₂O₃: Structure and Adhesion Energy," *Phys. Rev. Lett.* **83**, 4120–4123 (1999).

- [18] J.-D. Grunwaldt, A. M. Molenbroek, N.-Y. Topsøe, H. Topsøe, and B. S. Clausen, "In Situ Investigations of Structural Changes in Cu/ZnO Catalysts," *J. Catal.* **194**, 452–460 (2000).
- [19] P. L. Hansen, J. B. Wagner, S. Helveg, J. R. Rostrup-Nielsen, B. S. Clausen, and H. Topsøe, "Atom-Resolved Imaging of Dynamic Shape Changes in Supported Copper Nanocrystals," *Science* **295**, 2053–2055 (2002).
- [20] E. Christoffersen, P. Liu, A. Ruban, H. L. Skriver, and J. K. Nørskov, "Anode Materials for Low-Temperature Fuel Cells: A Density Functional Theory Study," *J. Catal.* **199**, 123–131 (2001).
- [21] E. Christoffersen, "Adsorption-induced segregation and step formation: a simulation study", PhD thesis, Technical University of Denmark, 2001.
- [22] H. Over, Y. D. Kim, A. P. Seitsonen, S. Wendt, E. Lundgren, M. Schmid, P. Varga, A. Morgante, and G. Ertl, "Atomic-Scale Structure and Catalytic Reactivity of the RuO₂(110) Surface," *Science* **287**, 1474–1476 (2000).
- [23] K. Reuter and M. Scheffler, "Composition, structure, and stability of RuO₂(110) as a function of oxygen pressure," *Phys. Rev. B* **65**, 035406 (2002).
- [24] C. Stampfl, M. V. Ganduglia-Pirovano, K. Reuter, and M. Scheffler, "Catalysis and corrosion: the theoretical surface-science context," *Surf. Sci.* **500**, 368–394 (2002).
- [25] B. J. McIntyre, M. Salmeron, and G. A. Somorjai, "In situ scanning tunneling microscopy study of platinum (110) in a reactor cell at high pressures and temperatures," *J. Vac. Sci. Technol. A* **11**, 1964–1968 (1993).
- [26] X. Su, P. S. Cremer, Y. R. Shen, and G. A. Somorjai, "Pressure Dependence (10⁻¹⁰–700 Torr) of the Vibrational Spectra of Adsorbed CO on Pt(111) Studied by Sum Frequency Generation," *Phys. Rev. Lett.* **77**, 3858–3860 (1996).
- [27] J. A. Jensen, K. B. Rider, M. Salmeron, and G. A. Somorjai, "High Pressure Adsorbate Structures Studied by Scanning Tunneling Microscopy: CO on Pt(111) in Equilibrium with the Gas Phase," *Phys. Rev. Lett.* **80**, 1228–1231 (1998).
- [28] D. W. Goodman, "Correlations between Surface Science Models and "Real-World" Catalysts," *J. Phys. Chem.* **100**, 13090–13102 (1996).
- [29] L. Österlund, P. B. Rasmussen, P. Thosttrup, E. Lægsgaard, I. Stensgaard, and F. Besenbacher, "Bridging the Pressure Gap in Surface Science at the Atomic Level: H/Cu(110)," *Phys. Rev. Lett.* **86**, 460–463 (2001).
- [30] T. Gritsch, D. Coulman, R. J. Behm, and G. Ertl, "Mechanism of the CO-induced 1×2 → 1×1 Structural Transformation of Pt(110)," *Phys. Rev. Lett.* **63**, 1086–1089 (1989).
- [31] R. Feidenhans'l, F. Grey, M. Nielsen, F. Besenbacher, F. Jensen, E. Lægsgaard, I. Stensgaard, K. W. Jacobsen, J. K. Nørskov, and R. L. Johnson, "Oxygen chemisorption on Cu(110): A model for the c(6×2) structure," *Phys. Rev. Lett.* **65**, 2027–2030 (1990).
- [32] F. Besenbacher and J. K. Nørskov, "Oxygen chemisorption on metal surfaces: general trends for Cu, Ni and Ag," *Prog. Surf. Sci.* **44**, 5–66 (1993).
- [33] L. P. Nielsen, F. Besenbacher, I. Stensgaard, E. Lægsgaard, C. Engdahl, P. Stoltze, and J. K. Nørskov, "'Dealloying' Phase Separation during Growth of Au on Ni(110)," *Phys. Rev. Lett.* **74**, 1159–1162 (1995).
- [34] S. Dahl, A. Logadottir, R. C. Egeberg, J. H. Larsen, I. Chorkendorff, E. Törnquist, and J. K. Nørskov, "Role of Steps in N₂ Activation on Ru(0001)," *Phys. Rev. Lett.* **83**, 1814–1817 (1999).
- [35] U. Diebold, "The Structure of TiO₂ surfaces," in *Oxide Surfaces*, Vol. 9 of *The Chemical Physics of Solid Surfaces*, D. P. Woodruff, ed., (Elsevier Science, Amsterdam, 2001), pp. 443–484.
- [36] M. V. Bollinger, J. V. Lauritsen, K. W. Jacobsen, J. K. Nørskov, S. Helveg, and F. Besenbacher, "One-Dimensional Metallic Edge States in MoS₂," *Phys. Rev. Lett.* **87**, 196803 (2001).
- [37] L. C. Feldman and J. W. Mayer, *Fundamentals of Surface and Thin Film Analysis* (Elsevier Science Publishing, New York, 1986).

- [38] D. P. Woodruff and T. A. Delchar, *Modern Techniques of Surface Science, Cambridge Solid State Science Series*, 2nd ed. (Cambridge University Press, Cambridge, 1994).
- [39] K. Y. Kung, P. Chen, F. Wei, G. Rupprechter, Y. R. Shen, and G. A. Somorjai, "Ultrahigh vacuum high-pressure reaction system for 2-infrared 1-visible sum frequency studies," *Rev. Sci. Instrum.* **72**, 1806–1809 (2001).
- [40] G. Rupprechter, T. Dellwig, H. Unterhalt, and H.-J. Freund, "High-Pressure Carbon Monoxide Adsorption on Pt(111) Revisited: A Sum Frequency Generation Study," *J. Phys. Chem. B* **105**, 3797–3802 (2001).
- [41] T. W. Hansen, J. B. Wagner, P. L. Hansen, S. Dahl, H. Topsøe, and C. J. H. Jacobsen, "Atomic-Resolution in Situ Transmission Electron Microscopy of a Promoter of a Heterogenous Catalyst," *Science* **294**, 1508–1510 (2001).
- [42] B. S. Clausen, J. Schiøtz, L. Gråbæk, C. V. Ovesen, K. W. Jacobsen, J. K. Nørskov, and H. Topsøe, "Wetting/non-wetting phenomena during catalysis: evidence from in situ on-line EXAFS studies of Cu-based catalysts," *Topics Catal.* **1**, 367–376 (1994).
- [43] E. Lægsgaard, F. Besenbacher, K. Mortensen, and I. Stensgaard, "A fully automated, 'thimble-size' scanning tunnelling microscope," *J. Microscop.* **152**, 663–669 (1988).
- [44] M. Ø. Pedersen, "Scanning Tunneling Microscopy Studies of Growth and Adsorption on Transition Metal Surfaces", PhD thesis, University of Aarhus, 1998.
- [45] F. Besenbacher, F. Jensen, E. Lægsgaard, K. Mortensen, and I. Stensgaard, "Visualization of the dynamics in surface reconstructions," *J. Vac. Sci. Technol. B* **9**, 874–878 (1991).
- [46] J. A. Jensen, K. B. Rider, Y. Chen, M. Salmeron, and G. A. Somorjai, "High pressure, high temperature scanning tunneling microscopy," *J. Vac. Sci. Technol. B* **17**, 1080–1084 (1999).
- [47] G. A. Somorjai, X. Su, K. R. McCrea, and K. B. Rider, "Molecular surface studies of adsorption and catalytic reaction on crystal (Pt, Rh) surfaces under high pressure conditions (atmospheres) using sum frequency generation (SFG) - surface vibrational spectroscopy and scanning tunneling microscopy (STM)," *Topics Catal.* **8**, 23–34 (1999).
- [48] J. V. Barth, H. Brune, G. Ertl, and R. J. Behm, "Scanning tunneling microscopy observations on the reconstructed Au(111) surface: Atomic structure, long-range superstructure, rotational domains, and surface defects," *Phys. Rev. B* **42**, 9307–9318 (1990).
- [49] J. V. Barth, R. J. Behm, and G. Ertl, "Mesoscopic structural transformations of the Au(111) surface induced by alkali metal adsorption," *Surf. Sci.* **302**, L319–L324 (1994).
- [50] P. Hohenberg and W. Kohn, "Inhomogeneous Electron Gas," *Phys. Rev.* **136**, B864–B871 (1964).
- [51] W. Kohn, "Nobel Lecture: Electronic structure of matter — wave functions and density functionals," *Review of Modern Physics* **71**, 1253–1266 (1999).
- [52] W. Kohn and L. J. Sham, "Self-Consistent Equations Including Exchange and Correlation Effects," *Phys. Rev.* **140**, A1133–A1138 (1965).
- [53] J. P. Perdew, "Unified theory of exchange and correlation beyond the local density approximation," In *Electronic Structure of Solids '91*, P. Ziesche and H. Eschrig, eds., *Physical Research* **17**, 11–20 (Akademie Verlag, Berlin, 1991).
- [54] J. P. Perdew, K. Burke, and M. Ernzerhof, "Generalized Gradient Approximation Made Simple," *Phys. Rev. Lett.* **77**, 3865–3868 (1996).
- [55] Y. Zhang and W. Yang, "Comment on 'Generalized Gradient Approximation Made Simple'," *Phys. Rev. Lett.* **80**, 890–891 (1998).
- [56] B. Hammer, L. B. Hansen, and J. K. Nørskov, "Improved adsorption energetics within density-functional theory using revised Perdew-Burke-Ernzerhof functionals," *Phys. Rev. B* **59**, 7413–7421 (1999).
- [57] G. Binnig, H. Rohrer, C. Gerber, and E. Weibel, "Surface Studies by Scanning Tunneling Microscopy," *Phys. Rev. Lett.* **49**, 57–61 (1982).

- [58] J. Tersoff and D. R. Hamann, "Theory and Application for the Scanning Tunneling Microscope," *Phys. Rev. Lett.* **50**, 1998–2001 (1983).
- [59] J. Tersoff and D. R. Hamann, "Theory of the scanning tunneling microscope," *Phys. Rev. B* **31**, 805–813 (1985).
- [60] J. Bardeen, "Tunneling from a Many-Particle Point of View," *Phys. Rev. Lett.* **6**, 57–59 (1961).
- [61] P. Sautet and C. Joachim, "Electronic transmission coefficient for the single-impurity problem in the scattering-matrix approach," *Phys. Rev. B* **38**, 12238–12247 (1988).
- [62] P. Sautet, "Images of Adsorbates with the Scanning Tunneling Microscope: Theoretical Approaches to the Contrast Mechanism," *Chem. Rev.* **97**, 1097–1116 (1997).
- [63] M. Ø. Pedersen, M.-L. Bocquet, P. Sautet, E. Lægsgaard, I. Stensgaard, and F. Besenbacher, "CO on Pt(111): binding site assignment from the interplay between measured and calculated STM images," *Chem. Phys. Lett.* **299**, 403–409 (1999).
- [64] F. Rosei, M. Schunack, P. Jiang, A. Gourdon, E. Lægsgaard, I. Stensgaard, C. Joachim, and F. Besenbacher, "Organic Molecules Acting as Templates on Metal Surfaces," *Science* **296**, 328–331 (2002).
- [65] W. Sacks and C. Noguera, "Generalized expression for the tunneling current in scanning tunneling microscopy," *Phys. Rev. B* **43**, 11612–11622 (1991).
- [66] B. Hammer, Y. Morikawa, and J. K. Nørskov, "CO Chemisorption at Metal Surfaces and Overlayers," *Phys. Rev. Lett.* **76**, 2141–2144 (1996).
- [67] B. Hammer and J. K. Nørskov, "Theory of adsorption and surface reactions," in *Chemisorption and Reactivity on Supported Clusters and Thin Films*, Vol. 331 of *NATO ASI Series E*, R. M. Lambert and G. Pacchioni, eds., (Kluwer Academic Publishers, Dordrecht, 1997), pp. 285–351.
- [68] B. Hammer and J. K. Nørskov, "Theoretical Surface Science and Catalysis—Calculation and Concepts," *Adv. Catal.* **45**, 71–130 (2000).
- [69] G. Blyholder, "Molecular Orbital View of Chemisorbed Carbon Monoxide," *J. Phys. Chem.* **68**, 2772–2778 (1964).
- [70] B. Hammer, O. H. Nielsen, and J. K. Nørskov, "Structure sensitivity in adsorption: CO interaction with stepped and reconstructed Pt surfaces," *Catal. Lett.* **46**, 31–35 (1997).
- [71] D. P. Landau and K. Binder, *A Guide to Monte Carlo Simulations in Statistical Physics* (Cambridge University Press, Cambridge, 2000).
- [72] G. Anger, A. Winkler, and K. D. Rendulic, "Adsorption and desorption kinetics in the systems H₂/Cu(111), H₂/Cu(110) and H₂/Cu(100)," *Surf. Sci.* **220**, 1–17 (1989).
- [73] J. M. Campbell and C. T. Campbell, "The dissociative adsorption of H₂ and D₂ on Cu(110): activation barriers and dynamics," *Surf. Sci.* **259**, 1–17 (1991).
- [74] J. M. Campbell, M. E. Domagala, and C. T. Campbell, "Energy requirements for the dissociative adsorption of hydrogen on Cu(110)," *J. Vac. Sci. Technol. A* **9**, 1693–1697 (1991).
- [75] C. T. Rettner, D. J. Auerbach, J. C. Tully, and A. W. Kleyn, "Chemical Dynamics at the Gas-Surface Interface," *J. Phys. Chem. B* **100**, 13021–13033 (1996).
- [76] P. B. Rasmussen, P. M. Holmblad, T. Askgaard, C. V. Ovesen, P. Stoltze, J. K. Nørskov, and I. Chorkendorff, "Methanol synthesis on Cu(100) from a binary gas mixture of CO₂ and H₂," *Catal. Lett.* **26**, 373–381 (1994).
- [77] C. T. Campbell and K.-H. Ernst, "Forward and Reverse Water-Gas Shift Reactions on Model Copper Catalysts," in *Surface Science of Catalysis*, Vol. 482 of *ACS Symposium Series*, D. J. Dwyer and F. M. Hoffmann, eds., (American Chemical Society, Washington DC, 1992), pp. 130–142.
- [78] K.-H. Ernst, C. T. Campbell, and G. Moretti, "Kinetics of the Reverse Water-Gas Shift Reaction over Cu(110)," *J. Catal.* **134**, 66–74 (1992).
- [79] K.-H. Rieder and W. Stocker, "Hydrogen-Induced Subsurface Reconstruction of Cu(110)," *Phys. Rev. Lett.* **57**, 2548–2551 (1986).

- [80] B. E. Hayden, D. Lackey, and J. Schott, "A vibrational study of the hydrogen induced reconstruction on Cu(110)," *Surf. Sci.* **239**, 119–126 (1990).
- [81] R. Spitzl, H. Niehus, B. Poelsema, and G. Comsa, "H-induced (1×2) reconstruction of the Cu(110) surface: structure and deconstruction kinetics," *Surf. Sci.* **239**, 243–253 (1990).
- [82] J. Goerge, P. Zeppenfeld, R. David, M. Büchel, and G. Comsa, "Structure of the hydrogen covered Cu(110) surface studied with thermal energy helium scattering," *Surf. Sci.* **289**, 201–213 (1993).
- [83] F. Besenbacher, P. T. Sprunger, L. Ruan, L. Olesen, I. Stensgaard, and E. Lægsgaard, "Direct observation of changes in surface structures by scanning tunneling microscopy," *Topics Catal.* **1**, 325–341 (1994).
- [84] U. Bischler, P. Sandl, E. Bertel, T. Brunner, and W. Brenig, "Sticking, Adsorption, and Absorption of Atomic H on Cu(110)," *Phys. Rev. Lett.* **70**, 3603–3606 (1993).
- [85] W. R. Wampler, T. Schober, and B. Lengeler, "Precipitation and trapping of hydrogen in copper," *Philos. Mag.* **34**, 129–141 (1976).
- [86] R. Feidenhans'l and I. Stensgaard, "Oxygen-adsorption induced reconstruction of Cu(110) studied by high energy ion scattering," *Surf. Sci.* **133**, 453–468 (1983).
- [87] A. P. Baddorf and J. F. Wendelken, "High coverages of oxygen on Cu(110) investigated with XPS, LEED, and HREELS," *Surf. Sci.* **256**, 264–271 (1991).
- [88] L. Carrette, K. A. Friedrich, and U. Stimming, "Fuel Cells - Fundamentals and Applications," *Fuel Cells* **1**, 5–39 (2001).
- [89] P. Hofmann, S. R. Bare, and D. R. King, "Surface phase transitions in CO chemisorption on Pt{110}," *Surf. Sci.* **117**, 245–256 (1982).
- [90] D. Rieger, R. D. Schnell, and W. Steinmann, "Angular distribution patterns of photoelectrons from orbitals of CO adsorbed on Ni(100), Pt(111) and Pt(110)," *Surf. Sci.* **143**, 157–176 (1984).
- [91] J. C. Campuzano, "The Adsorption of Carbon Monoxide by the Transition Metals," in *Chemisorption Systems, Part A*, Vol. 3 of *The Chemical Physics of Solid Surfaces and Heterogeneous Catalysis*, D. A. King and D. P. Woodruff, eds., (Elsevier Science, Amsterdam, 1990), pp. 389–469.
- [92] I. Villegas and M. J. Weaver, "Carbon monoxide adlayer structures on platinum (111) electrodes: A synergy between *in situ* scanning tunneling microscopy and infrared spectroscopy," *J. Chem. Phys.* **101**, 1648–1660 (1994).
- [93] P. Cernota, K. Rider, H. A. Yoon, M. Salmeron, and G. A. Somorjai, "Dense structures formed by CO on Rh(111) studied by scanning tunneling microscopy," *Surf. Sci.* **445**, 249–255 (2000).
- [94] H. Steininger, S. Lehwald, and H. Ibach, "On the adsorption of CO on Pt(111)," *Surf. Sci.* **123**, 264–282 (1982).
- [95] G. Ertl, M. Neumann, and K. M. Streit, "Chemisorption of CO on the Pt(111) surface," *Surf. Sci.* **64**, 393–410 (1977).
- [96] I. K. Robinson, E. Vlieg, and K. Kern, "Non-Ising Behavior of the Pt(110) Surface Phase Transition," *Phys. Rev. Lett.* **63**, 2578–2581 (1989).
- [97] V. P. Zhdanov, "The effect of adsorbate-induced changes in the surface on thermal desorption," *Surf. Sci.* **257**, 344–352 (1991).
- [98] A. V. Myshlyavtsev and V. P. Zhdanov, "Surface Reconstruction and Thermal Desorption: The Missing-Row Model for CO/Pt(110)," *Langmuir* **9**, 1290–1298 (1993).
- [99] Q. Ge and D. A. King, "Surface diffusion potential energy surfaces from first principles: CO chemisorbed on Pt{110}," *J. Chem. Phys.* **111**, 9461–9464 (1999).
- [100] P. Thostrup, E. Christoffersen, H. T. Lorensen, K. W. Jacobsen, F. Besenbacher, and J. K. Nørskov, "Adsorption-Induced Step Formation," *Phys. Rev. Lett.* **87**, 126102 (2001).
- [101] R. M. Lambert, "On the interpretation of LEED patterns due to CO adsorption on the (110) faces of Ni, Pd, Pt, and Ir," *Surf. Sci.* **49**, 325–329 (1975).

- [102] C. M. Comrie and R. M. Lambert, "Chemisorption and Surface Structural Chemistry of Carbon Monoxide on Pt(110)," *J. Chem. Soc., Faraday Trans.* **72**, 1659–1669 (1976).
- [103] S. Ferrer and H. P. Bonzel, "The preparation, thermal stability and adsorption characteristics of the non-reconstructed Pt(110)- 1×1 surface," *Surf. Sci.* **119**, 234–250 (1982).
- [104] T. E. Jackman, J. A. Davies, D. P. Jackson, W. N. Unertl, and P. R. Norton, "The Pt(110) phase transitions: A study by Rutherford backscattering, nuclear microanalysis, LEED and thermal desorption spectroscopy," *Surf. Sci.* **120**, 389–412 (1982).
- [105] N. Freyer, M. Kiskinova, G. Pirug, and H. P. Bonzel, "Site-Specific Core Level Spectroscopy of CO and NO Adsorption on Pt(110)(1×2) and (1×1) Surfaces," *Appl. Phys. A* **39**, 209–219 (1986).
- [106] B. E. Hayden, A. W. Robinson, and P. M. Tucker, "IR evidence for the molecular reorientation of linear CO on Pt(110)-(1×2)," *Surf. Sci.* **192**, 163–171 (1987).
- [107] R. Imbühl, S. Ladas, and G. Ertl, "The CO-induced $1 \times 2 \leftrightarrow 1 \times 1$ phase transition of Pt(110) studied by LEED and work function measurements," *Surf. Sci.* **206**, L903–L912 (1988).
- [108] S. R. Bare, K. Griffiths, P. Hofmann, D. A. King, G. L. Nyberg, and N. V. Richardson, "A synchrotron radiation study of the electronic and geometric structure of CO on Pt(110)," *Surf. Sci.* **120**, 367–375 (1982).
- [109] P. Hofmann, S. R. Bare, and D. A. King, "characterisation of a Low Temperature Surface Phase of CO on Pt{110}," *Phys. Scr.* **T4**, 118–121 (1983).
- [110] S. R. Bare, P. Hofmann, and D. A. King, "Vibrational studies of the surface phases of CO on Pt{110} at 300 K," *Surf. Sci.* **144**, 347–399 (1984).
- [111] C. Klünker, M. Balden, S. Lehwald, and W. Daum, "CO stretching vibrations on Pt(111) and Pt(110) studied by sum-frequency generation," *Surf. Sci.* **360**, 104–111 (1996).
- [112] P. Hofmann, S. R. Bare, and D. R. King, "Orientation of the chemisorbed species from orthogonal-plane ARUPS: Tilted CO on Pt{110} and upright CO on Pt{111}," *Solid State Commun.* **42**, 645–651 (1982).
- [113] T. E. Jackman, J. A. Davies, D. P. Jackson, P. R. Norton, and W. N. Unertl, "A new surface phase for CO-covered Pt(110)," *J. Phys. C* **15**, L99–L104 (1982).
- [114] R. K. Sharma, W. A. Brown, and D. A. King, "Adsorbed CO chain condensation and evaporation on Pt{110}-(1×2) at 30–70 K studied by RAIRS," *Chem. Phys. Lett.* **291**, 1–6 (1998).
- [115] R. K. Sharma, W. A. Brown, and D. A. King, "The adsorption of CO on Pt{110} over the temperature range from 90 to 300 K studied by RAIRS," *Surf. Sci.* **414**, 68–76 (1998).
- [116] T. Gritsch, D. Coulman, R. J. Behm, and G. Ertl, "A Scanning Tunneling Microscopy Investigation of the $1 \times 2 \rightleftharpoons 1 \times 1$ Structural Transformation of the Pt(110) Surface," *Appl. Phys. A* **49**, 403–406 (1989).
- [117] J. Winterlin and R. J. Behm, "Adsorbate Covered Metal Surfaces and Reactions on Metal Surfaces," in *Scanning Tunneling Microscopy I*, Vol. 20 of *Springer Series in Surface Sciences*, 2 ed., H.-J. Güntherodt and R. Wiesendanger, eds., (Springer-Verlag, New York, 1994), pp. 39–82.
- [118] E. Bertel, N. Memmel, G. Rangelov, and U. Bischler, "Compressed CO adsorption layers on the (110) surfaces of Ni, Pd, and Pt. An inverse photoemission study of the unoccupied electronic band structure," *Chem. Phys.* **177**, 337–348 (1993).
- [119] S. Schwegmann, W. Tappe, and U. Korte, "Quantitative structure analysis of a disordered system: RHEED study of the CO induced (1×2) \rightarrow (1×1) structure transition of Pt(110)," *Surf. Sci.* **334**, 55–76 (1995).
- [120] C. E. Wartnaby, A. Stuck, Y. Y. Yeo, and D. A. King, "Microcalorimetric Heats of Adsorption for CO, NO, and Oxygen on Pt{110}," *J. Phys. Chem. B* **100**, 12483–12488 (1996).
- [121] P. Fery, W. Moritz, and D. Wolf, "Structure determination of the (1×2) and (1×3) reconstructions of Pt(110) by low-energy electron diffraction," *Phys. Rev. B* **38**, 7275–7286 (1988).
- [122] T. Gritsch, D. Coulman, R. J. Behm, and G. Ertl, "A scanning tunneling microscopy investigation of the structure of the Pt(110) and Au(110) surfaces," *Surf. Sci.* **257**, 297–306 (1991).

- [123] K.-D. Shiang and T. T. Tsong, "Energetics and atomic steps in the reconstruction of the Pt(110) surface," *Phys. Rev. B* **51**, 5522–5525 (1995).
- [124] P. Sprunger, F. Besenbacher, and I. Stensgaard, "STM study of the Ni(110)-(2×1)-2CO system: Structure and bonding-site determination," *Surf. Sci.* **324**, L321–L327 (1995).
- [125] F. Besenbacher, "Scanning tunnelling microscopy studies of metal surfaces," *Rep. Prog. Phys.* **59**, 1737–1802 (1996).
- [126] P. J. Feibelman, B. Hammer, J. K. Nørskov, F. Wagner, M. Scheffler, R. Stumpf, R. Watwe, and J. Dumesic, "The CO/Pt(111) Puzzle," *J. Phys. Chem. B* **105**, 4018–4025 (2001).
- [127] J. P. Perdew, J. A. Chevary, S. H. Vosko, K. A. Jackson, M. R. Pederson, and D. J. Singh, "Atoms, molecules, solids, and surfaces: Applications of the generalized gradient approximation for exchange and correlation," *Phys. Rev. B* **46**, 6671–6687 (1992).
- [128] H. T. Lorenzen, J. K. Nørskov, and K. W. Jacobsen, "Mechanisms of self-diffusion on Pt(110)," *Phys. Rev. B* **60**, R5149–R5152 (1999).
- [129] P. J. Feibelman, "Ordering of self-diffusion barrier energies on Pt(110)-(1×2)," *Phys. Rev. B* **61**, R2452–R2455 (2000).
- [130] K.-M. Ho and K. P. Bohnen, "Stability of the missing-row reconstruction on fcc (110) transition-metal surfaces," *Phys. Rev. Lett.* **59**, 1833–1836 (1987).
- [131] L. Vitos, A. V. Ruban, H. L. Skriver, and J. Kollár, "The surface energy of metals," *Surf. Sci.* **411**, 186–202 (1998).
- [132] P. Hanesch and E. Bertel, "Mesoscopic Self-Organisation Induced by Intrinsic Surface Stress on Pt(110)," *Phys. Rev. Lett.* **79**, 1523–1526 (1997).
- [133] K. Swamy, E. Bertel, and I. Vilfan, "Step interaction and relaxation at steps: Pt(110)," *Surf. Sci.* **425**, L369–L375 (1999).
- [134] B. Hammer and J. K. Nørskov, "Adsorbate Reorganization at Steps: NO on Pd(211)," *Phys. Rev. Lett.* **79**, 4441–4444 (1997).
- [135] B. Hammer, "The NO + CO Reaction Catalyzed by Flat, Stepped, and Edged Pd Surfaces," *J. Catal.* **199**, 171–176 (2001).
- [136] B. L. M. Hendriksen and J. W. M. Frenken, "CO Oxidation on Pt(110): Scanning Tunneling Microscopy Inside a High-Pressure Flow Reactor," *Phys. Rev. Lett.* **89**, 046101 (2002).
- [137] T. R. Linderoth, J. J. Mortensen, K. W. Jacobsen, E. Lægsgaard, I. Stensgaard, and F. Besenbacher, "Homoepitaxial Growth of Pt on Pt(100)-hex: Effects of Strongly Anisotropic Diffusion and Finite Island Sizes," *Phys. Rev. Lett.* **77**, 87–90 (1996).
- [138] T. R. Linderoth, "Diffusion, Nucleation and Growth of Pt on Pt surfaces Studied by Scanning Tunneling Microscopy", PhD thesis, Aarhus, 1997.
- [139] A. Borg, A.-M. Hilmen, and E. Bergene, "STM studies of clean, CO- and O₂-exposed Pt(100)-hex-R0.7°," *Surf. Sci.* **306**, 10–20 (1994).
- [140] R. J. Behm, P. A. Thiel, P. R. Norton, and G. Ertl, "The interaction of CO and Pt(100). I. Mechanism of adsorption and Pt phase transition," *J. Chem. Phys.* **78**, 7437–7447 (1983).
- [141] G. Brodén, G. Pirug, and H. P. Bonzel, "Chemisorption of CO on the unreconstructed Pt(100) surface," *Surf. Sci.* **72**, 45–52 (1978).
- [142] T. R. Linderoth (private communication).
- [143] A. Hopkinson and D. A. King, "Surface restructuring dynamics in CO adsorption, desorption, and reaction with NO on Pt{100}," *Chem. Phys.* **177**, 433–452 (1993).
- [144] A. Hopkinson and D. A. King, "Modelling the CO-induced Surface Phase Transition on Pt{100}: Implications for Kinetic Oscillations," *Faraday Discuss.* **96**, 255–264 (1993).
- [145] A. Fujishima and K. Honda, "Electrochemical Photolysis of Water at a Semiconductor Electrode," *Nature* **238**, 37–38 (1972).

- [146] A. Linsebigler, G. Lu, and J. T. J. Yates, "Photocatalysis on TiO₂ Surfaces: Principles, Mechanisms, and Selected Results," *Chem. Rev.* **95**, 735–758 (1995).
- [147] C. Barth and M. Reichling, "Imaging the atomic arrangements on the high-temperature reconstructed α -Al₂O₃(0001) surface," *Nature* **414**, 54–57 (2001).
- [148] V. E. Henrich, "Metal oxide surfaces and interfaces: concepts and issues," in *Oxide Surfaces*, Vol. 9 of *The Chemical Physics of Solid Surfaces*, D. P. Woodruff, ed., (Elsevier Science, Amsterdam, 2001), pp. 1–34.
- [149] H. Over, A. P. Seitsonen, E. Lundgren, M. Schmid, and P. Varga, "Direct Imaging of Catalytically Important Processes in the Oxidation of CO over RuO₂(110)," *J. Am. Chem. Soc.* **123**, 11807–11808 (2001).
- [150] A. Fujishima, T. N. Rao, and A. D. Tryk, "Titanium dioxide photocatalysis," *Journal of Photochemistry and Photobiology C: Photochemistry Reviews* **1**, 1–21 (2000).
- [151] B. Kasemo and J. Gold, "Implant Surfaces and Interface Processes," *Adv. Dent. Res.* **13**, 8–20 (1999).
- [152] A. Heller, "Chemistry and Applications of Photocatalytic Oxidation of Thin Organic Films," *Acc. Chem. Res.* **28**, 503–508 (1995).
- [153] P. M. Oliver, G. W. Watson, E. T. Kelsey, and S. C. Parker, "Atomistic simulation of the surface structure of the TiO₂ polymorphs rutile and anatase," *J. Mat. Chem.* **7**, 563–568 (1997).
- [154] W. Hebenstreit, N. Ruzycski, G. S. Herman, Y. Gao, and U. Diebold, "Scanning tunneling microscopy investigation of the TiO₂ anatase (101) surface," *Phys. Rev. B* **62**, R16334–R16336 (2000).
- [155] R. Hengerer, B. Bolliger, M. Erbudak, and M. Grätzel, "Structure and stability of the anatase TiO₂ (101) and (001) surfaces," *Surf. Sci.* **460**, 162–169 (2000).
- [156] A. Belrán, J. R. Sambrano, M. Calatayud, F. R. Sensato, and J. Andrés, "Static simulation of bulk and selected surfaces of anatase TiO₂," *Surf. Sci.* **490**, 116–124 (2001).
- [157] M. Lazzeri, A. Vittadini, and A. Selloni, "Structure and energetics of stoichiometric TiO₂ anatase surfaces," *Phys. Rev. B* **63**, 155409 (2001).
- [158] A. Hagfeldt and M. Graetzel, "Light-Induced Redox Reactions in Nanocrystalline Systems," *Chem. Rev.* **95**, 49–68 (1995).
- [159] M. B. Hugenschmidt, L. Gamble, and C. T. Campbell, "The interaction of H₂O with a TiO₂(110) surface," *Surf. Sci.* **302**, 329–340 (1994).
- [160] M. A. Henderson, "An HREELS and TPD study of water on TiO₂(110): The extent of molecular versus dissociative adsorption," *Surf. Sci.* **355**, 151–166 (1996).
- [161] D. Brinkley, M. Dietrich, T. Engel, P. Farrall, G. Gantner, A. Schafer, and A. Szuchmacher, "A modulated molecular beam study of the extent of H₂O dissociation on TiO₂(110)," *Surf. Sci.* **395**, 292–306 (1998).
- [162] M. A. Henderson, "A surface perspective on self-diffusion in rutile TiO₂," *Surf. Sci.* **419**, 174–187 (1999).
- [163] M. Li, W. Hebenstreit, U. Diebold, A. M. Tyryshkin, M. K. Bowman, G. G. Dunham, and M. A. Henderson, "The Influence of the Bulk Reduction State on the Surface Structure and Morphology of Rutile TiO₂(110) Single Crystals," *J. Phys. Chem. B* **104**, 4944–4950 (2000).
- [164] J. Chen, L.-B. Lin, and F.-Q. Jing, "Theoretical study of F-type color center in rutile TiO₂," *J. Phys. Chem. Solids* **62**, 1257–1262 (2001).
- [165] M. Ramamoorthy, D. Vanderbilt, and R. D. King-Smith, "First-principles calculations of the energetics of stoichiometric TiO₂ surfaces," *Phys. Rev. B* **49**, 16721–16727 (1994).
- [166] D. Vogtenhuber, R. Podloucky, A. Neckel, S. G. Steinemann, and A. J. Freeman, "Electronic structure and relaxed geometry of the TiO₂ rutile (110) surface," *Phys. Rev. B* **49**, 2099–2103 (1994).
- [167] P. Reinhardt and B. A. Hess, "Electronic and geometrical structure of rutile surfaces," *Phys. Rev. B* **50**, 12015–12024 (1994).

- [168] S. P. Bates, G. Kresse, and M. J. Gillan, "A systematic study of the surface energetics and structure of $\text{TiO}_2(110)$ by first-principles calculations," *Surf. Sci.* **385**, 386–394 (1997).
- [169] P. J. D. Lindan, N. M. Harrison, M. J. Gillan, and J. A. White, "First-principles spin-polarized calculations on the reduced and reconstructed $\text{TiO}_2(110)$ surface," *Phys. Rev. B* **55**, 15919–15927 (1997).
- [170] B. Hird and R. A. Armstrong, "Ion scattering measurements of rutile $\text{TiO}_2(110)-(1 \times 1)$ surface relaxation," *Surf. Sci.* **385**, L1023–L1028 (1997).
- [171] B. Hird and R. A. Armstrong, "Surface relaxation of rutile $\text{TiO}_2(110)-(1 \times 1)$ from ion shadowing/blocking measurements," *Surf. Sci.* **420**, L131–L137 (1999).
- [172] G. Charlton *et al.*, "Relaxation of $\text{TiO}_2(110)-(1 \times 1)$ Using Surface X-Ray Diffraction," *Phys. Rev. Lett.* **78**, 495–498 (1997).
- [173] N. M. Harrison, X.-G. Wang, J. Muscat, and M. Scheffler, "The influence of soft vibrational modes on our understanding of oxide surface structure," *Faraday Discuss.* **114**, 305–312 (1999).
- [174] V. E. Henrich, G. Dresselhaus, and H. J. Zeiger, "Observation of Two-Dimensional Phases Associated with Defect States on the Surface of TiO_2 ," *Phys. Rev. Lett.* **36**, 1335–1339 (1976).
- [175] U. Diebold, J. F. Anderson, K.-O. Ng, and D. Vanderbilt, "Evidence for the Tunneling Site on Transition-Metal Oxides: $\text{TiO}_2(110)$," *Phys. Rev. Lett.* **77**, 1322–1325 (1996).
- [176] U. Diebold, J. Lehman, T. Mahmoud, M. Kuhn, G. Leonardelli, W. Hebenstreit, M. Schmid, and P. Varga, "Intrinsic defects on a $\text{TiO}_2(110)(1 \times 1)$ surface and their reaction with oxygen: a scanning tunneling microscopy study," *Surf. Sci.* **411**, 137–153 (1998).
- [177] S. Suzuki, K. Fukui, H. Onishi, and Y. Iwasawa, "Hydrogen Adatoms on $\text{TiO}_2(110)-(1 \times 1)$ Characterized by Scanning Tunneling Microscopy and Electron Stimulated Desorption," *Phys. Rev. Lett.* **84**, 2156–2159 (2000).
- [178] A. Szabo and T. Engel, "Structural studies of $\text{TiO}_2(110)$ using scanning tunneling microscopy," *Surf. Sci.* **329**, 241–254 (1995).
- [179] A. Berkó and F. Solymosi, "Study of Clean $\text{TiO}_2(110)$ Surface by Scanning Tunneling Microscopy and Spectroscopy," *Langmuir* **12**, 1257–1261 (1996).
- [180] C. L. Pang, S. A. Haycock, H. Raza, P. W. Murray, and G. Thornton, "Added row model of $\text{TiO}_2(110) 1 \times 2$," *Phys. Rev. B* **58**, 1586–1589 (1998).
- [181] R. E. Tanner, M. R. Castell, and G. A. D. Briggs, "High resolution scanning tunnelling microscopy of the rutile $\text{TiO}_2(110)$ surface," *Surf. Sci.* **412-413**, 672–680 (1998).
- [182] C. L. Pang, S. A. Haycock, H. Raza, G. Thornton, O. Gülseren, R. James, and D. W. Bullett, "Comment on 'High resolution scanning tunnelling microscopy of the rutile $\text{TiO}_2(110)$ surface' by R. E. Tanner, M. R. Castell, G. A. D. Briggs [Surf. Sci. 412/413 (1998) 672]," *Surf. Sci.* **437**, 261–262 (1999).
- [183] R. E. Tanner, M. R. Castell, and G. A. D. Briggs, "Reply to 'Comment on 'High resolution scanning tunnelling microscopy of the rutile $\text{TiO}_2(110)$ surface' by R.E. Tanner, M.R. Castell, G.A.D. Briggs" [Surf. Sci. 412/413 (1998) 672]," *Surf. Sci.* **437**, 263–264 (1999).
- [184] R. A. Bennett, S. Poulston, P. Stone, and M. Bowker, "STM and LEED observations of the surface structure of $\text{TiO}_2(110)$ following crystallographic shear plane formation," *Phys. Rev. B* **59**, 10341–10346 (1999).
- [185] H. Onishi and Y. Iwasawa, "Dynamic Visualization of a Metal-Oxide-Surface/Gas-Phase Reaction: Time-Resolved Observation by Scanning Tunneling Microscopy at 800 K," *Phys. Rev. Lett.* **76**, 791–794 (1996).
- [186] M. Li, W. Hebenstreit, and U. Diebold, "Oxygen-induced restructuring of the rutile $\text{TiO}_2(110)(1 \times 1)$ surface," *Surf. Sci.* **414**, L951–L956 (1998).
- [187] M. Li, W. Hebenstreit, L. Gross, U. Diebold, M. A. Henderson, D. R. Jennison, P. A. Schultz, and M. P. Sears, "Oxygen-induced restructuring of the $\text{TiO}_2(110)$ surface: a comprehensive study," *Surf. Sci.* **437**, 173–190 (1999).
- [188] M. Li, W. Hebenstreit, U. Diebold, M. A. Henderson, and D. R. Jennison, "Oxygen-induced restructuring of rutile formation $\text{TiO}_2(110)$: mechanism, atomic models, and influence on surface chemistry," *Faraday Discuss.* **114**, 245–258 (1999).

- [189] R. A. Bennett, P. Stone, and M. Bowker, "Scanning tunnelling microscopy studies of the reactivity of the $\text{TiO}_2(110)$ surface: Re-oxidation and the thermal treatment of metal nanoparticles," *Faraday Discuss.* **114**, 267–277 (1999).
- [190] R. A. Bennett, P. Stone, N. J. Price, and M. Bowker, "Two (1×2) Reconstructions of $\text{TiO}_2(110)$: Surface Rearrangement and Reactivity Studied Using Elevated Temperature Scanning Tunneling Microscopy," *Phys. Rev. Lett.* **82**, 3831–3834 (1999).
- [191] P. Stone, R. A. Bennett, and M. Bowker, "Reactive re-oxidation of reduced $\text{TiO}_2(110)$ surfaces demonstrated by high temperature STM movies," *Mat. Sci. Eng. A* **1**, 8 (1999).
- [192] O. Gülseren, R. James, and D. W. Bullett, "Theoretical analysis of STM experiments at rutile TiO_2 surfaces," *Surf. Sci.* **377-379**, 150–154 (1997).
- [193] K.-O. Ng and D. Vanderbilt, "Structure and apparent topography of $\text{TiO}_2(110)$ surfaces," *Phys. Rev. B* **56**, 10544–10548 (1997).
- [194] A. T. Paxton and L. Thiên-Nga, "Electronic structure of reduced titanium dioxide," *Phys. Rev. B* **57**, 1579–1584 (1998).
- [195] F. H. Jones, "Teeth and bones: applications of surface science to dental materials and related biomaterials," *Surf. Sci. Rep.* **42**, 75–205 (2001).
- [196] R. L. Kurtz, R. Stockbauer, T. E. Madey, E. Román, and J. L. de Segovia, "Synchrotron radiation studies of H_2O adsorption on $\text{TiO}_2(110)$," *Surf. Sci.* **218**, 178–200 (1989).
- [197] T. Bredow and K. Jug, "Theoretical investigation of water adsorption at rutile and anatase surfaces," *Surf. Sci.* **327**, 398–408 (1995).
- [198] J. Goniakowski and M. J. Gillan, "The adsorption of H_2O on TiO_2 and $\text{SnO}_2(110)$ studied by first-principles calculations," *Surf. Sci.* **350**, 145–158 (1996).
- [199] P. J. D. Lindan, N. M. Harrison, J. M. Holender, and M. J. Gillan, "First-principles molecular dynamics simulation of water dissociation on $\text{TiO}_2(110)$," *Chem. Phys. Lett.* **261**, 246–252 (1996).
- [200] J. Ahdjoudj, A. Markovits, and C. Minot, "Hartree-Fock periodic study of the chemisorption of small molecules on TiO_2 and MgO surfaces," *Catal. Today* **50**, 541–551 (1999).
- [201] P. J. D. Lindan, N. M. Harrison, and M. J. Gillan, "Mixed Dissociative and Molecular Adsorption of Water on the Rutile (110) Surface," *Phys. Rev. Lett.* **80**, 762–765 (1998).
- [202] K. F. Ferris and L.-Q. Wang, "Electronic structure calculations of small molecule adsorbates on (110) and (100) TiO_2 ," *J. Vac. Sci. Technol. A* **16**, 956–960 (1998).
- [203] E. V. Stefanovich and T. N. Truong, "Ab initio study of water adsorption on $\text{TiO}_2(110)$: molecular adsorption versus dissociative chemisorption," *Chem. Phys. Lett.* **299**, 623–629 (1999).
- [204] D. Vanderbilt, "Soft self-consistent pseudopotentials in a generalized eigenvalue formalism," *Phys. Rev. B* **41**, 7892–7895 (1990).
- [205] M. A. Henderson, "Structural Sensitivity in the Dissociation of Water on TiO_2 Single-Crystal Surfaces," *Langmuir* **12**, 5093–5098 (1996).
- [206] W. Langel, "Car-Parrinello simulation of H_2O dissociation on rutile," *Surf. Sci.* **496**, 141–150 (2002).
- [207] M. A. Henderson, W. S. Epling, C. L. Perkins, and C. H. F. Peden, "Interaction of Molecular Oxygen with the Vacuum-Annealed $\text{TiO}_2(110)$ Surface: Molecular and Dissociative Channels," *J. Phys. Chem.* **103**, 5328–5337 (1999).
- [208] W. S. Epling, C. H. F. Peden, M. A. Henderson, and U. Diebold, "Evidence for oxygen adatoms on $\text{TiO}_2(110)$ resulting from O_2 dissociation at vacancy sites," *Surf. Sci.* **412-413**, 333–343 (1998).
- [209] C. L. Perkins and M. A. Henderson, "Photodesorption and Trapping of Molecular Oxygen at the $\text{TiO}_2(110)$ -Water Ice Interface," *J. Phys. Chem. B* **105**, 3856–3863 (2001).
- [210] M. Valden, S. Pak, X. Lai, and D. W. Goodman, "Structure sensitivity of CO oxidation over model Au/TiO_2 catalysts," *J. Catal.* **56**, 7–10 (1998).
- [211] J. Jacobsen, B. Hammer, K. W. Jacobsen, and J. K. Nørskov, "Electronic structure, total energies, and STM images of clean and oxygen-covered $\text{Al}(111)$," *Phys. Rev. B* **52**, 14954–14962 (1995).

- [212] N. Lopez and J. K. Nørskov, "Theoretical study of the Au/TiO₂(110) interface," Surf. Sci. in press (2002).
- [213] H. Häkkinen and U. Landman, "Gold clusters (Au_N, 2 ≤ N ≤ 10) and their anions," Phys. Rev. B **62**, R2287–R2290 (2000).
- [214] J. Carrey, J.-L. Maurice, F. Petroff, and A. Vaurès, "Growth of Au Clusters on Amorphous Al₂O₃: Evidence of Cluster Mobility above a Critical Size," Phys. Rev. Lett. **86**, 4600–4603 (2001).
- [215] F. Cosandey and T. E. Madey, "Growth, morphology, interfacial effects and catalytic properties of Au on TiO₂," Surf. Rev. Lett. **8**, 73–93 (2001).
- [216] S. C. Parker, A. W. Grant, V. A. Bondzie, and C. T. Campbell, "Island growth kinetics during the vapor deposition of gold onto TiO₂(110)," Surf. Sci. **441**, 10–20 (1999).
- [217] J. V. Barth, "Transport of adsorbates at metal surfaces: from thermal migration to hot precursors," Surf. Sci. Rep. **40**, 75–149 (2000).
- [218] J. Wintterlin, R. Schuster, and G. Ertl, "Existence of a "Hot" Atom Mechanism for the Dissociation of O₂ on Pt(111)," Phys. Rev. Lett. **77**, 123–126 (1996).
- [219] H. Brune, J. Wintterlin, R. J. Behm, and G. Ertl, "Surface Migration of "Hot" Adatoms in the Course of Dissociative Chemisorption of Oxygen on Al(111)," Phys. Rev. Lett. **68**, 624–626 (1992).
- [220] U. Diebold, W. Hebenstreit, G. Leonardelli, M. Schmid, and P. Varga, "High Transient Mobility of Chlorine on TiO₂(110): Evidence for "Cannon-Ball" Trajectories of Hot Adsorbates," Phys. Rev. Lett. **81**, 405–408 (1998).
- [221] S. Schintke, S. Messerli, K. Morgenstern, J. Nieminen, and W.-D. Schneider, "Far-ranged transient motion of "hot" oxygen atoms upon dissociation," J. Chem. Phys. **114**, 4206–4209 (2001).
- [222] J. Harris and B. Kasemo, "On precursor mechanisms for surface reactions," Surf. Sci. **105**, L281–L287 (1981).
- [223] D. Vogtenhuber, R. Podloucky, J. Redinger, E. L. D. Hebenstreit, W. Hebenstreit, and U. Diebold, "Ab initio and experimental studies of chlorine adsorption on the rutile TiO₂(110) surface," Phys. Rev. B **65**, 125411 (2002).
- [224] A. Kolmakov and D. W. Goodman, "Imaging gold clusters on TiO₂(110) at elevated pressures and temperatures," Catal. Lett. **70**, 93–97 (2000).
- [225] S. Völkening, K. Bedürftig, K. Jacobi, J. Wintterlin, and G. Ertl, "Dual-Path Mechanism for Catalytic Oxidation of Hydrogen on Platinum Surfaces," Phys. Rev. Lett. **83**, 2672–2675 (1999).
- [226] C. Sachs, M. Hildebrand, S. Völkening, J. Wintterlin, and G. Ertl, "Spatiotemporal Self-Organization in a Surface Reaction: From the Atomic to the Mesoscopic Scale," Science **293**, 1635–1638 (2001).
- [227] C. Stampfl, H. J. Kreuzer, S. H. Payne, H. Pfnür, and M. Scheffler, "First-Principles Theory of Surface Thermodynamics and Kinetics," Phys. Rev. Lett. **83**, 2993–2996 (1999).
- [228] X.-G. Wang, A. Chaka, and M. Scheffler, "Effect of the Environment on α-Al₂O₃(0001) Surface Structures," Phys. Rev. Lett. **84**, 3650–3653 (2000).

Acknowledgements

During the course of my PhD studies in the CAMP group, I have cooperated and interacted with a large number of people. Of these, I would specifically like to thank my principal collaborators Toshu An, Kim Højrup Hansen, Stig Helveg, Réналd Schaub, Krishna Swamy, Ebbe Kruse Vestergaard, Erik Wahlström, and Lars Österlund. Invaluable advice from the three group seniors, Erik Lægsgaard, Ivan Stensgaard, and Flemming Besenbacher, is greatly appreciated. From Flemming in particular I have met an incessant optimism and trust, which I hope to have reciprocated.

I have enjoyed a fruitful collaboration with our CAMP sister group at the Technical University of Denmark. I would like to thank Ebbe Christoffersen, Nuria Lopez Alonso and Jens K. Nørskov for having shown interest in my work and performing the Monte Carlo simulations in Chap. 5 and the theoretical part of the $\text{TiO}_2(110)$ studies. I also acknowledge Bjørk Hammer and Maria Dall Rasmussen from University of Aarhus for recent theoretical input.

A number of people have made suggestions for improvements during the making of this thesis. Maria Dall Rasmussen, Réналd Schaub, Erik Wahlström commented on parts of the thesis, but especially Ebbe Kruse Vestergaard and Michael Schunack will be gratefully remembered for a very thorough read indeed.

Last, by not least, my scientific endeavors would have been impossible were it not for the caring support from Rebeca, my lovely wife.

The Aarhus STM group is part of the Center for Atomic-scale Materials Physics (CAMP), funded by the Danish National Research Foundation. Personal support is acknowledged from the Danish Research Counsel materials program “New Design Strategies for Catalysts”.